Colloquium: Quantum anomalous Hall effect

Cui-Zu Chang[*] and Chao-Xing Liu[†]

Department of Physics, The Pennsylvania State University, University Park, Pennsylvania 16802, USA

Allan H. MacDonald[‡]

Department of Physics, The University of Texas at Austin, Austin, Texas 78712, USA

(published 23 January 2023)

The quantum Hall (QH) effect, quantized Hall resistance combined with zero longitudinal resistance, is the characteristic experimental fingerprint of Chern insulators—topologically nontrivial states of two-dimensional matter with broken time-reversal symmetry. In Chern insulators, nontrivial bulk band topology is expressed by chiral states that carry current along sample edges without dissipation. The quantum anomalous Hall (QAH) effect refers to QH effects that occur in the absence of external magnetic fields due to spontaneously broken time-reversal symmetry. The QAH effect has now been realized in four different classes of two-dimensional materials: (i) thin films of magnetically (Cr- and/or V-) doped topological insulators in the $(Bi, Sb)_2Te_3$ family, (ii) thin films of the intrinsic magnetic topological insulator $MnBi_2Te_4$, (iii) moiré materials formed from graphene, and (iv) moiré materials formed from transition-metal dichalcogenides. In this Colloquium, the physical mechanisms responsible for each class of QAH insulator are reviewed, with both differences and commonalities highlighted, and potential applications of the QAH effect are commented upon.

DOI: 10.1103/RevModPhys.95.011002

CONTENTS

[*]cxc955@psu.edu
[†]cxl56@psu.edu
[‡]macd@physics.utexas.edu

I. INTRODUCTION

The quantum Hall (QH) effect refers to quantization of the Hall conductance of a material at integer multiples of e^2/h, a value that is dependent on only two fundamental physical constants, the electron charge e and the Planck constant h. Precision QH effect measurements currently achieve deviations from exact quantization of 1 part in 10^{10} (Schopfer and Poirier, 2007), an accuracy that allows the QH effect to play an essential role in metrology (Jeckelmann and Jeanneret, 2001; Poirier and Schopfer, 2009). The QH effect was first observed (Klitzing, Dorda, and Pepper, 1980) in semiconductor quantum well two-dimensional (2D) electron gas systems in strong perpendicular magnetic fields that cause electrons to execute closed cyclotron orbits with quantized

kinetic energy. The quantum mechanical problem of independent electrons in a magnetic field was first addressed by Lev Landau (Landau, 1930; Landau and Lifshitz, 2013), and the set of orbitals with a discrete allowed kinetic energy is known as a Landau level.

Although early explanations of the QH effect were based on the specific properties of Landau levels, one could ask whether the phenomenon of precise quantization of Hall resistance could also occur, at least in principle, in the absence of a magnetic field. An affirmative answer to this question was supplied early in the development of the theory of the QH effect. In 1982, Thouless, Kohmoto, Nightingale, and den Nijs (TKNN) (Thouless *et al.*, 1982) derived a formula that related the Hall conductivity of a 2D crystalline insulator to the integral of the Bloch state momentum-space Berry curvature (Xiao, Chang, and Niu, 2010) over the finite area toroidal momentum space (the Brillouin zone) of a 2D crystal. For each band, the integral is always an integer multiple of 2π, and the integer is the Chern number: a topological index that classifies how the Bloch wave function depends on crystal momentum. It is noteworthy that this seemingly abstract mathematical quantity is observable experimentally simply by performing a standard transport measurement.

Since momentum space is finite only for electrons in a periodic potential, the TKNN formula does not apply directly to the Landau levels of electron gas systems. In the TKNN paper, the formula was applied to a single-band square-lattice tight-binding model with an external magnetic field. Commensurability (MacDonald, 1983) between the crystal unit cell area and the area that encloses one quantum of magnetic flux then leads to fractal energy spectra often referred to as Hofstadter butterflies (Hofstadter, 1976). Initially, the possibility that Chern numbers could in principle be nonzero even in the absence of a magnetic field was not emphasized. This property was first explicitly highlighted in an important 1988 paper by Duncan Haldane (Haldane, 1988), in which he constructed a toy model of electrons on a honeycomb lattice with zero spatially averaged perpendicular field whose bands nevertheless have nonzero Chern numbers. The bands of the model, like those of any magnetic crystal, do, however, break time-reversal (TR) symmetry.

A band insulator that exhibits nonzero integer Hall conductance but preserves lattice translation symmetry is called a Chern insulator, or sometimes a Hofstadter-Chern insulator if a magnetic field is present. The terms Chern insulator and quantum anomalous Hall (QAH) insulator are almost identical in usage, although the term QAH insulator is sometimes used to refer to the zero-magnetic-field subset of Chern insulators. In this Colloquium, we adopt this terminology. The adjective anomalous for a QH effect without a magnetic field is adopted from the terminology used to describe the Hall effects of three-dimensional (3D) magnetic conductors in the absence of a magnetic field, which are generically nonzero, as discovered by Edwin Hall (Hall, 1880) in the 19th century.

The underlying microscopic mechanism of Hall's bulk anomalous Hall (AH) effect was controversial for more than a century. The modern Berry phase theory of the AH effect (Nagaosa *et al.*, 2010; Xiao, Chang, and Niu, 2010) in magnetic conductors, and interest in the role of momentum-space Berry phases in transport more generally, can be traced in part to the TKNN paper. It is now clear that the intrinsic Berry phase contribution to the AH conductivity, in the case of 2D insulators proportional to the Chern number summed over occupied bands and the only contribution to the Hall conductivity, is often also important in metals. In the metal case, the integral of the Berry curvature, which is taken over occupied electronic states only, is not the only contribution to the Hall effect and is not quantized.

The TKNN formula tells us that the Hall conductance in 2D magnetic insulators and semiconductors is always quantized. The quantized value is, however, almost always zero in the absence of a magnetic field. For several decades, little progress was made toward experimental realization of the QAH effect (Onoda and Nagaosa, 2003; Nagaosa *et al.*, 2010). Prospects improved around 2006 with the discovery of topological insulators (TIs) (Kane and Mele, 2005; Bernevig, Hughes, and Zhang, 2006; Bernevig and Zhang, 2006; Fu and Kane, 2007; Fu, Kane, and Mele, 2007; König *et al.*, 2007; Moore and Balents, 2007; Chen *et al.*, 2009; Roy, 2009; Xia *et al.*, 2009; Zhang *et al.*, 2009; Lapano *et al.*, 2020; Ledwith *et al.*, 2020), which were to provide a natural platform. A TI possesses a topologically nontrivial electronic band structure protected by TR symmetry (Hasan and Kane, 2010; Qi and Zhang, 2011) and has topologically protected boundary modes. Because 2D TIs have a quantized spin Hall effect, opposite sign Hall effects in opposite spin sectors, it was natural to consider (Qi, Wu, and Zhang, 2006) what could be achieved by adding magnetism to TIs. The first theoretical proposal was to dope Mn ions into HgTe/CdTe quantum wells, a 2D TI system (Liu, Qi *et al.*, 2008). However, it turns out that HgTe remains paramagnetic when Mn doped and does not break TR symmetry. A weak magnetic field (~0.07 T) is therefore necessary to drive the system into a quantized state (Budewitz *et al.*, 2017). Soon thereafter, a related strategy was proposed (Qi, Hughes, and Zhang, 2008; Yu *et al.*, 2010), namely, introducing magnetic dopants (such as Cr or Fe) into the 3D TI $(\mathrm{Bi/Sb})_2(\mathrm{Se/Te})_3$ [Fig. 3(a)]. This approach led to successful realization of the QAH effect in Cr-doped $(\mathrm{Bi,Sb})_2\mathrm{Te}_3$ films in 2013 (Chang *et al.*, 2013a), and in V-doped $(\mathrm{Bi,Sb})_2\mathrm{Te}_3$ films in 2015 (Chang, Zhao, Kim, Zhang *et al.*, 2015). Since then, the QAH effect and the physical properties of Cr- or V-doped $(\mathrm{Bi,Sb})_2\mathrm{Te}_3$ have been extensively studied by experimental groups worldwide.

Despite impressive progress (Chang *et al.*, 2013a; Chang, Zhao, Kim, Zhang *et al.*, 2015; Mogi *et al.*, 2015; Ou *et al.*, 2018), the magnetic doping approach has a clear disadvantage in that it inevitably degrades the sample quality, and thus limits the critical temperature of the QAH state. It is therefore desirable to realize the QAH effect in materials with intrinsic magnetism. This goal was recently achieved in manually exfoliated $\mathrm{MnBi}_2\mathrm{Te}_4$ flakes (Deng *et al.*, 2020). Separately, the QAH effect has now also been achieved (Sharpe *et al.*, 2019; Y. Chen *et al.*, 2020; Serlin *et al.*, 2020) in moiré superlattice systems (Andrei *et al.*, 2021) that do not contain magnetic elements, including twisted bilayer graphene (TBG) (Sharpe *et al.*, 2019; Serlin *et al.*, 2020), *ABC* trilayer graphene on hexagonal boron nitride (*h*-BN) (Y. Chen *et al.*, 2020), and transition-metal dichalcogenide (TMD)

heterobilayers (T. Li *et al.*, 2021b). In moiré superlattices, the AH effect is driven not by local-moment spin magnetism in combination with spin-orbit coupling (SOC), but instead by unusual purely orbital magnetic states.

Early developments in the theory of the QAH effect and the work responsible for the effect's first experimental realization in magnetically doped TIs have both been discussed (Weng *et al.*, 2015; Chang and Li, 2016; Liu, Zhang, and Qi, 2016; He, Wang, and Xue, 2018; Tokura, Yasuda, and Tsukazaki, 2019). The aim of this Colloquium is to provide a detailed description of the QAH effects that have been realized in magnetically doped TIs, the intrinsic magnetic TI $MnBi_2Te_4$, and moiré materials (Sec. II). We seek to identify important features that are unique to each class of systems (Secs. III–V, and also to identify commonalities. We also discuss potential applications of the QAH effect in quantum information devices, spintronics, and metrology and provide an outlook on future research directions (Sec. VI).

II. PHYSICAL MECHANISMS OF THE QAH EFFECT

A. Dirac models and Berry curvature

1. The two-dimensional Dirac equation

A common feature of all currently established QAH systems, magnetically doped TI films, films of the intrinsic magnetic TI $MnBi_2Te_4$, magic-angle TBG, *ABC* trilayer graphene on *h*-BN, and TMD moirés is adiabatic connection to a limit in which the band states close to the Fermi level can be described by 2D massive Dirac equations. We therefore use this model as a springboard for our discussion. The 2D massive Dirac Hamiltonian is

$$H_{\mathrm{D}} = \hbar v_{\mathrm{D},x} k_x \sigma_x + \hbar v_{\mathrm{D},y} k_y \sigma_y + m\sigma_z, \tag{1}$$

where $\sigma_{x,y,z}$ are Pauli matrices, $\mathbf{k}$ is the electron momentum, $v_{\mathrm{D},x(y)}$ is the Dirac velocity along the x (y) direction, and m is a mass parameter that characterizes the energy gap. The 2D Dirac model is not periodic in momentum and is therefore not a crystal Hamiltonian. When applied to crystalline electronic degrees of freedom, it is intended to apply only in small isolated portions of the Brillouin zone (BZ) with large Berry curvatures, and the zero of momentum is chosen to be at the center of that region. The two-level degrees of freedom that the Pauli matrices in H_{D} act on are defined by the two bands that cross at $\mathbf{k} = 0$ when $m = 0$.

The electronic momentum-space Berry curvature in a crystal is defined in terms of the dependence of the Bloch wave functions on momentum:

$$\Omega_{xy,s}(\mathbf{k}) = i(\langle \partial_{k_x} u_s | \partial_{k_y} u_s \rangle - \langle \partial_{k_y} u_s | \partial_{k_x} u_s \rangle), \tag{2}$$

where s is a band index and $u_{s,\mathbf{k}}$ is a Bloch state eigen–wave function. The TKNN formula states that the Hall conductivity σ_{xy} in a band insulator is related to the Chern number C by

$$\sigma_{xy} = \frac{e^2}{h} C, \tag{3}$$

where the Chern number

$$C = \frac{1}{2\pi} \int_{\mathrm{BZ}} d^2k \sum_{s\in \mathrm{occ}} \Omega_{xy,s}(\mathbf{k}) \tag{4}$$

is an integer. In Eq. (4), the sum is over occupied bands and BZ specifies that the integral is over the entire BZ.

Chern numbers are particularly easy to evaluate in two-band models since the Berry curvature is then proportional (Auerbach, 2012) to the area enclosed on the two-level Bloch sphere per area enclosed in momentum space. It follows that the Berry curvature of the 2D Dirac Hamiltonian [Eq. (1)] is

$$\Omega_{xy,s} = -\frac{sm\hbar^2 v_{\mathrm{D},x} v_{\mathrm{D},y}}{2[(\hbar v_{\mathrm{D},x} k_x)^2 + (\hbar v_{\mathrm{D},y} k_y)^2 + m^2]^{3/2}}, \tag{5}$$

where $s = \pm$ is a band label that specifies the sign of 2D Dirac band energy and $E_s = s\sqrt{(\hbar v_{\mathrm{D},x} k)^2 + (\hbar v_{\mathrm{D},y} k_y)^2 + m^2}$. From Eq. (5), one can see that the Berry curvature in the 2D Dirac equation is concentrated within a momentum-space area proportional to $(m/\hbar v_{\mathrm{D}})^2$ (where $v_{\mathrm{D}} \sim v_{\mathrm{D},x} \sim v_{\mathrm{D},y}$), and that it decays as $|\mathbf{k}|^{-3}$ for large $|\mathbf{k}|$. The Hall conductivity σ_{xy} cannot be directly determined from the 2D Dirac model, since the former requires an integral over the entire BZ [Eqs. (3) and (4)], including momenta outside the Dirac model's range of validity. This effective model approach is nevertheless useful in understanding the topological properties of realistic materials that have a small value of m. In that case we can choose a momentum-space cutoff Λ that is simultaneously large compared to $m/\hbar v_{\mathrm{D}}$, and therefore large enough to capture nearly all the Berry curvature integral, and small compared to the size of BZ (and therefore within the range of validity of the 2D Dirac model). In this limit, the Hall conductivity in Eq. (3) $\sigma_{xy} \to \mathrm{sgn}(v_{\mathrm{D},x} v_{\mathrm{D},y} m) e^2/2h$. Each 2D Dirac Hamiltonian therefore contributes $\pm e^2/2h$ to the Hall conductivity; the band states cover half the Bloch sphere starting from a pole position at $\mathbf{k} = 0$, circling the sphere when $\mathbf{k}$ executes a circle and moving toward the equator as $|\mathbf{k}| \to \infty$. The sign of the Hall contribution is determined by the relative signs of $v_{\mathrm{D},x}$, $v_{\mathrm{D},y}$, and m.

The TKNN paper tells us that the total Hall conductivity in any 2D crystal must be an integer multiple of e^2/h. When level crossings in a 2D crystal are weakly gapped by TR symmetry breaking so that almost all the Berry curvature contributions are associated with 2D Dirac fermions, the integer can be determined simply by summing half-quantized contributions of variable signs. It follows that the number of local Dirac Hamiltonians [Eq. (1)] across the BZ must be even. This property can be viewed as a 2D version (Semenoff, 1984; Fradkin, Dagotto, and Boyanovsky, 1986; Haldane, 1988; Fang and Fu, 2019) of the fermion-doubling theorem (Nielsen and Ninomiya, 1981a, 1981b) for Weyl points in 3D crystals with TR symmetry.

The relationships of 2D Dirac fermions to realistic QAH systems are summarized in Fig. 1; see Secs. II.A.2 and II.A.3. Here we consider a toy model, the Haldane model, which was the first theoretical model for the QAH effect. The Haldane model was constructed by adjusting the electronic structure of graphene (Haldane, 1988) in a way that was mainly of academic interest at the time. The low-energy electronic

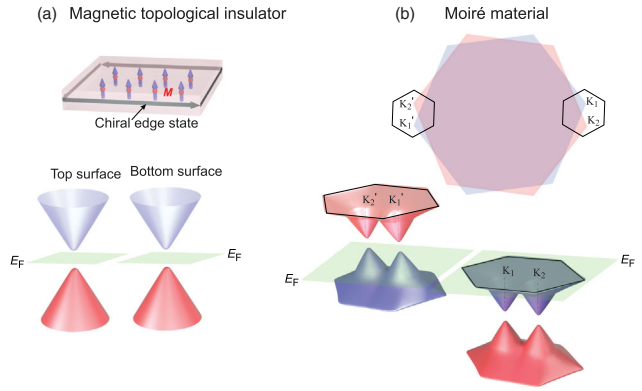

FIG. 1. QAH effects in magnetic TI and moiré superlattice systems. In both cases gapped Dirac cones contribute $\sigma_{xy} = \pm e^2/2h$ to the Hall conductance. The sign of the contribution is distinguished by the color (red or blue) of the lower energy occupied band. The Fermi level [green (light gray) plane] must be in a gap for the Hall effect to be quantized. (a) Schematic of a magnetic TI thin film. The TR symmetry of a TI is broken by the appearance of ferromagnetism in the sample. The total Hall conductance of a magnetic TI film is $\sigma_{xy} = (1/2 + 1/2)\, e^2/h = e^2/h$ when the two surfaces have parallel magnetization directions. (b) The BZ and moiré BZ of a triangular lattice moiré material. The moiré minibands located near the K and K' valleys are related by TR. A QAH effect occurs when the two 2D Dirac cones in the same valley contribute half-quantized Hall conductances of the same sign and the moiré miniband filling factors in the two valleys differ. The green (light gray) planes in (a) and (b) are constant energy surfaces in gaps between occupied and empty bands.

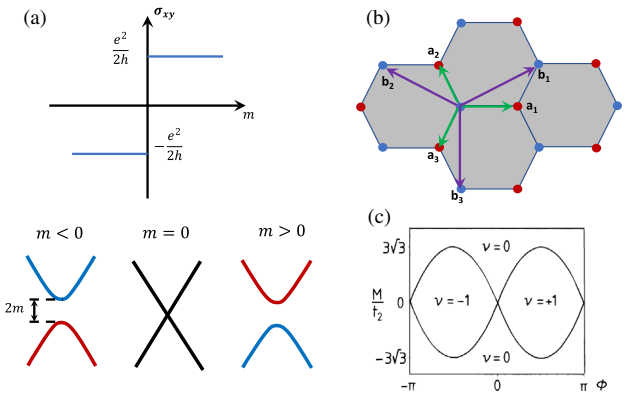

FIG. 2. Haldane model for the QAH effect. (a) The Hall conductivity σ_{xy} as a function of the mass m in 2D Dirac equation. When m changes from a negative value to a positive value, σ_{xy} jumps from $-e^2/2h$ to $e^2/2h$. (b) Honeycomb lattice of the Haldane model. Here $\mathbf{a}_i$ and $\mathbf{b}_i$, respectively, label the NN and NNN translation vectors. (c) Phase diagram of the Haldane model. ν is the Chern number. From Haldane, 1988.

structure of graphene (Castro Neto *et al.*, 2009) can be described using a single π-band tight-binding model on a honeycomb lattice with nearest neighbor (NN) hopping between the A and B sublattices. This model yields gapless Dirac cones centered on the K and K' BZ corners. To demonstrate that the QAH effect was a realistic experimental possibility, Haldane added artificial complex next-nearest neighbor (NNN) intrasublattice (A to A and B to B) hopping terms [illustrated in Fig. 2(b)] to the graphene tight-binding model. The complex hopping terms break TR symmetry and can be viewed as being induced by a magnetic field that has the periodicity of the lattice and a vanishing spatial average. When both NN and NNN hopping are included, the modified tight-binding model Hamiltonian,

$$\begin{aligned} H(\mathbf{k}) = {} & t_1 \sum_{i\in \mathrm{NN}} [\cos(\mathbf{k}\cdot\mathbf{a}_i)\sigma_x + \sin(\mathbf{k}\cdot\mathbf{a}_i)\sigma_y] \\ & + 2t_2 \cos\phi \sum_{i\in \mathrm{NNN}} \cos(\mathbf{k}\cdot\mathbf{b}_i) \\ & + \left(M - 2t_2 \sin\phi \sum_{i\in \mathrm{NNN}} \sin(\mathbf{k}\cdot\mathbf{b}_i)\right)\sigma_z, \end{aligned} \tag{6}$$

preserves the original translational symmetry. In Eq. (6), $\sigma_{x,y,z}$ are three Pauli matrices for the A and B sublattices, t_1 is the NN hopping parameter, t_2 and ϕ are the amplitude and phase of the NNN hopping parameter, M accounts for a possible on-site energy difference between the A and B sublattices, and $\mathbf{a}_i$ and $\mathbf{b}_i$ are the lattice vectors between the NN and NNN sites, respectively. In the limit $t_2, M \ll t_1$, the low-energy physics will be completely determined by the 2D Dirac fermions located at K and K'. We can then expand the tight-binding Hamiltonian around K and K' as

$$H_{\mathbf{K}(\mathbf{K}')} = \mp \frac{3t_1}{2}(\kappa_x\sigma_x \pm \kappa_y\sigma_y) + (M \pm 2t_2\cos\phi)\sigma_z, \tag{7}$$

where a constant term has been absorbed into the zero of energy. Comparing Eq. (7) to Eq. (1), this Hamiltonian can be recognized as a massive Dirac model with velocities $\hbar v_{\mathrm{D},x} = \pm(3/2)t_1$ and $\hbar v_{\mathrm{D},y} = -(3/2)t_1$ and mass $m = M \pm 2t_2\cos\phi$. Therefore, in the limit $M, t_2 \ll t_1$ the Hall conductance σ_{xy} can be directly read from the relative signs of $v_{\mathrm{D},x(y)}$ and m. Since the sign of $v_{\mathrm{D},x}v_{\mathrm{D},y}$ is the opposite for the Dirac cones at $\mathbf{K}$ and $\mathbf{K}'$, the contribution to the Hall conductance σ_{xy} of the Dirac cones at $\mathbf{K}$ and $\mathbf{K}'$ will share the same sign when t_2 dominates, but will be the opposite if the M term is dominant. A phase transition [Fig. 2(a)] occurs at $M = \pm 2t_2\cos\phi$. (The $t_2 = 0$, $M \neq 0$ version of this model is realized by graphene on aligned h-BN, as previously discussed.) The model has a QAH state with $\pm e^2/h$ Hall conductivity when $|2t_2\cos\phi| > M$, as shown in Fig. 2(c).

The Haldane model can describe some TMD moiré homobilayers. When the two valence band tops in a TMD bilayer are close in energy, interlayer hybridization becomes important and the one-band Hubbard model (Wu *et al.*, 2018) of typical heterobilayers must be decorated with a two-level layer degree of freedom that acts much like the sublattice degree of freedom in the Haldane model. The orbitals in each layer can be approximated by triangular lattice Hubbard models, with the lattice points located at the position where the metal atoms of one layer are directly above or below chalcogen atoms of the other layer. In bilayers, the two triangular lattice models combine to form a honeycomb lattice, and the one-band tight-binding model generalizes to a 2×2 tight-binding model. Band crossings at the moiré BZ

corners are avoided because the site-diagonal terms in the Hamiltonian favor one layer over the other. When opposite layers are favored at opposite moiré BZ corners, as happens in the heterobilayer case (F. Wu *et al.*, 2019; Pan *et al.*, 2022), the bilayer is described by a moiré superlattice length scale version of the Haldane model and the valley-projected bands carry nonzero Chern numbers.

2. Magnetic TI films

The discussion in this section applies to thin films of both magnetically doped TIs and the intrinsic magnetic TI $MnBi_2Te_4$. TIs have been reviewed by Hasan and Kane (2010) and Qi and Zhang (2011). In the prototype $(Bi/Sb)_2(Se/Te)_3$ TI family, the form for one topological surface state (TSS) is particularly simple and described by the effective Hamiltonian

$$H_{\rm sur} = \hbar v_{\rm D}(k_x\sigma_y - k_y\sigma_x), \tag{8}$$

where the Pauli matrices σ_i act on electron spin, or more strictly speaking a pseudospin formed by the $\mathbf{k} = 0$ Kramers doublet. This effective Hamiltonian $H_{\rm sur}$ coincides with Eq. (1) with $m \to 0$ after performing the spin rotation $\sigma_y \to \sigma_x$ and $\sigma_x \to -\sigma_y$. Note that $H_{\rm sur}$ has the same form as the SOC terms in the Rashba Hamiltonian (Bychkov and Rashba, 1984) that describes 2D electron gases in semiconductor quantum wells and the surface states of certain heavy metals (Koroteev *et al.*, 2004; Krupin *et al.*, 2005). This similarity reflects the common SOC origin of the spin splitting. Unlike in ordinary Rashba bands, one branch of TSSs merges with the bulk conduction band at large momentum, while the other branch merges with the valence band. When the Fermi energy is located in the bulk gap of a TI, there is only a single spin-momentum locked helical Fermi surface for one TSS. Ordinary Rashba bands have k^2 terms in their Hamiltonians that dominate at large momenta so that there are always two Fermi surfaces with opposite helicities.

The gapless nature of the TSSs ($m = 0$ in the 2D Dirac equation) is protected by TR symmetry and Kramers's theorem, which in solids states that an eigenstate at the momentum $\mathbf{k}$ has the same energy as an orthogonal time-reversed eigenstate at the momentum $-\mathbf{k}$. The energy spectrum of $H_{\rm sur}$ satisfies the requirements of Kramers's theorem. At TR-invariant momenta, Kramers's theorem requires double degeneracies $[E_s(0) = E_{-s}(0)]$. Thus, the band touching point, called the Dirac point, between two branches of $H_{\rm sur}$ is at a TR-invariant momentum. Inducing magnetization in a TI produces exchange coupling between the ordered magnetic moments and the TSS spins, and introduces an additional nonzero mass term $H_{\rm ex} = m\sigma_z$ in $H_{\rm sur}$ when the magnetization has an out-of-plane component. According to the discussion in Sec. II.A.1, the Dirac fermions at each surface are described by 2D Dirac Hamiltonians $H_{\rm sur} + H_{\rm ex}$ that together give rise to a contribution of $\pm e^2/2h$ to the Hall conductivity. This property has been referred to as a "surface half QH effect" (Qi, Hughes, and Zhang, 2008; Chu, Shi, and Shen, 2011; Qi and Zhang, 2011). The TSSs exist for both the top and bottom surfaces for a TI film, and since both Dirac velocities have opposite signs on opposite surfaces, the two 2D Dirac cones contribute Hall conductivities of the same sign when their masses have the same sign, i.e., when the magnetizations are parallel near two surfaces. Consequently, one expects a total Hall conductivity $\pm e^2/h$ for a TI film with a uniform magnetization, as shown in Fig. 1(a), where the $\pm$ sign depends on the magnetization direction. Since the QAH effect requires only surface magnetization, the role of the bulk magnetic order is simply to lock two surface magnetizations into a parallel configuration.

3. Moiré materials

After the first realization of the QAH effect in Cr-doped $(Bi, Sb)_2Te_3$ (Chang *et al.*, 2013a), the search for new QAH materials focused on compounds with heavy elements that can host both strong SOC and local magnetic moments. Unexpectedly, the QAH effect was, however, next discovered (Sharpe *et al.*, 2019; Serlin *et al.*, 2020) in a system composed entirely of carbon atoms, light elements with weak SOC, and no magnetic moments, TBG. The TBG case represents a new route to realize the QAH effect in which emergent translational symmetries, orbital magnetic moments, and Coulomb interactions all play essential roles. Related QAH effects have now been oberved in *ABC* trilayer graphene on *h*-BN (Y. Chen *et al.*, 2019) and TMD bilayer moiré superlattices (T. Li *et al.*, 2021b).

Moiré patterns are formed in few-layer van der Waals thin films by overlaying layers that have different lattice constants or different orientations (Andrei and MacDonald, 2020; Andrei *et al.*, 2021). When the host 2D materials are semiconductors or semimetals and the period of the moiré pattern is long compared to the lattice constants of the host 2D crystals, the moiré pattern gives rise to low-energy effective Hamiltonians with an emergent translational symmetry that has the periodicity of the moiré pattern, i.e., to artificial crystals (moiré materials) with lattice constants on the ∼10 nm scale. TBG and group VI TMD bilayers are the prototypical moiré materials. In graphene and most TMDs, the host materials have triangular Bravais lattices and low-energy states have crystal momenta in valleys centered on one of two inequivalent BZ-corner momenta [K and K' in Fig. 1(b)] that are related to each other by TR symmetry. The valley flavor is a good quantum number in the emergent moiré band Hamiltonian, and the valley-projected Hamiltonians are not in general TR invariant. It follows that TBG and TMD moiré bands can have nonzero Chern numbers.

The low-energy valley-projected Hamiltonian of an isolated graphene layer is the massless Dirac model of Eq. (1). The mass m can be generated (Giovannetti *et al.*, 2007; Quhe *et al.*, 2012; Yankowitz *et al.*, 2012; San-Jose *et al.*, 2014) by interaction with an adjacent layer of *h*-BN, the material that is now nearly universally employed to isolate graphene multilayer systems chemically. A finite Dirac mass m can also be generated spontaneously by electron-electron interactions (Min *et al.*, 2008; Xue and MacDonald, 2018; Bultinck, Chatterjee, and Zaletel, 2020) when the Dirac velocities are sufficiently low. Because of its emergent moiré bands, gaps can appear in the spectrum not only at neutrality but also at electron densities that are multiples of $4/A_{\rm M}$, where $A_{\rm M}$ is the moiré pattern unit cell area and the factor of 4 accounts for

spin and valley degeneracy. In electrically neutral twisted bilayers, the separate half QH effects of the two layers combine constructively. TBG, therefore, normally has a quantum valley Hall effect (Xiao, Yao, and Niu, 2007; Martin, Blanter, and Morpurgo, 2008; J. Li *et al.*, 2016; Li *et al.*, 2018; J. Liu *et al.*, 2019; Andrei and MacDonald, 2020; Liu and Dai, 2021a), opposing QH effect contributions from opposite valleys at neutrality. The quantum valley Hall effect is promoted to a true charge QAH effect when the Fermi level lies in a Dirac gap for an odd number of spin-valley flavors, as depicted in Fig. 1(b). The origin of the QAH effect is therefore spontaneous valley polarization, a purely orbital type of TR symmetry breaking that also leads to magnetization with a dominantly orbital nature (Zhu, Su, and MacDonald, 2020; C. Liu *et al.*, 2021).

In TMD heterobilayers, electrons and holes are often strongly confined to one layer or the other. They can then be described (Wu *et al.*, 2018) by single-band Hubbard models with an approximately parabolic kinetic energy operator and an external potential with moiré periodicity. Since the Hubbard model is TR invariant, the valley-projected bands do not carry nonzero Chern numbers when this approximation is valid. The situation changes in homobilayers and heterobilayers, in which gate voltages have been adjusted to favor strong hybridization between layers (F. Wu *et al.*, 2019; T. Li *et al.*, 2021b; Pan *et al.*, 2022). Under these circumstances, the valley-projected bands have a layer degree of freedom that acts as a pseudospin and allows each valley to provide a physical realization of the Haldane model, which is the first theoretical model of the QAH effect and is discussed later. The QAH effect was recently discovered in a TMD heterobilayer system (T. Li *et al.*, 2021b) in which the layer degree of freedom is activated by applying large gate-controlled transverse displacement fields.

B. Physical mechanisms of magnetism

1. Magnetically doped TIs

Magnetically doped TIs can be viewed as a special type of diluted magnetic semiconductor (Van Vleck, 1953; Zener and Heikes, 1953; Jungwirth *et al.*, 2006; Sato *et al.*, 2010; Dietl and Ohno, 2014) with strong SOC. A qualitative understanding of the magnetic properties of these systems can be obtained by separating the entire system into two subsystems, topologically nontrivial band electrons and local magnetic moments from magnetic doping. The two subsystems are coupled to each other, through interactions that are also typically referred to as exchange interactions and have the form $H_{\rm ex} = J_{\rm ex}\sum_i \mathbf{S}_i \cdot \mathbf{s}(\mathbf{R}_i)$, where $\mathbf{s}(\mathbf{r})$ is the electron spin operator at position $\mathbf{r}$ and $\mathbf{S}_i$ is the spin of the ith magnetic impurity. Here $J_{\rm ex}$ is the exchange coupling parameter. The microscopic mechanism of this coupling is discussed later.

Provided that the magnetic moments are uniformly distributed on characteristic electronic length scales, $\sum_i \mathbf{S}_i \cdot \mathbf{s}(\mathbf{R}_i)$ can be replaced by $n_{\rm M}\int d\mathbf{R}\, \mathbf{S}(\mathbf{R}) \cdot s(\mathbf{R})$, where $n_{\rm M}$ is the local-moment density. When this interaction is treated in a mean-field approximation, which was employed in an early paper by Zener (1951), the band spins see a mean magnetic field (in energy units) $-J_{\rm ex} n_{\rm M} \langle \mathbf{S} \rangle$ and the local moments see a magnetic field $\mathbf{H} = -J_{\rm ex}\langle \mathbf{s} \rangle$, where $\langle \mathbf{S} \rangle$ and $\langle \mathbf{s} \rangle$ are the thermal averages of the local-moment spins and the band electron spin densities. Given the effective magnetic field $\langle \mathbf{S} \rangle$ can be calculated from the textbook formula for polarization of an isolated local moment in a thermal bath $\langle \mathbf{S} \rangle = S\hat{\mathbf{H}} B_S(S|\mathbf{H}|/k_B T)$, where $B_s(x)$ is the Brillouin function. We can eliminate $\langle \mathbf{s} \rangle$ from these mean-field equations by assuming that the band electron spin response is linear, i.e., that $\langle \mathbf{s} \rangle = J_{\rm ex} N_{\rm M} \chi_s \langle \mathbf{S} \rangle$, where χ_s is the electron spin susceptibility. The mean-field critical temperature is determined by solving self-consistently for $\mathbf{S}$ and yields a critical temperature proportional to χ_s. This mean-field theory is accurate when the static response of the momentum-dependent spin susceptibility is peaked near zero wave vector (Jungwirth *et al.*, 2006).

In the Zener picture, the ferromagnetic critical temperature is proportional to the square of the exchange coupling $J_{\rm ex}$ and the first power of the electron spin susceptibility χ_s. For transition-metal local moments, the exchange coupling $J_{\rm ex}$ originates from hybridization between metal d electrons and the p orbitals of the host compounds (Zener, 1951). Strong hybridization between the p orbitals of Te atoms and the d orbitals of transition-metal magnetic impurities has been demonstrated experimentally in Cr- or V-doped $(\mathrm{Bi,Sb})_2\mathrm{Te}_3$ (Tcakaev *et al.*, 2020). When the band system is metallic, the electron spin susceptibility is usually dominated by the Fermi level Pauli response, which induces Ruderman-Kittel-Kasuya-Yosida (RKKY) type (Ruderman and Kittel, 1954; Kasuya, 1956; Yosida, 1957) interactions between the local moments. However, the QAH effect requires the band system to be insulating. Because the electron spin operator has large interband matrix elements in systems with strong SOC, the electron spin susceptibility χ_s can be nonzero and large when gaps are small. This mechanism for induced coupling between local moments is known as the Van Vleck (Van Vleck, 1932) (or Bloembergen-Rowland) mechanism (Bloembergen and Rowland, 1955). Therefore, the Van Vleck mechanism can give rise to ferromagnetism in insulating magnetically doped TIs (Yu *et al.*, 2010; Li, Chang *et al.*, 2015), and in this way allows for the realization of the QAH effect.

The situation in real materials is, as usual, more complex. The magnetic properties of magnetically doped TIs are sensitive to the chemical composition, the types and locations of magnetic impurities and other unintended defects, the energies of the d orbitals of the magnetic impurities, and even the external gate voltages. Motivated by the observation that insulating ferromagnetism survives in density functional theory (DFT) calculations even when SOC is set to zero, Kim, Jhi *et al.* (2017) suggested that the segregation of magnetic dopants on the group III sites of $(\mathrm{Bi/Sb})_2(\mathrm{Se/Te})_3$ plays a crucial role in favoring magnetic order. Furthermore, a finite carrier concentration is normally present in the $(\mathrm{Bi/Sb})_2(\mathrm{Se/Te})_3$ TIs and, along with carriers in the TSSs, can induce a ferromagnetic RKKY interaction on surfaces (Liu *et al.*, 2009). Moreover, d orbitals may appear inside the bulk gap of TIs for several compounds, such as V-doped $(\mathrm{Bi,Sb})_2\mathrm{Te}_3$ (Peixoto *et al.*, 2016), and form impurity bands near E_F (Zhang *et al.*, 2018). This can lead either to a ferromagnetic superexchange mechanism when E_F lies in

the gap between the lower and upper crystal-field-split majority-spin bands, as in the case of (Ga,V)As, or to a Zener double exchange mechanism when a finite d-orbital density of states appears at E_F, as in the case of (Ga,Mn)N (Jungwirth *et al.*, 2006; Sato *et al.*, 2010). In addition, the spatial randomness of magnetic impurities may require a magnetic percolation picture. Experiments have revealed superparamagnetic dynamics in which magnetic impurities are clustered in nearly independent magnetic islands with a size of tens of nanometers (Chang *et al.*, 2014; Grauer *et al.*, 2015; Lachman *et al.*, 2015; Liu *et al.*, 2016).

2. Intrinsic magnetic TIs

$MnBi_2Te_4$ is a stoichiometric compound with Mn local moments that form strong bonds with neighboring Te atoms located at the center of a weakly coupled septuple layer. Both the higher density of Mn local moments and the absence of intended randomness offer potential advantages over magnetically doped TIs. The Mn local moments have a valence $+2$ by losing two $4s$ electrons, and the remaining five $3d$ electrons give rise to an isotropic fully spin-polarized $5\mu_B$ local moment. Since the majority-spin d levels of Mn are fully filled and the minority-spin d levels are completely unoccupied, the superexchange mechanism plays an essential role in $MnBi_2Te_4$ (Otrokov *et al.*, 2017; J. Li *et al.*, 2019; Śliwa *et al.*, 2021). In the superexchange mechanism (Anderson, 1950), virtual electron transfer between two cations through an intermediate nonmagnetic anion couples the magnetic moments of the cations.

The superexchange interaction can be ferromagnetic or antiferromagnetic, depending on the relative angle between two cation-anion bonds, according to the Goodenough-Kanamori rules (Goodenough, 1955; Kanamori, 1959). In $MnBi_2Te_4$, two neighboring Mn atoms in one septuple layer are coupled through the adjacent Te atoms and the angle of two Mn–Te bonds is around 86°, close to 90°. Thus, the intralayer superexchange between two Mn atoms is ferromagnetic. In contrast, the coupling between two Mn magnetic moments in two adjacent septuple layers is mediated by several intermediate Te or Bi atoms and is of antiferromagnetic type since all the cation-anion bonds are roughly along the z direction. Therefore, $MnBi_2Te_4$ has intrinsic A-type antiferromagnetism, namely, intralayer ferromagnetism and interlayer antiferromagnetism. $MnBi_2Te_4$ is only one member of a large family of compounds $Mn(Bi/Sb)_{2n}(Se/Te)_{3n+1}$ in which the $Mn(Bi/Sb)_2(Se/Te)_4$ and $(Bi/Sb)_{2(n-1)}(Se/Te)_{3(n-1)}$ layers alternate and form a superlattice structure. More properties of the $Mn(Bi/Sb)_{2n}(Se/Te)_{3n+1}$ family of materials are discussed in Sec. IV.A.

3. Magnetism in moiré materials

In graphene and TMD multilayer materials, the carriers are often concentrated near the two inequivalent triangular lattice BZ corners, referred to as valleys, that transform into each other under TR symmetry. Currently all moiré material QAH states have valley-projected moiré bands with broken TR symmetry and nonzero Chern numbers. QAH states then appear when opposite valleys have different total filling factors. The mechanism that favors ground states with spontaneous valley polarization is itinerant electron exchange interactions, the same interactions that are responsible for ferromagnetism in many metals. Because of the long-range nature of Coulomb interactions, itinerant electron exchange is stronger between states that are close together in momentum space, i.e., in the same valley. Maximizing the magnitude of attractive itinerant electron exchange interactions competes with a minimization of band energy, which has lesser importance when the bands are narrow.

Occupying states in momentum space in a way that violates TR symmetry allows broken TR symmetry observables that depend only on orbital degrees of freedom to be nonzero, even when SOC is weak. The AH effect is an example of such a physical quantity and can be grouped in this sense with orbital magnetization (Xiao, Chang, and Niu, 2010; Thonhauser, 2011; Aryasetiawan and Karlsson, 2019) (see Sec. V.B) and magneto-optical observables like the Kerr and Faraday effects. The origin of the AH effect and the QAH effect in moiré materials is distinct from its origin in systems like magnetic TIs that rely on SOC combined with spin ferromagnetism.

The evaluation of orbital magnetization in periodic crystals is more subtle than the evaluation of spin magnetism because the electron position operator is ill defined for extended Bloch wave functions (Xiao, Chang, and Niu, 2010; Thonhauser, 2011; Aryasetiawan and Karlsson, 2019). As in the modern theory of charge polarization, orbital magnetization can be related to Bloch state Berry phases that can be evaluated using tight-binding models based on maximally localized Wannier functions. (Thonhauser *et al.*, 2005; Ceresoli *et al.*, 2006; Bianco and Resta, 2013). The connection between orbital magnetization and Bloch state Berry phases can be established by examining semiclassical wave-packet dynamics (Xiao, Shi, and Niu, 2005; Xiao, Chang, and Niu, 2010) or using linear-response theory (Shi *et al.*, 2007).

The general expression for the orbital magnetization $\mathbf{M}_{\rm orb}$ of Bloch bands includes two contributions: a local circulation contribution $\mathbf{M}_{\rm orb,L}$ that comes from atomic orbital moments and an itinerant contribution $\mathbf{M}_{\rm orb,I}$ that originates from the free current flowing at the boundary of the finite system (Thonhauser *et al.*, 2005). A different decomposition of the orbital magnetization into distinct partial contributions, one from self-rotation of the wave packet and the other due to center-of-mass motion, arises naturally in the semiclassical wave-packet formalism (Xiao, Chang, and Niu, 2010). The itinerant contribution $\mathbf{M}_{\rm orb,I}$ is of particular interest since it is directly related to the Hall conductivity. In Chern insulators (Ceresoli *et al.*, 2006; Zhu, Su, and MacDonald, 2020), the itinerant contribution $\mathbf{M}_{\rm orb,I}$ is produced by currents that circulate around the sample boundary and are related to the quantized Hall conductivity and the associated band Chern numbers C via

$$\frac{dM_{\rm orb,I}}{d\mu} = \frac{Ce}{h}, \tag{9}$$

where μ is the chemical potential. In fact, most experimental measurements of the QH effect can be viewed (MacDonald, 1994) as direct measurements of the left-hand side of Eq. (9).

III. MAGNETICALLY DOPED TIs

A. Material properties

Crystals in the $(Bi/Sb)_2(Se/Te)_3$ family share the same rhombohedral crystal structure with the space group D_{3d}^5 ($R\bar{3}m$) with five atoms in one layer, as shown in Fig. 3(a). These five-atom layers arranged along the z direction are known as quintuple layers (QLs). Each QL consists of three Se/Te layers and two Bi/Sb layers. Among the four stoichiometric members, Bi_2Se_3, Bi_2Te_3, and Sb_2Te_3 are topologically nontrivial, whereas Sb_2Se_3 is a trivial insulator due to its weaker SOC. In TI films, the TSSs at the top and bottom surfaces hybridize with each other and open a gap that shrinks exponentially with film thickness. The gaps become unobservably small at around six QLs in Bi_2Se_3 (Zhang *et al.*, 2010; Chang *et al.*, 2011), two QLs in Bi_2Te_3 (Y.-Y. Li *et al.*, 2010), and four QLs in Sb_2Te_3 (Wang *et al.*, 2010; Jiang, Wang *et al.*, 2012). Ferromagnetic order can be introduced in TIs via three different routes: (i) dilute magnetic doping of a TI, i.e., introducing magnetic ions into TI materials; (ii) discovery of single-crystal materials that host coexisting topological and magnetic states intrinsically; and (iii) fabrication of TI–ferromagnetic insulator heterostructures. Approach (i) was the first to be successful, while approach (ii) has also been achieved in thin films exfoliated from the bulk intrinsic magnetic TI $MnBi_2Te_4$ (Deng *et al.*, 2020); see Sec. IV. Despite significant efforts, approach (iii) has not yet been fully successful. A large AH effect (and even the QAH effect) has been claimed to be observed in MBE-grown $Cr_2Ge_2Te_6/(Bi,Sb)_2Te_3/Cr_2Ge_2Te_6$ (Mogi *et al.*, 2019) and $(Zn,Cr)Te/(Bi,Sb)_2Te_3/(Zn,Cr)Te$ sandwiches (Watanabe *et al.*, 2019). We noticed that the ferromagnetic layers in both systems include the element Cr. When the MBE growth of these sandwich samples was performed at high temperatures, Cr diffusion inevitably occurs between the middle $(Bi,Sb)_2Te_3$ and the Cr-based ferromagnetic surface layers. The QAH effect realized in MBE-grown $(Zn,Cr)Te/(Bi,Sb)_2Te_3/(Zn,Cr)Te$ sandwich heterostructures might indicate success of approach (i) [i.e., Cr-doped $(Bi,Sb)_2Te_3$] instead of approach (iii). This section focuses on approach (i).

Transition-metal element doping is a convenient approach for inducing long-range ferromagnetic order in TIs [Fig. 3(a)] (Chien, Zhou, and Uher, 2005; Zhou, Chien, and Uher, 2005, 2006; Hor *et al.*, 2010). The ordering mechanism is analogous to that in conventional dilute magnetic semiconductors (Ohno, 1999; Ohno *et al.*, 2000; Jungwirth *et al.*, 2006; Sato *et al.*, 2010; Dietl and Ohno, 2014), as discussed in Sec. II.B. In Cr-doped $(Bi/Sb)_2(Se/Te)_3$, scanning tunneling microscopy (STM) studies have demonstrated that Cr atoms usually substitute for Bi/Sb atoms [Fig. 3(a)] (Chang *et al.*, 2013b, 2014; Jiang *et al.*, 2015; Lee *et al.*, 2015; Zhang *et al.*, 2018). In the following, we compare the properties of Cr-doped Bi_2Se_3, Bi_2Te_3, and Sb_2Te_3 and explain why one is preferred as the parent material for the realization of the QAH effect. It turns out that the magnetic properties in these three TI compounds are highly sensitive to inhomogeneity of the Cr impurities. In Cr-doped Bi_2Se_3 thin films, no long-range ferromagnetic order has been observed down to $T = 1.5$ K [Fig. 3(b)] (Chang *et al.*, 2013b; Zhang *et al.*, 2013). The nonlinear Hall traces at low temperatures reflect the presence of weakly coupled superparamagnetic multimers formed by aggregated substitutional Cr atoms in Bi_2Se_3 matrices [Fig. 3(e)]. The appearance of a large gap opening at the Dirac point in Cr- and Fe-doped Bi_2Se_3 might also reflect substitutional Cr or Fe aggregations (Chen *et al.*, 2010;

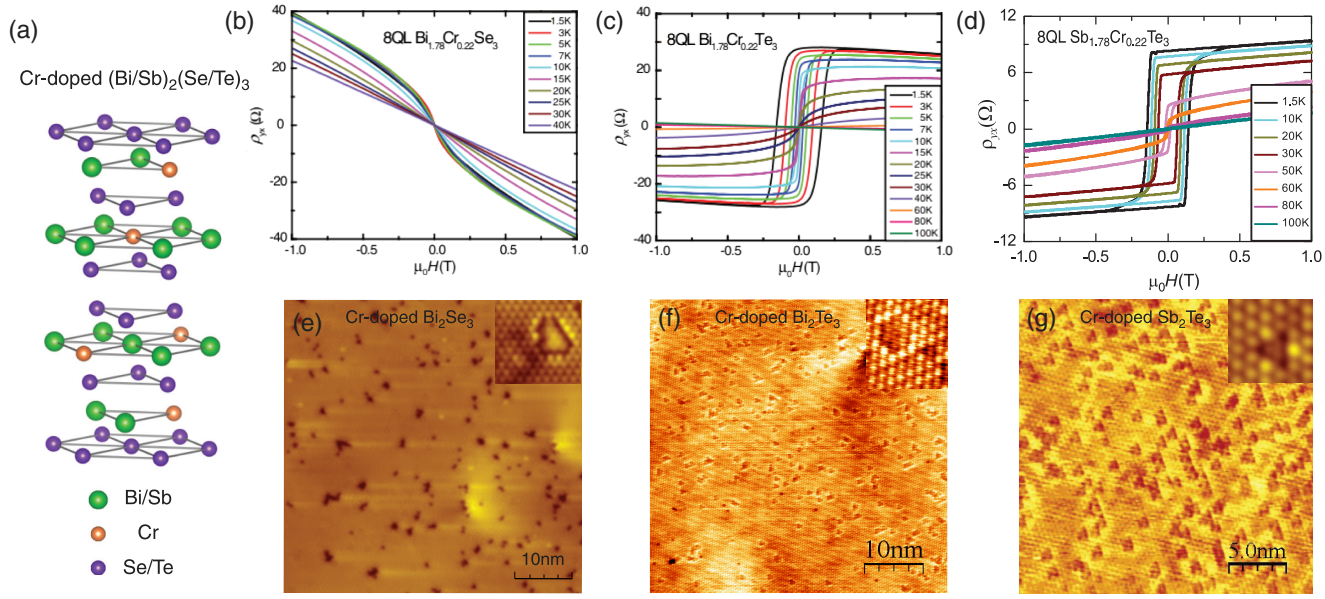

FIG. 3. Magnetically doped TI films. (a) Schematic structure of Cr-doped $(Bi/Sb)_2(Se/Te)_3$. Hall traces of eight QL (b) $Bi_{1.78}Cr_{0.22}Se_3$, (c) $Bi_{1.78}Cr_{0.22}Te_3$, and (d) $Sb_{1.78}Cr_{0.22}Te_3$ films. STM images of Cr-doped (e) Bi_2Se_3, (f) Bi_2Te_3, and (g) Sb_2Te_3. From Chang *et al.*, 2013b2014, and Zhang *et al.*, 2013.

Chang *et al.*, 2014). The absence of long-range ferromagnetic order due to inhomogeneity rules out Cr-doped Bi_2Se_3 as a candidate for the realization of the QAH effect. In contrast, both Cr-doped Bi_2Te_3 and Cr-doped Sb_2Te_3 exhibit pronounced hysteresis loops [Figs. 3(c) and 3(d)], demonstrating robust long-range ferromagnetic order in both materials (Zhang *et al.*, 2013; Chang, Liu *et al.*, 2016). Compared to Cr-doped Bi_2Te_3, Cr-doped Sb_2Te_3 has a much better ferromagnetic order as seen by a more square hysteresis loop at low temperatures [Fig. 3(d)]. STM measurements find that three Cr atom aggregations are common in Bi_2Te_3 [Fig. 3(f)]. Overall Cr doping homogeneity is better in Cr-doped Sb_2Te_3 films [Fig. 3(g)] (Chang *et al.*, 2013b). Doping homogeneity is the key ingredient for the long-range ferromagnetic order, as well as for the quality of the QAH state in magnetically doped TIs discussed in the following. Therefore, both transport and STM results suggest Cr-doped Sb_2Te_3 as a promising parent material for the realization of the QAH effect (Chang *et al.*, 2013a, 2013b; Chang, Liu *et al.*, 2016).

B. Realization of the QAH effect in magnetically doped TIs

1. QAH effect in Cr-doped TIs

Cr-doped Bi_2Te_3 and Sb_2Te_3 films both have large carrier densities because of common defects that act as donors or acceptors. The QAH effect could be achieved only after a systematic and careful exploration of the relationship between unintended doping and stochiometry (Chang *et al.*, 2013a, 2013b). In Cr-doped Sb_2Te_3, doping Bi can reduce the high hole carrier density (Chang *et al.*, 2013b; Chang, Liu *et al.*, 2016). The QAH effect was first realized in five QL $Cr_{0.15}(Bi,Sb)_{1.85}Te_3$ thin films on heat-treated $SrTiO_3(111)$ on October 9, 2012 (Chang *et al.*, 2013a). Figures 4(a) and 4(b) show the magnetic-field $\mu_0 H$ dependence of ρ_{yx} and ρ_{xx}, respectively, measured at $T \sim 30$ mK for various bottom gate biases V_g. The shape and the coercive fields of the AH hysteresis loops are nearly independent of V_g, indicating a carrier-independent ferromagnetic order (Chang *et al.*, 2013a; Chang *et al.*, 2013b). The zero-magnetic-field AH resistance $\rho_{yx}(0)$ changes dramatically with V_g, showing a maximum value of h/e^2 ($\sim$25.8 kΩ) at the charge neutral point $V_g = V_g^0$. The $\mu_0 H$ dependence of ρ_{xx} exhibits the typical hysteretic shape commonly observed in conventional ferromagnetic materials.

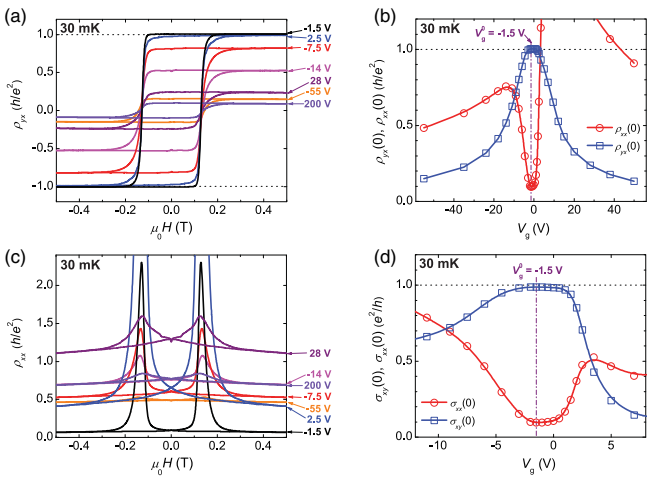

FIG. 4. Experimental realization of the QAH effect in five QL Cr-doped $(Bi,Sb)_2Te_3$ films. Magnetic-field $\mu_0 H$ dependence of (a) the Hall resistance ρ_{yx} and (c) the longitudinal resistance ρ_{xx} at different V_g's. (b) Gate dependence of the zero-magnetic-field Hall resistance $\rho_{yx}(0)$ (blue square) and the zero-magnetic-field longitudinal resistance $\rho_{xx}(0)$ (red circle). (d) Gate dependence of the zero-magnetic-field Hall resistance $\sigma_{xy}(0)$ (blue square) and the zero-magnetic-field longitudinal resistance $\sigma_{xx}(0)$ (red circle). From Chang *et al.*, 2013a.

The most important observation, that the Hall resistance exhibits a distinct plateau with the quantized value h/e^2 at zero magnetic field, is shown in Fig. 4(b). Concomitant with the ρ_{yx} plateaus, the zero-magnetic-field longitudinal resistance $\rho_{xx}(0)$ shows a dip, reaching a value of $0.098h/e^2$, yielding a Hall angle θ of $\sim$84.4°. For comparison with theory, we convert $\rho_{yx}(0)$ and $\rho_{xx}(0)$ into the sheet conductances $\sigma_{xy}(0)$ and $\sigma_{xx}(0)$ [Fig. 4(d)]. $\sigma_{xy}(0)$ exhibits a notable plateau at $0.987e^2/h$, while $\sigma_{xx}(0)$ exhibits a dip down to $0.096e^2/h$. These results mark the first experimental realization of the QAH effect. Note that the deviation of $\sigma_{xy}(0)$ from e^2/h and nonzero $\sigma_{xx}(0)$ can be attributed to residual dissipative channels in the sample, which are expected to vanish completely at zero temperature or under a high magnetic field. By applying a magnetic field, Chang *et al.* (2013a) did see near perfect quantization of ρ_{yx} and vanishing ρ_{xx}. The observation of a QAH effect in MBE-fabricated Cr-doped TI thin films was relatively quickly reproduced by many others (Checkelsky *et al.*, 2014; Kou *et al.*, 2014; Bestwick *et al.*, 2015; Kandala *et al.*, 2015; Lachman *et al.*, 2015; Liu *et al.*, 2016; Kawamura *et al.*, 2017), who used film thicknesses ranging from five to ten QLs on various substrates, including $SrTiO_3(111)$, $InP(111)$, and $GaAs(111)$. We review the physical properties of the QAH state in Cr-doped TI system in Sec. III.C.

Despite much effort, the critical temperature of the QAH state in Cr-doped TI films [Fig. 5(a)] is still limited to $\sim$2 K, which is an order of magnitude lower than the value of their Curie temperature T_C (Chang *et al.*, 2013a; Checkelsky *et al.*, 2014; Kou *et al.*, 2014; Bestwick *et al.*, 2015; Kandala *et al.*, 2015; Lachman *et al.*, 2015; Feng *et al.*, 2016; Liu *et al.*, 2016; Kawamura *et al.*, 2017). This difference is presumably due to the following two effects: (i) In magnetically doped TI films, the magnetic dopants may induce spatial fluctuations of the chemical potential and the exchange coupling across the film, and thus make the effective excitation gap much smaller than the average magnetic exchange gap (Chang, Zhao *et al.*, 2016), thereby enhancing the role of thermal fluctuations (Li and Cheng, 2021; W. Lin *et al.*, 2022). (ii) The energy of the Dirac point of the surface states in $(Bi,Sb)_2Te_3$ is close to or even buried in the bulk valence band maximum along the Γ-M direction (Chang, Zhao, Kim, Wei *et al.*, 2015; W. Li *et al.*, 2016; W. Wang *et al.*, 2018).

Different metrics have been used in the literature to identify the critical temperature of QAH insulators. In this Colloquium, we define the critical temperature of the QAH state as that at which the $\rho_{yx}(0)/\rho_{xx}(0)$ ratio is greater than 1. The low critical temperature not only impedes quantitative

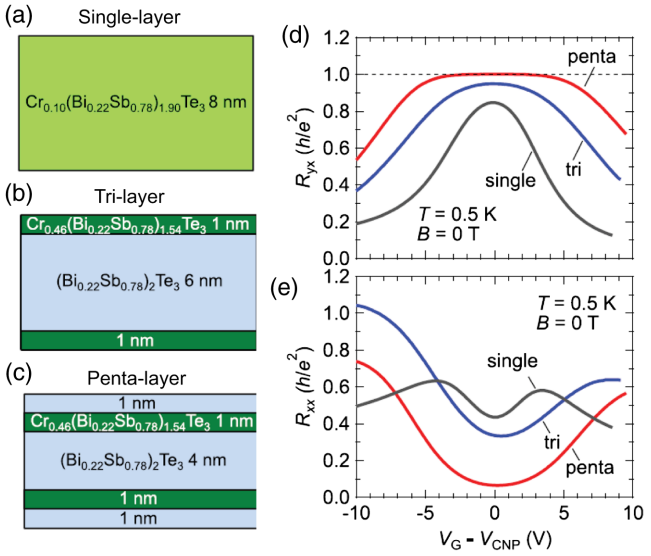

FIG. 5. Higher temperature QAH effects in TI heterostructures with modulation magnetic doping. Schematics are shown for different Cr-doping geometries: (a) uniformly doped, (b) Cr-doped TI trilayer, and (c) pentalayer. Gate dependence of (d) the Hall resistance R_{yx} and (e) the longitudinal resistance R_{xx} of the three samples shown in (a)–(c) measured at $T = 0.5$ K. From Mogi *et al.*, 2015.

studies of the QAH state, examination of the scaling behaviors of the plateau transitions (Checkelsky *et al.*, 2014; Kou *et al.*, 2014), and current-induced QAH breakdown (Kawamura *et al.*, 2017; Fox *et al.*, 2018) but also limits potential applications for electronic and spintronic devices with low power consumption.

Mogi *et al.* (2015) found that magnetic Cr modulation doping $(Bi, Sb)_2Te_3$ to form trilayer and pentalayer heterostructures can enhance the critical temperature of the QAH effect. By introducing two 1 nm thick heavily-Cr-doped $(Bi, Sb)_2Te_3$ layers near the top and bottom surfaces of a 6 nm nonmagnetic $(Bi, Sb)_2Te_3$ layer to form trilayer and pentalayer heterostructures [Figs. 5(a)–5(c)], they could achieve a better QAH state with a higher critical temperature [Figs. 5(d) and 5(e)]. At $T = 0.5$ K and the charge neutral point ($V_g = V_g^0$), the zero-magnetic-field Hall resistance $\rho_{yx}(0)$ is $\sim 0.85h/e^2$, $\sim 0.95h/e^2$, and $\sim 1h/e^2$ for the single-layer, trilayer, and pentalayer heterostructure samples, respectively. The monotonic decrease of the zero-magnetic-field longitudinal resistance $\rho_{xx}(0)$ further confirms that a better QAH state is achieved. In these modulation-doped trilayer and pentalayer heterostructure samples, the fluctuation of the magnetic exchange gap on the sample surfaces is apparently suppressed, and thus the effective magnetic exchange gap becomes larger, leading to a critical temperature ~ 10 K (Mogi *et al.*, 2015). We note that the heavily-Cr-doped $(Bi, Sb)_2Te_3$ layers used in the trilayer and pentalayer samples may drive the systems to a trivial ferromagnetic insulator state due to the reduction of SOC as a result of the heavy Cr doping in $(Bi, Sb)_2Te_3$ (Zhang *et al.*, 2013; Zhao *et al.*, 2020), which is further discussed in Sec. III.D.

Okada *et al.* (2016) performed terahertz Faraday and Kerr rotation measurements on pentalayer QAH samples and found that the Faraday and Kerr rotation angles quantitatively agree with the estimates based on electrical transport measurements. QAH trilayer samples have also been used in scaling studies of the plateau to plateau transitions (Kawamura *et al.*, 2018, 2020). More recently, motivated by this modulation doping method, Jiang *et al.* (2020) fabricated three QL Cr-doped $(Bi, Sb)_2Te_3$/five QL $(Bi, Sb)_2Te_3$/three QL Cr-doped $(Bi, Sb)_2Te_3$ sandwich structures and observed the concurrence of the topological Hall effect and the QAH effect through electric field gating. This concurrence indicates an interplay between the chiral edge states and chiral spin textures in magnetic TI heterostructures.

2. QAH effect in V-doped TIs

First-principles calculations by Yu *et al.* (2010) suggested that QAH insulators should occur in thin films of TIs with Cr or Fe doping, whereas the QAH state was expected to be absent for Ti or V doping because of *d*-electron impurity bands at the Fermi surface. Chang, Zhao, Kim, Zhang *et al.* (2015) found that among all 3*d* transition-metal elements (Chien, Zhou, and Uher, 2005; Zhou, Chien, and Uher, 2005, 2006; Hor *et al.*, 2010) V-doped Sb_2Te_3 exhibits the most robust ferromagnetic order. Following a strategy similar to that employed earlier for Cr-doped QAH samples (Chang *et al.*, 2013a), a high-precision QAH effect was observed in a four QL V-doped $(Bi, Sb)_2Te_3$ film [Fig. 6(a)] (Chang, Zhao, Kim, Wei *et al.*, 2015; Chang, Zhao, Kim, Zhang *et al.*, 2015). The QAH effect in V-doped TI systems was later replicated by others (Grauer *et al.*, 2015, 2017; Ou *et al.*, 2018; Lippertz *et al.*, 2022).

For both Cr- and V-doped $(Bi, Sb)_2Te_3$ films, the Curie temperature T_C strongly depends on the magnetic doping concentration x. The maximum value of T_C can be greater than 100 K in heavily Cr- and/or V-doped Sb_2Te_3 films (Zhou, Chien, and Uher, 2005, 2006; Chang, Zhao, Kim,

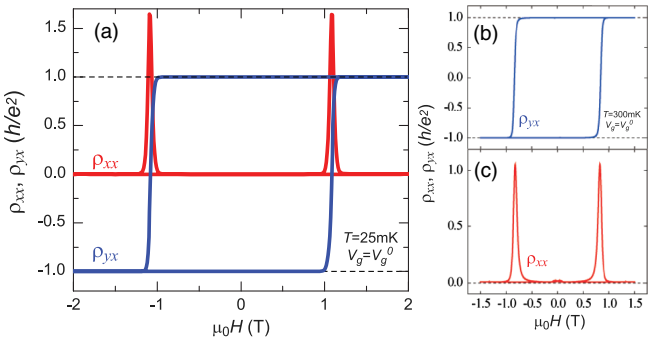

FIG. 6. QAH effect in V-doped $(Bi, Sb)_2Te_3$ films and Cr/V codoped $(Bi, Sb)_2Te_3$ films. (a) Magnetic-field dependence of the Hall resistance ρ_{yx} (blue curves) and the longitudinal resistance ρ_{xx} (red curves) of four QL V-doped $(Bi, Sb)_2Te_3$ films at the charge neutral point $V_g = V_g^0$ and temperature $T = 25$ mK. Magnetic-field dependence of (b) ρ_{yx} and (c) ρ_{xx} of five QL Cr/V codoped $(Bi, Sb)_2Te_3$ films at the charge neutral point $V_g = V_g^0$ and $T = 300$ mK. From Chang, Zhao, Kim, Zhang *et al.*, 2015, and Ou *et al.*, 2018.

Zhang *et al.*, 2015). However, heavy Cr- and/or V-doping greatly reduces the SOC of the magnetically doped TI and drives it into a trivial insulator state (Zhang *et al.*, 2013; Chang *et al.*, 2014; Zhao *et al.*, 2020, 2022).Therefore, an optimal Cr- and/or V-doping concentration x is required. The values of magnetic doping concentration x are usually different in different groups worldwide, but the T_C value of samples that exhibit the QAH effect is usually in a range of 15–30 K. Compared to Cr-doped Sb_2Te_3, the two main advantages of V-doped Sb_2Te_3 are (i) higher Curie temperature T_C, which is almost double that of Cr-doped Sb_2Te_3 at the same doping level x, and (ii) larger coercive field H_c, which is about an order larger than that of the Cr-doped Sb_2Te_3 with the same doping level at a fixed temperature (Chang, Zhao, Kim, Zhang *et al.*, 2015).

Figure 6(a) shows a nearly ideal QAH state in a four QL $V_{0.11}(Bi,Sb)_{1.89}Te_3/SrTiO_3(111)$ film. At the charge neutral point $V_g = V_g^0$, the zero-magnetic-field Hall resistance $\rho_{yx}(0)$ is $\sim(1.000\,19 \pm 0.000\,69)h/e^2$ $(25.8178 \pm 0.0177\ \mathrm{k\Omega})$, while the zero-magnetic-field longitudinal resistance $\rho_{xx}(0)$ is as low as $\sim(0.000\,13 \pm 0.000\,07)h/e^2$ $(\sim 3.35 \pm 1.76\ \Omega)$ measured at $T = 25$ mK. The ratio $\rho_{yx}(0)/\rho_{xx}(0)$ corresponds to an AH angle $\sim 89.993 \pm 0.004°$. The corresponding Hall conductance at zero magnetic field $\sigma_{yx}(0)$ is $\sim(0.9998 \pm 0.0006)e^2/h$ and the corresponding longitudinal conductance $\sigma_{xx}(0)$ is $\sim(0.000\,13 \pm 0.000\,07)e^2/h$ (Chang, Zhao, Kim, Zhang *et al.*, 2015). The critical temperature of the QAH state in the V-doped TI system is around 1 K. Measuring the gate and temperature dependence of local and nonlocal magnetoresistance, Chang, Zhao, Kim, Wei *et al.* (2015) established the presence of dissipationless chiral edge transport in this system in the absence of a magnetic field. By tuning the chemical potential, Chang, Zhao *et al.* (2016) also observed a quantum phase transition from a QAH insulator to an Anderson insulator. The critical scaling behavior of this topological quantum phase transition is discussed in Sec. III.C.4.

Grauer *et al.* (2015) synthesized ten QL V-doped $(Bi,Sb)_2Te_3$ films on hydrogen passivated Si(111) substrates and observed a coincidence of superparamagnetism and perfect quantization. The scaling behaviors of uniformly V-doped $(Bi,Sb)_2Te_3$ films of various thicknesses on Si(111) and InP(111) substrates have been studied and the QAH insulators have been classified as either 2D or 3D (Grauer *et al.*, 2017; Fijalkowski *et al.*, 2021). The different origins of the $(\sigma_{xy}, \sigma_{xx}) = (0, 0)$ point in scaling plots of individual magnetically doped QAH samples and magnetic TI sandwich samples are discussed in Sec. III.C.2.

As previously noted, the QAH effect has been demonstrated in both Cr- and V-doped $(Bi,Sb)_2Te_3$ films. Ou *et al.* (2018) synthesized five QL Cr and V codoped $(Bi,Sb)_2Te_3$ films with various Cr/V ratios and found a significant increase in the critical temperature of the QAH effect to around 10 K for $Cr/(Cr + V) \sim 0.16$. For the optimal Cr-to-V ratio, a codoped $(Bi,Sb)_2Te_3$ sample yielded $\rho_{yx}(0) \sim h/e^2$ to within experimental uncertainty and $\rho_{xx}(0) \sim 0.009h/e^2$ at $V_g = V_g^0$ and $T = 300$ mK [Figs. 6(b) and 6(c)]. At $T = 1.5$ K, $\rho_{yx}(0) \sim 0.97h/e^2$ and $\rho_{xx}(0) \sim 0.19h/e^2$. Such a quantization level has been observed only at $T \sim 100$ mK in either individual Cr-doped or V-doped QAH samples (Chang *et al.*, 2013a; Checkelsky *et al.*, 2014; Kou *et al.*, 2014; Chang, Zhao, Kim, Zhang *et al.*, 2015). The enhancement of the critical temperature of the QAH effect in Cr and V codoped QAH samples is attributed to an improvement of the homogeneity of the ferromagnetic order and a modulation of the sample band structure (Ou *et al.*, 2018).

A follow-up study combined magnetic force microscopy with electrical transport to reveal typical ferromagnetic domain behaviors in the Cr and V codoped QAH films, in contrast to the much weaker magnetic signals observed in either Cr-doped or V-doped QAH films (W. Wang *et al.*, 2018), possibly due to the role of local superparamagnetism (Grauer *et al.*, 2015; Lachman *et al.*, 2015). In addition, by studying a series of Cr and V codoped and individual Cr-doped QAH samples, Liu *et al.* (2020) found that the ground states of all samples can be categorized either as QAH insulators or as AH insulators. In the low-disorder limit, a universal quantum longitudinal resistance $\rho_{xx} = h/e^2$ is observed at the coercive field H_c of the QAH samples. Modulation doping (Sec. III.B.1) (Mogi *et al.*, 2015) and magnetic codoping (Ou *et al.*, 2018) are now established as techniques to enhance the critical temperature of the QAH effect in magnetically doped TI systems. The QAH critical temperatures of 5–10 K are regularly obtained.

C. Physical properties of the QAH states in magnetically doped TIs

Following the realization of the QAH effect in a Cr-doped TI system (Chang *et al.*, 2013a), close synergy between theory and experiment greatly advances our understanding of the QAH state. The QAH effect and the QH effect share the same topological properties, but their physical origins are different. The QH effect arises from the formation of Landau levels under high magnetic fields, and its realization relies on carrier mobility (Klitzing, Dorda, and Pepper, 1980) that is high enough to weaken mixing between different Landau levels, i.e., to make $\omega_c\tau \gg 1$ large where τ is the Bloch state lifetime, ω_c is the cyclotron frequency, and $\hbar\omega_c$ is the Landau level separation, which has a typical value ~ 1 meV. In contrast, the QAH effect in magnetically doped TIs is a consequence of an interplay between strong SOC and magnetic exchange interactions (Chang, 2020). The QAH effect can appear in materials with low carrier mobility (Chang *et al.*, 2013a; Chang, Zhao, Kim, Zhang *et al.*, 2015) since it requires only that $\Delta\tau \gg \hbar$, where Δ is the topologically nontrivial band gap. The energy scale Δ is set by SOC and exchange interactions in magnetically doped TIs and is normally on the order of hundreds of meV. The different physical origins of the QAH and QH states motivates studies of the physical properties of QAH states in magnetically doped TIs. This section reviews a variety of physical properties associated with QAH states, including, in particular, evidence for the coexistence of chiral and nonchiral edge states, the appearance of zero Hall conductance plateaus, and their relation to axion insulator states and the topological magnetoelectric (TME) effect, global phase diagrams, scaling behaviors, and current-induced breakdown properties.

1. Chiral and nonchiral edge states

The QH effect and the QAH effect are both characterized by electric currents that flow along sample edges in equilibrium thanks to topologically protected chiral edge states. In both cases, the microscopic physics of the edge states can be complex. We focus here on the peculiarities of the edge state systems associated with the QAH state in magnetically doped TIs. As the mobility of magnetically doped TIs is several orders smaller than that in typical QH systems, disorder scattering is usually much stronger in the QAH system.

The energy of the Dirac point of TSSs in parent $(Bi, Sb)_2Te_3$ compounds is close to the valence band maximum (Chang, Zhao, Kim, Wei *et al.*, 2015; W. Li *et al.*, 2016; W. Wang *et al.*, 2018). It follows that disordered bulk transport likely coexists with edge transport in magnetically doped devices. When the magnetization is perpendicular to the thin film plane, the TSSs remain gapless on the side surfaces of TI films and give rise to an edge state system that contains a number of channels proportional to the film thickness (Wang *et al.*, 2013). Both the residual bulk carriers and the multichannel edge state systems play a role in understanding the experimental fact that the QAH effect in magnetically doped TIs sometimes shows a residual ρ_{xx} that is several kΩ, while ρ_{yx} is nearly quantized.

The presence of multichannel sidewalls was experimentally confirmed by performing the nonlocal transport measurements on both uniformly ten QL Cr-doped $(Bi, Sb)_2Te_3$ (Kou *et al.*, 2014) and uniformly four QL V-doped $(Bi, Sb)_2Te_3$ (Chang, Zhao, Kim, Wei *et al.*, 2015) Hall bar devices. In the absence of disorder, the wave vector along the sidewall is a good quantum number and the edge system can be separated into a single chiral channel and a set of nonchiral pairs. ρ_{yx} quantization is perfect when bulk transport is localized near the sidewalls, and the entire edge state system is in local equilibrium. Kou *et al.* (2014) showed that the nonlocal resistance is hysteretic, with both low-resistance and high-resistance states appearing during the magnetization reversal process, due to the interplay between edge and bulk channels. Chang, Zhao, Kim, Wei *et al.* (2015) further showed asymmetric behavior of local and nonlocal transport when the carrier type is tuned from electrons to holes through an external gate voltage, implying the dominant dissipative channels vary from quasihelical edge states to bulk states. Dissipation can occur because of transport across the bulk, or because the current-carrying multichannel edge system is not in local equilibrium. Recently Wang *et al.* (2020) performed more systematic temperature- and magnetic-field-dependent transport measurements on a three QL Cr-doped $(Bi, Sb)_2Te_3$/five QL $(Bi, Sb)_2Te_3$/three QL Cr-doped $(Bi, Sb)_2Te_3$ sandwich sample and concluded that in thick QAH samples the dominant dissipation mechanism switches between edge and bulk states in different magnetic-field regimes.

Another unique feature of magnetotransport in QAH materials is that the magnetization direction in a magnetic domain is locked not only to the Hall conductance but also to the propagation direction (i.e., clockwise or counterclockwise) of the chiral edge current. Chiral currents flow not only at sample edges but also along domain walls with opposing magnetization orientations. This property makes electrical probes sensitive to the motion of magnetic domain walls. Yasuda *et al.* (2017) utilized a magnetic force microscope to control the magnetization direction of a QAH sample with modulated magnetic doping and concluded that the observed nonlocal transport is consistent with chiral edge conduction along the walls in a written domain pattern. We note that direct imaging of magnetic domain walls is absent in these nonlocal transport measurements. Rosen *et al.* (2017) partially covered the QAH films with a bulk niobium superconductor and demonstrated chiral edge conduction along the magnetic domain walls via the Meissner-Ochsenfeld effect. Microwave impedance microscopy can directly image the distribution of chiral edge currents at the boundary and at magnetic domain walls in a QAH sample (Allen *et al.*, 2019). In addition, chiral edge states can also carry spin polarization (Zhang, Hsu, and Liu, 2016; Cheraghchi and Sabze, 2020) or form spin texture (Wu, Liu, and Liu, 2014), which implies that the chiral edge states can be utilized to control magnetic domain walls and drive a domain-wall motion (Upadhyaya and Tserkovnyak, 2016; Kim, Kurebayashi, and Nomura, 2019). The interplay between dissipationless chiral modes and magnetic domain walls in QAH insulators points to potential applications in spintronics if higher critical temperatures can be achieved.

2. Zero Hall conductance plateau and the axion insulator state

In uniformly doped thin films, the magnetization of a QAH sample reverses its sign at the coercive field H_c, and correspondingly the Hall conductance σ_{xy} will vary from e^2/h to $-e^2/h$ with a change of the Chern number C by 2. This scenario does not, however, exhaust the available phenomenology. In some devices, the system undergoes two separate topological phase transitions with each varying C by 1, and consequently an intermediate zero Hall conductance plateau (ZHCP) with $C = 0$ emerges in the magnetization reversal process.

Two scenarios can be identified for ZHCP formation in magnetic TI films. The first scenario assumes that the magnetization is uniform across the device so that the magnetic gaps, denoted as Δ_M here, for the TSSs on the top and bottom surfaces are the same. A finite hybridization (denoted as m_0) between two TSSs is considered, and when the magnetic domains in the sample are well aligned in the same direction, the magnetic gap Δ_M is dominant such that the system is in the QAH state with the Chern number $C = \Delta_M/|\Delta_M| = \pm 1$, depending on the sign of Δ_M. During the magnetization reversal process, the number of upward and downward oriented magnetic domains changes, and the spatially averaged magnetic gap continuously varies from positive to negative. This scenario applies when the typical domain size is small compared to the characteristic electronic length scale $\hbar v_D/\Delta_M$, allowing the nonuniform magnetization to be replaced by its spatial average. The topological phase transition between $C = 0$ and $|C| \neq 0$ states takes place at the gap closings when $|\Delta_0| = |m_0|$. When the hybridization gap is dominant ($|\Delta_0| < |m_0|$), the Chern number becomes $C = 0$, leading to a ZHCP. This scenario is more likely to apply in thinner TI films with a large hybridization between two TSSs (Feng *et al.*, 2015; Kou *et al.*, 2015). Since the hybridization between two TSSs declines

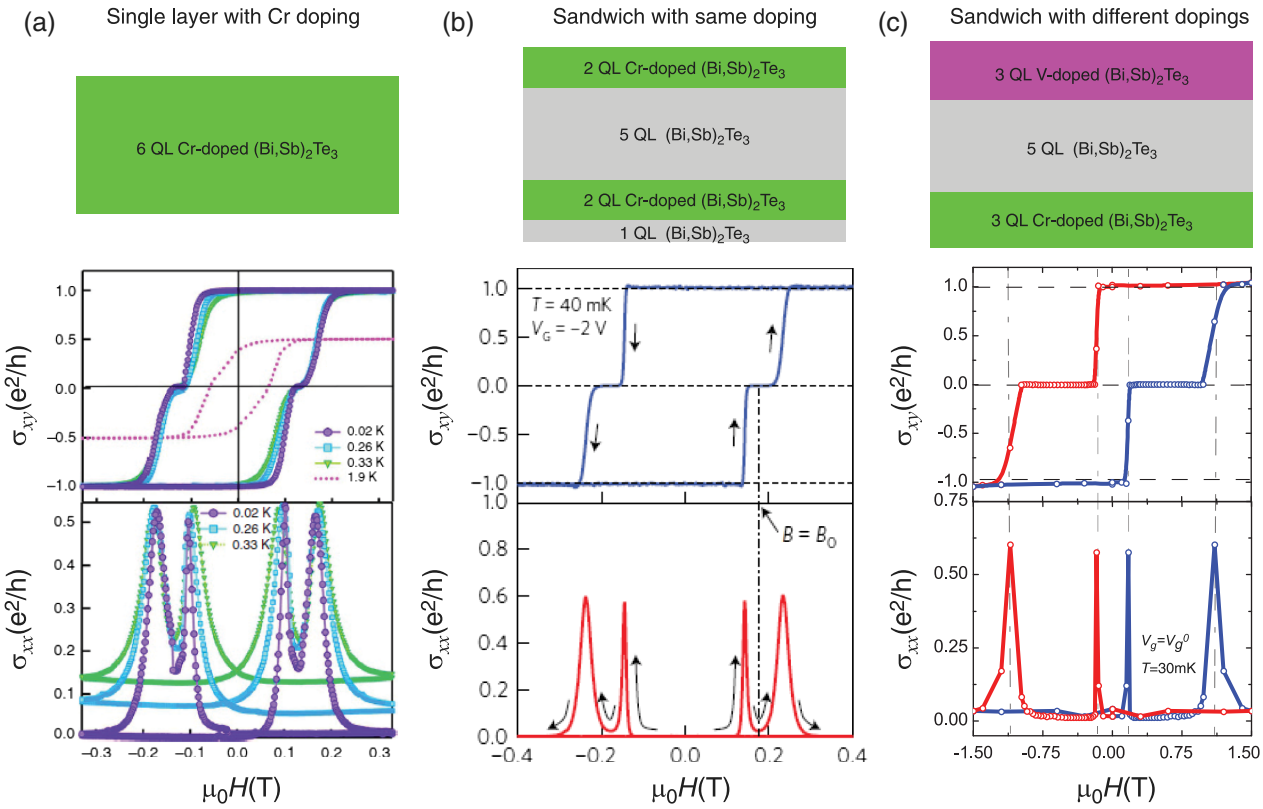

FIG. 7. Zero Hall conductance plateaus and axion insulator states in magnetic TI films and heterostructures. Top panels: schematics of a uniformly Cr-doped TI, a magnetic TI sandwich with the asymmetric Cr doping near the top and bottom surfaces, and a magnetic TI sandwich with magnetic doping with Cr and V. Bottom panels: magnetic-field $\mu_0 H$ dependence of the Hall conductance σ_{xy} and the longitudinal conductance σ_{xx} of (a) six QL Cr-doped $(Bi, Sb)_2Te_3$ films, (b) a two QL Cr-doped $(Bi, Sb)_2Te_3$/five QL $(Bi, Sb)_2Te_3$/two QL Cr-doped $(Bi, Sb)_2Te_3$/one QL $(Bi, Sb)_2Te_3$ heterostructure, and (c) a three QL V-doped $(Bi, Sb)_2Te_3$/five QL $(Bi, Sb)_2Te_3$/three QL Cr-doped $(Bi, Sb)_2Te_3$ heterostructure. From Kou *et al.*, 2015, Mogi, Kawamura, Yoshimi *et al.*, 2017, and Xiao *et al.*, 2018.

exponentially with increasing TI film thickness and samples always have some disorder, this picture becomes untenable beyond a relatively small number of layers. On the other hand, with increasing film thickness the magnetism in the two surface regions is more weakly coupled, and modulation doping makes it possible to design devices in which the two coercive fields differ. This leads to an alternative scenario for the ZHCP. When the magnetic gap for the top TSS has the opposite sign of the bottom TSS, the two TSSs give opposing contributions to the Hall conductivity, and this leads to a ZHCP (Wang, Lian, and Zhang, 2014; Mogi, Kawamura, Tsukazaki *et al.*, 2017; Xiao *et al.*, 2018). When ZHCP states are observed in magnetic sandwiches, both sidewall and bulk quasiparticles must be absent at the Fermi level, or if present must be localized. ZHCP states therefore can be viewed as a special subclass of normal 2D insulators, or, in the case where localized states are present, as Anderson insulators. However, they still have broken TR symmetry and, as we later discuss, are expected to exhibit properties that are related to the TME effect, a characteristic of bulk 3D TIs.

Soon after the theoretical predictions (Wang, Lian, and Zhang, 2014), two experimental groups separately reported ZHCP observations in five and six QL uniformly Cr-doped $(Bi, Sb)_2Te_3$ films [Fig. 7(a)] (Feng *et al.*, 2015; Kou *et al.*, 2015). Given the uniform magnetization, the observed ZHCPs are likely to have their origin from the hybridization gap. Experimental identifications of ZHCP states can be somewhat ambiguous because measurements are always performed at finite temperatures where insulating behaviors are not fully developed. Examinations of the Hall conductivity and resistivity related by $\sigma_{xy} = \rho_{yx}/(\rho_{xx}^2 + \rho_{yx}^2)$ can give different impressions. σ_{xy} is small whenever ρ_{xx} at H_c is much greater than the quantized ρ_{yx}. This can result in the appearance of a zero σ_{xy} plateau but no zero ρ_{yx} plateau at H_c. Indeed, pronounced ZHCPs are found in disordered five QL Cr-doped $(Bi, Sb)_2Te_3$ films (Feng *et al.*, 2015) but are usually absent in magnetically doped QAH samples with higher quality (Chang, Zhao, Kim, Zhang *et al.*, 2015). The appearance of ZHCP plateaus also depends strongly on MBE growth conditions. For six QL Cr-doped $(Bi, Sb)_2Te_3$ films from the same group, some samples show the ZHCP [Fig. 7(a)] (Kou *et al.*, 2014), while others that have relatively small ρ_{xx} at H_c do not (Rosen *et al.*, 2017). For the hybridization-gap-induced ZHCP, Haim, Ilan, and Alicea (2019) pointed out that strong magnetic disorder can drive the system into a new topological state supporting helical edge modes that are protected by crystalline reflection symmetry instead of TR symmetry. This phenomenon is called the "quantum anomalous parity Hall effect" but is not yet supported by experimental evidence.

In the literature, the observation of ZHCPs in 2D magnetic TI thin films has always been connected to the concept of axion insulator states, a moniker motivated by the TME effect, a characteristic property of 3D TIs (Wilczek, 1987; Qi, Hughes, and Zhang, 2008; Essin, Moore, and Vanderbilt, 2009; Morimoto, Furusaki, and Nagaosa, 2015; Wang, Lian *et al.*, 2015; Pournaghavi *et al.*, 2021). In the field theory description of 3D TIs, a topological θ term $\theta e^2\mathbf{E}\cdot\mathbf{B}/2\pi h$ is added to the ordinary Maxwell electromagnetic Lagrangian (Qi, Hughes, and Zhang, 2008; Sekine and Nomura, 2021), yielding axion electrodynamics (Wilczek, 1987). Here $\mathbf{E}$ and $\mathbf{B}$ are the conventional electric and magnetic fields inside an insulator, and θ is a pseudoscalar. It is normally argued that θ can differ from $-\theta$ only by a multiple of 2π when TR symmetry or inversion symmetry is present in the bulk. It follows that θ is always a multiple of π, an even multiple (normally 0) for a normal 3D insulator, and an odd multiple (normally ± 1) for a 3D TI (Qi, Hughes, and Zhang, 2008; Essin, Moore, and Vanderbilt, 2009). Breaking TR and inversion symmetry in the bulk can generally lead to an arbitrary value of θ. The term *axion* is adopted because the mathematical structure of the electrodynamics of TIs with gapped surface states is similar to that of the hypothetical particles invented by Frank Wilczek to solve the strong charge conjugation-parity problem in particle physics (Peccei and Quinn, 1977). In a field theory description, the parameter θ in the axion effective action continuously varies from the value π in the TI to 0 in the vacuum across the surface region. It turns out that this π change of θ implies the surface half QH effect described in Sec. II.A.2. Therefore, the quantized value $e^2/2h$ of the surface σ_{xy}, as well as the quantized magnetoelectric response of bulk TIs, is equivalent to the quantized θ value of the axion term in electromagnetic Lagrangians of 3D bulk TIs (Sekine and Nomura, 2021).

The definition of the term axion insulators has been somewhat inconsistent in the literature. Generally, an axion insulator is viewed as a 3D TI with a nonzero quantized θ parameter in the bulk and surface states gapped by either surface magnetism or bulk magnetism (Essin, Moore, and Vanderbilt, 2009; Turner *et al.*, 2012; Varnava and Vanderbilt, 2018). In this terminology, axion insulators that allow for the observation of the TME effect have not only insulating bulks but also insulating surfaces and hinges, a requirement that is satisfied by all-in or all-out magnetization configurations (Varnava and Vanderbilt, 2018). A TI heterostructure in which a thick TI film has an undoped interior sandwiched by magnetically doped regions near the film surface [the sample configuration in Fig. 7(c)] with antiparallel magnetization orientations on the two surfaces belongs to this category. When the TI film is thick enough that the surface regions are electrically isolated, this system will support half-quantized surface Hall conductances of opposing signs. The orbital magnetizations associated with the corresponding equilibrium orbital currents then do not cancel perfectly in the presence of a weak electric field applied across the film. The net magnetization per cross-sectional area is

$$M_{\mathrm{orb}} = \frac{e}{2h} \times eEt, \tag{10}$$

where t is the film thickness, the first factor on the right-hand side is the surface state Hall conductance from Eq. (9), and the second factor is the electric potential drop across the film. The electric field creates a parallel bulk magnetization per unit volume with a universal coefficient of proportionality that is quantized in units of $e^2/2h$. This property, known as the TME effect, is equivalent to having $\theta = \pi$ in the electromagnetic Lagrangian and to half-quantized surface Hall conductivities. The TME effect is therefore activated by surface magnetizations whose projections onto the surface normal never change sign. For thin film geometries, the necessary condition is that the top and bottom surface magnetizations have the opposite orientations, so the chiral edge channel is absent in Fig. 7(c).

Experimental confirmation of the TME effect is challenging. The following three conditions are required: (i) the TI film is in the 3D regime so that TSSs at opposing surfaces are decoupled; (ii) all surfaces are gapped, with the chemical potential lying within both gaps; and (iii) the interior of the TI must preserve either TR symmetry or certain crystalline symmetries (such as inversion) to maintain the $\theta = \pi$ constraint. Given that the TME effect is equivalent to a magnetic-surface localized half-quantized Hall conductance, it is reasonable to argue (Morimoto, Furusaki, and Nagaosa, 2015; Wang, Lian *et al.*, 2015; Mogi, Kawamura, Tsukazaki *et al.*, 2017; Mogi, Kawamura, Yoshimi *et al.*, 2017; Xiao *et al.*, 2018) that the previously discussed second scenario of the ZHCP, in concert with observation of the QAH effect, provides experimental evidence of the TME effect. A jump of the total 2D Hall conductance by $\pm e^2/h$ due to reversal of magnetization at one surface must mean that the contribution of that surface to the Hall conductance is $\pm e^2/2h$. Mogi, Kawamura, Yoshimi *et al.* (2017) fabricated asymmetric $(\mathrm{Bi,Sb})_2\mathrm{Te}_3$ sandwich heterostructures with surface Cr doping. The observation of a zero σ_{xy} plateau [Fig. 7(b)] was interpreted as evidence of a TME effect associated with an antiparallel alignment of the top and bottom Cr-doped $(\mathrm{Bi,Sb})_2\mathrm{Te}_3$ magnetized layers. Subsequent magnetic domain imaging measurements on the same sample failed, however, to find evidence of uniform antiparallel magnetization alignment at any external magnetic field (Lachman *et al.*, 2017; Allen *et al.*, 2019), making it less convincing that the observed ZHCP is fully explained by opposing magnetic exchange gaps. Soon thereafter Mogi, Kawamura, Tsukazaki *et al.* (2017) and Xiao *et al.* (2018) replaced the top Cr-doped TI layer with a V-doped layer to form a V-doped TI/TI/Cr-doped TI sandwich heterostructures [Fig. 7(c)]. The significant difference in H_c between the Cr- and V-doped TI systems then leads to a broad ZHCP, as shown in Fig. 7(c). Magnetic force microscopy images in this system reveal two separate magnetization reversals, as expected from the coercive field difference of the two magnetic layers (Xiao *et al.*, 2018). This observation suggests that the observed ZHCP has a different origin than that in the uniformly magnetically doped QAH samples and is the result of an opposite sign half-quantized σ_{xy} in the two surface regions. An alternative approach to probing the TME effect is through magneto-optical measurements (Okada *et al.*, 2016; Wu *et al.*, 2016; Dziom *et al.*, 2017), but they have the disadvantage of probing the response properties

of topological matter at finite frequencies, whereas the TME refers to a characteristic static response.

The essential feature of an axion insulator is the surface half QH effect, but metallic modes may exist on certain surfaces or hinges of a finite sample in a more broad definition once its bulk θ value is quantized. This has led to theoretical proposals of high-order topology in axion insulators (Varnava and Vanderbilt, 2018; Wieder and Bernevig, 2018; Xu *et al.*, 2019; Yue *et al.*, 2019; Zhang, Wu, and Sarma, 2020; R. Chen *et al.*, 2021; Varnava *et al.*, 2021), in which metallic modes exist at the hinges of finite samples. The critical behaviors for the transition from a 3D axion insulator with high-order topology to a trivial insulator have also been theoretically studied (H. Li, Jiang *et al.*, 2021; Song, Lian, Queiroz *et al.*, 2021). Experimentally, the one semicircle behavior of the $(\sigma_{xx}, \sigma_{xy})$ flow diagram observed in thick QAH samples (Grauer *et al.*, 2017; Fijalkowski *et al.*, 2021) is consistent with the scaling behavior of a surface half QH effect (Nomura and Nagaosa, 2011) if one assumes that the phase transitions on the two surfaces occur simultaneously.

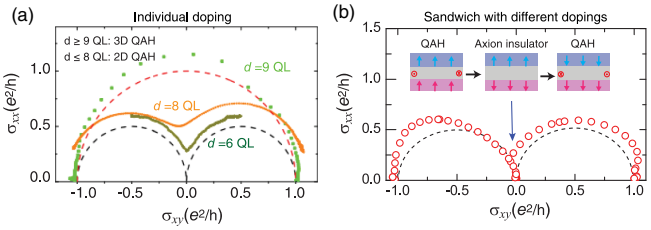

FIG. 8. Scaling behaviors of the QAH effect in uniformly magnetically doped TI films, and in sandwiches with V and Cr surface doping. (a) $(\sigma_{xy}, \sigma_{xx})$ flow diagram of uniformly V-doped $(Bi, Sb)_2Te_3$ with thicknesses of nine QLs (green curve), eight QLs (orange curve), and six QLs (dark yellow curve). (b) $(\sigma_{xy}, \sigma_{xx})$ flow diagram of a sample with an axion insulator doping profile: three QL V-doped $(Bi, Sb)_2Te_3$/five QL $(Bi, Sb)_2Te_3$/three QL Cr-doped $(Bi, Sb)_2Te_3$. Two semicircles of radius $0.5e^2/h$ centered at $(0.5e^2/h, 0)$ and $(-0.5e^2/h, 0)$ are plotted as black dashed lines in (a) and (b) for comparison. A semicircle of the radius e^2/h centered at $(0, 0)$ is shown as a red dashed line in (a). From Grauer *et al.*, 2017, and Xiao *et al.*, 2018.

3. Scaling behavior of plateau transitions

The scaling behavior of plateau transitions in the space of temperature and Landau level filling factor ν has been extensively studied in conventional QH systems (Girvin and Prange, 1990; Huckestein, 1995). In QAH systems, the external magnetic field plays the role of ν, and the plateau behavior is complicated by the role of the magnetic domain structure near the coercive field H_c. Wang, Lian, and Zhang (2014) used a Chalker-Coddington-type network model based on an intuitive picture of random magnetic domain switching and chiral edge state propagation along magnetic domain walls to discuss the scaling properties of transitions between QAH plateaus. Phase diagrams and scaling behaviors have also been addressed by performing numerical simulations of disordered QAH systems (Onoda and Nagaosa, 2003; Nomura and Nagaosa, 2011; Chang, Zhao *et al.*, 2016; Qiao *et al.*, 2016; Chen, Liu, and Xie, 2019). The possible presence of ZHCP states discussed in Sec. III.C.2 strongly influences the scaling behavior of the plateau transitions. In the absence of a ZHCP, the Chern number change on the plateau transition is 2, and this case must be described using a Chalker-Coddington model with two channels (Lee and Chalker, 1994; Xiong *et al.*, 2001; Chen, Liu, and Xie, 2019).

Experimental efforts have explored global phase diagrams and scaling behaviors of QAH effects in a variety of different magnetically doped TI heterostructures (Checkelsky *et al.*, 2014; Kou *et al.*, 2015; Chang, Zhao *et al.*, 2016; Grauer *et al.*, 2017; Kawamura *et al.*, 2018; Liu *et al.*, 2020; Wu, Xiao *et al.*, 2020). Checkelsky *et al.* (2014) found the first evidence of quantum criticality by examining $(\sigma_{xy}, \sigma_{xx})$ as a function of temperature and electrostatic doping near neutrality, concluding that the delocalization behavior of QAH states can be described in terms of the renormalization group flow of the integer QH effect. The global $(\sigma_{xy}, \sigma_{xx})$ phase diagram depends qualitatively on whether or not a ZHCP is present. When a ZHCP is absent the $(\sigma_{xy}, \sigma_{xx})$ flow diagram can be approximated by a semicircle with radius e^2/h centered at $(0, 0)$; when the ZHCP is present it is approximated by two semicircles with radius $0.5e^2/h$ centered at $(0.5e^2/h, 0)$ and $(-0.5e^2/h, 0)$. Two semicircle $(\sigma_{xy}, \sigma_{xx})$ behavior was first observed by Kou *et al.* (2015). Soon thereafter Grauer *et al.* (2017) found a systematic crossover from two semicircle to one semicircle behavior with an increasing thickness of V-doped $(Bi, Sb)_2Te_3$ films and interpreted this behavior as a dimensional crossover from a 2D QAH state to a 3D TI state [Fig. 8(a)]. It was suggested that the critical thickness of this crossover is eight to nine QL for TI films with uniform V doping (Fijalkowski *et al.*, 2021). The thickness dependence strongly relies on the quality of magnetically doped QAH thin films, however, and has additional sensitivity to the typical magnetic domain size and the magnetic dopant chemical environment.

The physical picture of dimensional crossover, which relies on magnetization reversals at both the top and bottom surfaces that occur simultaneously, can be relevant only for uniformly doped systems. It cannot be applied to V-doped TI/TI/Cr-doped TI sandwich structures, since the middle TI layer acts like a magnetic buffer layer that decouples the top and bottom magnetic TI layers. When the number of nonmagnetic interior TI layers is increased, the exchange coupling between the top and bottom magnetic TI layers is quickly reduced and leads to a broader ZHCP (Mogi, Kawamura, Tsukazaki *et al.*, 2017; Xiao *et al.*, 2018). As discussed in Sec. III.C.2, independent surface magnetization reversal processes are observed in V-doped TI/TI/Cr-doped TI heterostructures, but not in uniformly magnetically doped QAH samples. The scaling behavior of the V-doped TI/TI/Cr-doped TI samples always shows two semicircle behavior, as shown in Fig. 8(b), regardless of thickness.

Fijalkowski *et al.* (2021) recently observed an unexpected ZHCP in a symmetric magnetic TI thin film sandwich structure and ascribed the plateau to hybridization between surfaces. They suggested on this basis that the ZHCP observed in intentionally asymmetric V-doped TI/TI/Cr-doped TI sandwich heterostructures (Mogi, Kawamura, Tsukazaki *et al.*, 2017; Xiao *et al.*, 2018) might also originate from a

TABLE I. QAH insulator scaling study summary. QL, quintuple layer; Cr-TI, Cr-doped $(Bi, Sb)_2Te_3$; V-TI, V-doped $(Bi, Sb)_2Te_3$; κ, the critical exponent extracted from the temperature dependence of the plateau transition widths.

QAH-related phase transition	Sample	Extracted κ	T range for scaling (mK)	Reference
Plateau to plateau	Six QL Cr-TI	0.22	20–100	Kou *et al.* (2015)
QAH to Anderson insulator	Four QL V-TI	0.62 ± 0.03	25–500	Chang, Zhao *et al.* (2016)
QAH to trivial insulator	Two QL Cr-TI/two QL TI/two QL Cr-TI/one QL TI	0.61 ± 0.01	60–800	Kawamura *et al.* (2018)
QAH to AH insulator	Five QL Cr-TI	0.31 ± 0.01	100–800	Liu *et al.* (2020)
QAH to axion insulator	Three QL V-TI/five QL TI/three QL Cr-TI	0.38 ± 0.02	45–100	Wu, Xiao *et al.* (2020)

hybridization gap, rather than from the formation of the axion insulator state. This interpretation requires a reduction of the exchange coupling between the local moments and the Dirac electrons, allowing intersurface hybridization to dominate at small external magnetic fields. An alternative explanation for the appearance of two peaks in nominally symmetric samples is that asymmetry was induced unintentionally during the photolithography process. We favor the latter interpretation since Zeeman coupling at the coercive field scale has a small direct influence on electronic structure. Future experiments that more fully reveal trends versus film thickness, on which hybridization depends exponentially, should enable us to distinguish between these scenarios.

The critical exponents κ of the QAH plateau transitions extracted from the temperature dependence of the plateau transition widths are summarized in Table I. κ varies over a broad range of 0.22 to 0.62. This might be because the critical temperature of the QAH state in the magnetically doped TI films or heterostructures is limited to a few kelvin, limiting the temperature range available for identifying the plateau-width power law. Studies on the scaling behaviors of plateau transitions have to be performed at temperatures that are well below the critical temperature of the QH or QAH state (Wei, Tsui, and Pruisken, 1986; Wei *et al.*, 1988; Huckestein, 1995). As a comparison, the critical temperature of the QH state in (In, Ga)As/InP heterostructures is ∼50 K (Wei, Tsui, and Pruisken, 1986), and the scaling behaviors were studied in the temperature range $0.1 < T < 4.2$ K (Wei *et al.*, 1988). In spite of these uncertainties, the determination of the critical exponents still provides valuable information. The plateau transition is expected to be identical to that of QH systems when the magnetization reversals on the two surfaces occur separately. In sandwich samples, Wu, Xiao *et al.* (2020) demonstrated that the QAH to axion insulator phase transition indeed shares scaling universality with the standard plateau transition in the QH effect. However, if the magnetization reversals at the top and bottom surfaces occur simultaneously, the plateau transition should be described by a Chalker-Coddington model with two channels (Lee and Chalker, 1994; Xiong *et al.*, 2001; Chen, Liu, and Xie, 2019). Other features of the magnetization reversal process have also been explored experimentally. Lachman *et al.* (2015) imaged the magnetic structure of a seven QL Cr-doped $(Bi, Sb)_2Te_3/SrTiO_3(111)$ in a QAH state and found a superparamagnetic state with weakly interacting magnetic domains. Liu *et al.* (2016) observed large jumps in the Hall and longitudinal resistances during the magnetic transition between QAH states in a ten QL Cr-doped $(Bi, Sb)_2Te_3/SrTiO_3(111)$ sample and attributed these large jumps to quantum tunneling between magnetic domains. These experiments imply that the magnetic dynamics during the reversal is complex and likely requires a theoretical description that is more sophisticated than simple percolation theory. In addition, Kandala *et al.* (2015) performed angular magnetotransport measurements on a ten QL Cr-doped $(Bi, Sb)_2Te_3/SrTiO_3(111)$ sample by rotating the magnetic field and found that a giant anisotropic magnetoresistance is induced by a magnetic-field-tilt-driven crossover from chiral edge transport to diffusive transport.

4. Current breakdown

The stability of the QAH state against excitation currents has also been studied experimentally in magnetically doped TI systems. Kawamura *et al.* (2017) claimed that some of their observations are similar to those in QH states. For example, they found that the critical current for QAH breakdown is roughly proportional to the width of the Hall bar [Fig. 9(a)]. However, some behavior differs qualitatively from QH state breakdown phenomenology. In particular, there is no sudden increase in dissipation at the breakdown current, which they attributed to a variable-range-hopping bulk transport mechanism at low temperatures. Fox *et al.* (2018) observed a current-induced QAH breakdown at $T \sim 21$ mK and attributed this phenomenon to runaway electron heating in bulk current flow [Fig. 9(b)]. Lippertz *et al.* (2022) recently investigated the QAH breakdown through local and nonlocal measurements and found that the QAH breakdown is absent in

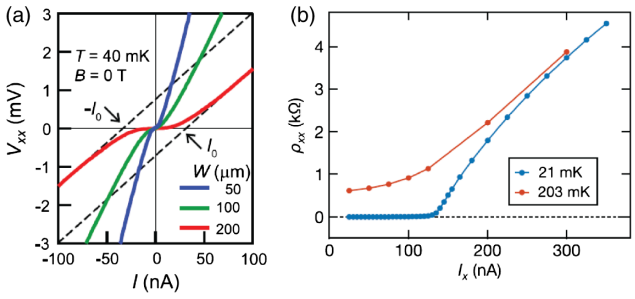

FIG. 9. Current-induced breakdown of the QAH effect. (a) Bias current dependence of the voltage V_{xx} for three Hall bars with different widths $W = 50$ (blue line), 100 (green line), and 200 μm (red line). The QAH samples used here are nine QL Cr-doped $(Bi, Sb)_2Te_3$ films. (b) Bias current I_x dependence of the longitudinal resistance ρ_{xx} of a six QL Cr-doped $(Bi, Sb)_2Te_3$ film. All curves are measured at the charge neutral point $V_g = V_g^0$. From Kawamura *et al.*, 2017, and Fox *et al.*, 2018.

nonlocal regions, indicating that the transverse electric field might be responsible for the QAH breakdown. Because the QAH state in magnetically doped TIs has a strong temperature dependence and a small effective exchange gap (~100 μeV), the QAH breakdown occurs at a significantly smaller current in TI QAH devices (tens to hundreds of nanoamperes) (Kawamura *et al.*, 2017; Fox *et al.*, 2018; Lippertz *et al.*, 2022) than in conventional QH samples (a few tens of microamperes) (Mensz and Tsui, 1989; Kawaji, 1996; Singh and Deshmukh, 2009; Alexander-Webber *et al.*, 2012; Connolly *et al.*, 2012). Further studies that address breakdown in higher temperature QAH insulators are desirable.

D. High-Chern-number QAH effect

High-Chern-number QAH effects have been theoretically proposed for Cr-doped $Bi_2(Se,Te)_3$ films (Wang, Liu, and Liu, 2013) and for films of the topological crystalline insulator SnTe when magnetically doped (Fang, Gilbert, and Bernevig, 2014). The high-Chern-number QAH effect in the former system appears when two or more pairs of inverted subbands are induced by strong exchange fields (Jiang, Qiao *et al.*, 2012; Wang, Liu, and Liu, 2013), while the high-Chern-number QAH effect conjectured in the magnetically doped SnTe system derives from the presence of multiple TSSs (Fang, Gilbert, and Bernevig, 2014). In practice, realization of high-Chern-number QAH states is unlikely in Cr-doped $Bi_2(Se,Te)_3$ films given the complex magnetic configurations suggested by nonsquare Hall conductivity hysteresis loops and the possible relevance of metallic phases (Zhang *et al.*, 2013; Chang *et al.*, 2014). The proposed high-Chern-number QAH state in magnetically doped SnTe is also challenging because of the absence of ferromagnetism, and because the multiple Dirac points are normally located at different energies. This property makes it difficult to have a fully gapped surface in the SnTe system (Fang, Gilbert, and Bernevig, 2014; F. Wang *et al.*, 2018). In addition to these two systems, high-Chern-number QAH states can also be realized in magnetic TI-based multilayer structures with alternating $C = 1$ QAH and normal insulator layers (Burkov and Balents, 2011). The thickness of the normal insulator layer modulates the coupling between two $C = 1$ QAH layers and thus tunes the Chern numbers of QAH insulators.

Jiang *et al.* (2018) initiated a search for high-Chern-number QAH states in Cr-doped $(Bi,Sb)_2Te_3$/CdSe multilayers. However, the CdSe layers had a wurtzite structure. The difference in structure compared to the tetradymite structure of magnetic TIs inevitably leads to stacking faults in Cr-doped $(Bi,Sb)_2Te_3$/CdSe multilayer samples. These defects can induce a large longitudinal resistance and also make the Hall resistances exceed the quantized value. Recently Zhao *et al.* (2020) grew heavily Cr-doped TI/TI multilayers with symmetric structures, specifically [three QL Cr-doped $(Bi,Sb)_2Te_3$/four QL $(Bi,Sb)_2Te_3]_m$/three QL Cr-doped $(Bi,Sb)_2Te_3$ multilayer structures, where m is an integer reflecting the number of bilayer periods. Well-quantized high-Chern-number QAH effects with Chern numbers C of 1–5 were observed [Figs. 10(a)–10(e)]. It is thought that the bulk band gap is no longer inverted in the heavily Cr-doped TI layer because heavy Cr doping greatly reduces SOC. However, the heavy doping can break the TR symmetry of

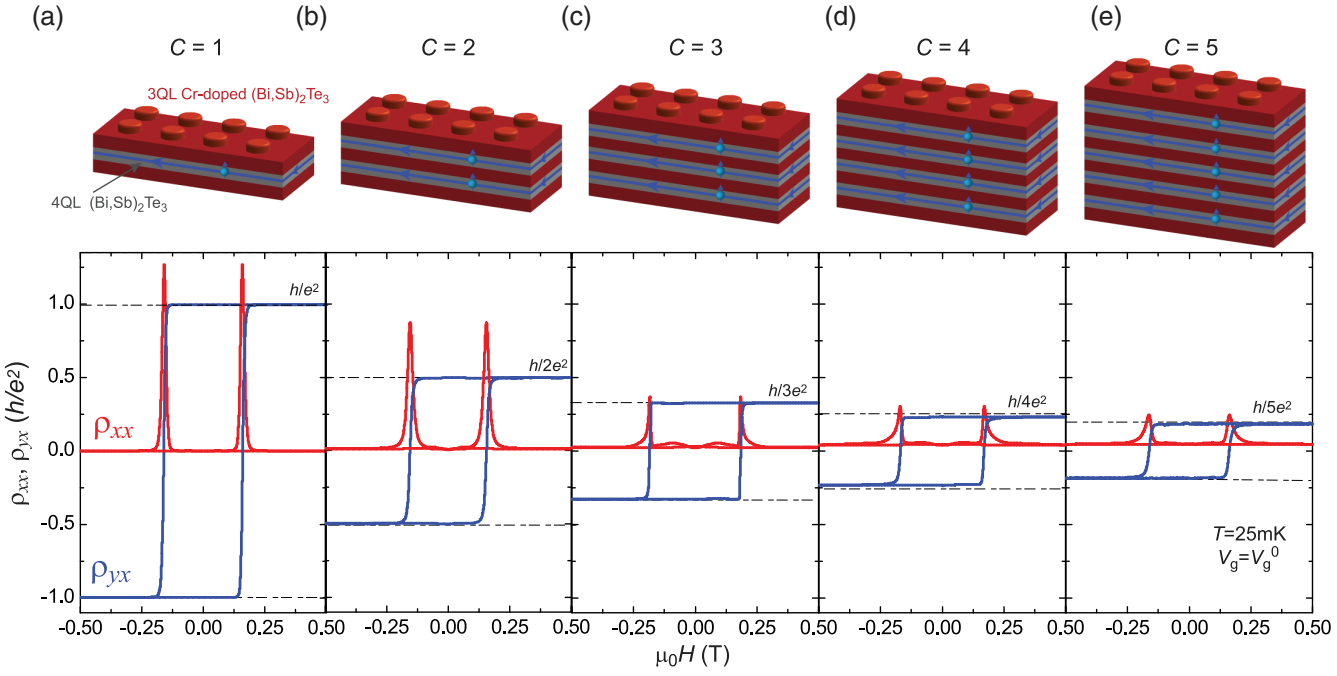

FIG. 10. (a)–(e) High-Chern-number QAH effect in magnetic TI/TI multilayer structures. Top images: schematic (LEGO blocks) multilayer structures for the QAH effect with Chern numbers (C) ranging from 1 to 5. The red and gray LEGOs correspond to three QL Cr-doped $(Bi,Sb)_2Te_3$ and four QL $(Bi,Sb)_2Te_3$, respectively. Bottom panels: magnetic-field $\mu_0 H$ dependence of the longitudinal resistance ρ_{xx} (red curve) and the Hall resistance ρ_{yx} (blue curve) measured at the charge neutral point $V_g = V_g^0$ and $T = 25$ mK. From Zhao *et al.*, 2020.

the undoped TI layers and allows for the $C = 1$ QAH effects in each undoped TI layer. Heavily Cr-doped TI/TI multilayer samples behave like several $C = 1$ QAH insulators in parallel. The Chern number C of the QAH insulators is determined by the number m of undoped TI layers. In the same sample configuration, Zhao *et al.* (2020) also showed that the Chern number of the QAH insulators can be tuned by varying either the magnetic doping concentration or the thickness of the interior magnetic TI layers. Increasing magnetic TI/TI layer numbers is expected to further raise the Chern number, potentially leading to the 3D QAH state with chiral surface states (Halperin, 1987; Bernevig *et al.*, 2007; Wang *et al.*, 2017; Lu, 2019). The realization of QAH insulators with tunable Chern numbers facilitates potential applications of dissipationless chiral edge currents in energy-efficient electronic devices and opens opportunities for developing multichannel quantum computing and higher-capacity chiral circuit interconnects.

IV. $MnBi_2Te_4$: AN INTRINSIC MAGNETIC TI

A. Material properties

$MnBi_2Te_4$ is a tetradymite antiferromagnetic semiconductor and was recently theoretically predicted (Otrokov *et al.*, 2017; J. Li *et al.*, 2019; Zhang, Shi *et al.*, 2019) and experimentally demonstrated (Gong *et al.*, 2019; Otrokov *et al.*, 2019) to be an intrinsic magnetic TI. Like the $(Bi/Sb)_2(Se/Te)_3$ compounds discussed in Sec. III, $MnBi_2Te_4$ crystals have a rhombohedral structure with the space group D_{3d}^5 ($R\bar{3}m$). In the $MnBi_2Te_4$ case the building blocks are seven atom thick (Te-Bi-Te-Mn-Te-Bi-Te) septuple layers (SLs). The lattice structure of $MnBi_2Te_4$ can be viewed as intercalating a Mn-Te bilayer into a Bi_2Te_3 QL [Fig. 11(a)]. As noted in Sec. II.B, $MnBi_2Te_4$ is one member of the $Mn(Bi/Sb)_{2n}(Se/Te)_{3n+1}$ family of compounds, which includes $MnBi_4Te_7$ (H. Li *et al.*, 2019; Shi *et al.*, 2019; Vidal *et al.*, 2019b; J. Wu *et al.*, 2019; Ding *et al.*, 2020; C. Hu *et al.*, 2020b; Klimovskikh *et al.*, 2020; L. Xu *et al.*, 2020; Yan *et al.*, 2020), $MnBi_6Te_{10}$ (H. Li *et al.*, 2019; Shi *et al.*, 2019; Jo *et al.*, 2020; Klimovskikh *et al.*, 2020; Tian *et al.*, 2020; Yan *et al.*, 2020), $MnBi_8Te_{13}$ (C. Hu *et al.*, 2020a), $MnSb_2Te_4$ (Murakami *et al.*, 2019; Yan, Okamoto *et al.*, 2019; Y. Chen *et al.*, 2020; Ge *et al.*, 2021; Y. Liu *et al.*, 2021; Wimmer *et al.*, 2021; Yan, Yang *et al.*, 2021), $MnSb_4Te_7$ (Huan *et al.*, 2021), $Mn(Bi, Sb)_2Te_4$ (B. Chen *et al.*, 2019; Yan, Okamoto *et al.*, 2019; Y. Chen *et al.*, 2020; Jiang *et al.*, 2021; Lee *et al.*, 2021), and $MnBi_2Se_4$ (Zhu *et al.*, 2021). $Mn(Bi/Sb)_{2n}(Se/Te)_{3n+1}$ can be viewed as $(n-1)$ $(Bi/Sb)_2(Se/Te)_3$ QLs stacked on a $Mn(Bi/Sb)_2(Se/Te)_4$ parent to form one unit cell.

As noted in Sec. II.B, the magnetic properties of $MnBi_2Te_4$ stem primarily from the presence of the Mn $3d$ local moments. The Mn^{2+} ions are located at SL centers and carry $5\mu_B$ magnetic moments. They have strong ferromagnetic exchange interactions within each SL and weaker antiferromagnet interactions between adjacent layers [Fig. 11(a)], and therefore have A-type antiferromagnetic order with a Néel temperature $T_N \sim 25$ K [Fig. 11(c)] (Lee *et al.*, 2019; Otrokov *et al.*, 2019; Yan, Zhang *et al.*, 2019; Liu, Wang *et al.*, 2020). As discussed in Sec. II.B. the intralayer ferromagnetism

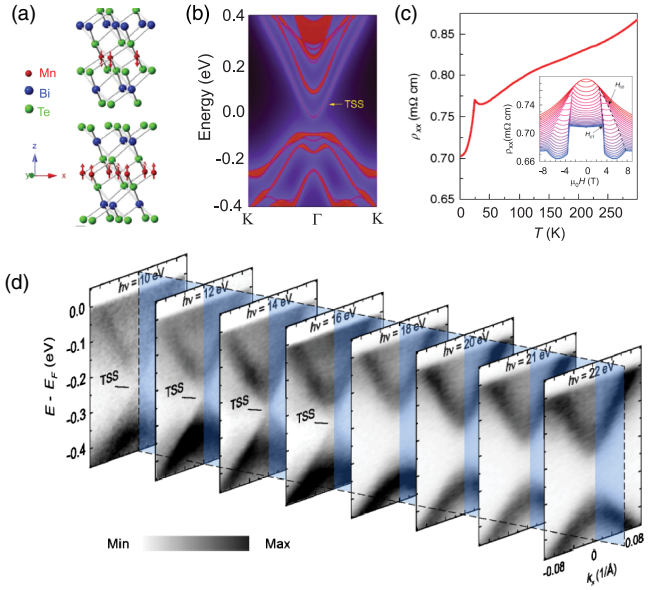

FIG. 11. Properties of $MnBi_2Te_4$ single crystals. (a) Crystal structure of $MnBi_2Te_4$. One SL of $MnBi_2Te_4$ is composed of Te-Bi-Te-Mn-Te-Bi-Te. The red arrows indicate the magnetic moments on the Mn layer. (b) Calculated electronic band structure of $MnBi_2Te_4$. (c) Temperature dependence of the longitudinal resistivity ρ_{xx}. The hump feature occurs at the Néel temperature T_N of $MnBi_2Te_4$ single crystals. Inset: magnetic-field $\mu_0 H$ dependence of ρ_{xx} at different temperatures. (d) ARPES band structures of $MnBi_2Te_4$ single crystals measured at different photon energies. From B. Chen *et al.*, 2019, Y. Chen *et al.*, 2019, Zhang, Shi *et al.*, 2019, and Liu, Wang *et al.*, 2020.

(interlayer antiferromagnetism) is induced by ferromagnetic superexchange (antiferromagnetic super-superexchange), and captured by DFT calculations (Otrokov *et al.*, 2017; J. Li *et al.*, 2019; Zhang, Shi *et al.*, 2019). Magnetic properties in these compounds are strongly influenced by impurity states; for some synthesis conditions, $MnSb_2Te_4$ can exhibit ferromagnetism with T_C of 25–50 K (Murakami *et al.*, 2019; Ge *et al.*, 2021; Y. Liu *et al.*, 2021; Wimmer *et al.*, 2021; Yan, Yang *et al.*, 2021).

$MnBi_{2n}Te_{3n+1}$ compounds have n QLs of Bi_2Te_3 between each $MnBi_2Te_4$ SL. The magnetic coupling between neighboring Mn layers therefore decreases strongly in strength with n and can become ferromagnetic. For $n = 2$ and 3 (i.e., $MnBi_4Te_7$ and $MnBi_6Te_{10}$), the compounds still show the A-type antiferromagnetism, while for $n \geq 4$ the compounds become ferromagnetic (J. Wu *et al.*, 2019; Klimovskikh *et al.*, 2020; Yan *et al.*, 2020). The Néel temperature T_N values of $MnBi_4Te_7$ and $MnBi_6Te_{10}$ are $\sim$13 and $\sim$11 K, respectively (Shi *et al.*, 2019; Tian *et al.*, 2020; Yan *et al.*, 2020), while the Curie temperature T_C of $MnBi_8Te_{13}$ is $\sim$10.5 K (C. Hu *et al.*, 2020a).

The electronic band structures and topological properties of $MnBi_2Te_4$ and its relatives depend qualitatively on magnetic configurations, which can be altered by relatively weak magnetic fields because of the weak interlayer exchange interactions. For example, bulk $MnBi_2Te_4$ is a magnetic TI in its ground antiferromagnetic configuration, with the topological nontrivial surface states formed by Bi and Te p-orbital

bands that are inverted and have strong SOC [Fig. 11(b)] (J. Li *et al.*, 2019; Otrokov *et al.*, 2019; Zhang, Shi *et al.*, 2019). In the aligned spin configuration induced by relatively modest magnetic fields, it becomes a type-II Weyl semimetal with a single pair of Weyl points (J. Li *et al.*, 2019; Zhang, Shi *et al.*, 2019; Lei, Chen, and MacDonald, 2020).

Although the electronic bands of these compounds are theoretically expected to be relatively simple, early experimental studies have painted a more confusing picture. In early angle-resolved photoemission spectroscopy (ARPES) measurements, the TSSs of $MnBi_2Te_4$ bulk crystals were found to have surface gaps greater than 50 meV (Lee *et al.*, 2019; Otrokov *et al.*, 2019; Vidal *et al.*, 2019a). However, the observed gap had a weak temperature dependence and could be detected even above T_N, suggesting that it was not related to magnetic order in $MnBi_2Te_4$. Soon thereafter several groups performed high-resolution synchrotron or laser ARPES measurements with a photon energy $h\nu \leq 16$ eV and observed gapless TSSs that cannot be resolved for $h\nu > 16$ eV [Fig. 11(d)] (B. Chen *et al.*, 2019; Y. Chen *et al.*, 2019; Hao *et al.*, 2019; H. Li *et al.*, 2019; Nevola *et al.*, 2020; Swatek *et al.*, 2020; Yan, Fernandez-Mulligan *et al.*, 2021). This finding suggests that the gap observed in prior studies (Lee *et al.*, 2019; Otrokov *et al.*, 2019; Vidal *et al.*, 2019a) could be a bulk gap. The fact that the gapless TSSs are observed only for $h\nu \leq 16$ eV might be a result of matrix element and cross-section effects in ARPES measurements (Y. Chen *et al.*, 2019). The observation of the gapless TSSs is also independent of magnetic ordering in $MnBi_2Te_4$. The formation of the gapless TSSs in $MnBi_2Te_4$ bulk crystals has been attributed to the existence of multiple antiferromagnetic domains (Y. Chen *et al.*, 2019), to unexpected types of magnetic order such as in-plane *A*-type antiferromagentism or *G*-type antiferromagnetism (Hao *et al.*, 2019; Swatek *et al.*, 2020), and to weak hybridization between the localized magnetic moments and the surfaces of $MnBi_2Te_4$ (H. Li *et al.*, 2019). Further study is needed to clarify the origin of the gapless TSSs observed in some ARPES studies of $MnBi_2Te_4$ bulk crystals.

For $MnBi_{2n}Te_{3n+1}$ with $n \geq 2$, the ARPES results are also controversial. Y. Hu *et al.* (2020) and L. Xu *et al.* (2020) observed gapless TSSs for all terminations of $MnBi_4Te_7$ and $MnBi_6Te_{10}$, whereas Jo *et al.* (2020) observed a temperature-dependent gap opening on $MnBi_2Te_4$ with SL termination, but gapless surface states with Bi_2Te_3 QL terminations. Separately, Gordon *et al.* (2019), C. Hu *et al.* (2020a, 2020b), Ma *et al.* (2020), Wu *et al.* (2020), and Yan, Zhu *et al.* (2021) observed gapped TSSs in $MnBi_6Te_{10}$ and $MnBi_8Te_{13}$ with one QL Bi_2Te_3/one SL $MnBi_2Te_4$ termination, which might be interpreted in terms of surface-bulk band hybridization, but gapless TSSs for other terminations. The topological character of $MnSb_2Te_4$ is still under debate (B. Chen *et al.*, 2019; Wimmer *et al.*, 2021). More recently $MnSb_4Te_7$ was demonstrated to be an intrinsic antiferromagnetic TI with $T_N \sim 13.5$ K and to possess multiple topological phases, including antiferromagnetic TI phases, ferromagnetic inversion-symmetry-protected axion insulator phases, and ferromagnetic Weyl semimetal phases with multiple Weyl nodes, depending on magnetic configurations and doping levels (Huan *et al.*, 2021).

In addition to direct magnetic and ARPES measurements, transport, STM, and magnetic force microscopy measurements have also been performed on $MnBi_2Te_4$ bulk crystals. Negative magnetoresistance below and above T_N, the emergence of a canted antiferromagnetic state between the antiferromagnetic and spin-aligned states, and nonlinear Hall traces in the canted antiferromagnetic state have all been reported in transport studies (B. Chen *et al.*, 2019; Cui *et al.*, 2019; Lee *et al.*, 2019; Li *et al.*, 2020). Low-temperature STM measurements have found large densities (3%–5%) of Mn/Bi antisites, which might affect intralayer and interlayer magnetic coupling of $MnBi_2Te_4$ (Yan, Zhang *et al.*, 2019; Huang *et al.*, 2020; Liang *et al.*, 2020; Yuan *et al.*, 2020). Recently antiferromagnetic domains as well as the *A*-type antiferromagnetic order were imaged in $MnBi_2Te_4$ and $Mn(Bi,Sb)_2Te_4$ bulk crystals by magnetic force microscopy (Sass, Ge *et al.*, 2020; Sass, Kim *et al.*, 2020). More focused reviews of the $MnBi_2Te_4$ family of compounds were authored by Ning and Mao (2020), Sekine and Nomura (2021), Wang *et al.* (2021), and Zhao and Liu (2021).

B. $MnBi_2Te_4$ thin films

A-type antiferromagnetic order has a substantial influence on the topological properties of $MnBi_2Te_4$ thin films. Because of the ferromagnetism within each SL, the surface states develop a magnetic exchange gap driven by surface magnetism. The signs of the half-quantized Hall conductance σ_{xy} contributed by the top and bottom surfaces are determined by the direction of magnetic order at that surface. For perfect *A*-type order, the surface states on top and bottom SLs will yield parallel surface layer magnetizations when the number N of septuple layers is odd, and to antiparallel magnetizations when N is even. The total Hall conductance is therefore expected to be quantized in the absence of a magnetic field at $\pm e^2/h$ when N is odd and the films are thick enough to weaken hybridization between the top and bottom surfaces. Even N films have no Hall conductance for insulating states. Like the ZHCP states of magnetically doped sandwich structures discussed previously, even N $MnBi_2Te_4$ thick films are referred to as axion insulators in the literature (J. Li *et al.*, 2019; Otrokov, Rusinov *et al.*, 2019; Zhang, Shi *et al.*, 2019; Liu, Wang *et al.*, 2020), a practice that we follow. Films with an odd number of SLs will yield QAH states. It has been predicted that an in-plane magnetic field can drive $MnBi_2Te_4$ into a higher-order Möbius insulator with surface "Möbius fermions" and chiral hinge states (Zhang, Wu, and Sarma, 2020).

Atomically thin $MnBi_2Te_4$ films can be formed either by MBE growth (Gong *et al.*, 2019; Rienks *et al.*, 2019; Kagerer *et al.*, 2020; Lapano *et al.*, 2020; Zhu *et al.*, 2020; Tai *et al.*, 2021; Trang *et al.*, 2021; Zhao *et al.*, 2021; Bac *et al.*, 2022) or by manual exfoliation from bulk crystals (Deng *et al.*, 2020; Ge *et al.*, 2020; Liu, Wang *et al.*, 2020; Gao *et al.*, 2021; C. Liu *et al.*, 2021; Ovchinnikov *et al.*, 2021; Ying *et al.*, 2022). MBE growth of $MnBi_2Te_4$ thin films has been achieved by alternate depositions of Bi_2Te_3 and MnTe layers (Gong *et al.*, 2019; Trang *et al.*, 2021; Zhao *et al.*, 2021; Bac *et al.*, 2022), coevaporation of Mn, Bi, and Te elements (Rienks *et al.*, 2019; Lapano *et al.*, 2020; Zhu *et al.*, 2020; Tai *et al.*, 2021),

and codeposition of MnTe and Bi_2Te_3 sources (Kagerer *et al.*, 2020). Owing to unusual growth dynamics, Bi_2Te_3, MnTe, and Mn-doped Bi_2Te_3 inevitably coexist with the dominant $MnBi_2Te_4$ phase in all these MBE-grown materials. MBE growth of $MnBi_2Te_4$ follows a SL-by-SL growth mode, which is similar to the QL-by-QL growth mode of the well-studied Bi_2Te_3 family TI (Y.-Y. Li *et al.*, 2010; Zhang *et al.*, 2010). For this reason, it is difficult to achieve uniform thickness $MnBi_2Te_4$ thin films over millimeter-size ranges. Owing to this property, the Hall resistances measured in MBE-grown $MnBi_2Te_4$ thin films (Gong *et al.*, 2019; Lapano *et al.*, 2020; Tai *et al.*, 2021; Zhao *et al.*, 2021; Bac *et al.*, 2022) are normally small. Realization of the QAH effect requires uniform thickness across entire devices, which is challenging for MBE-grown samples.

Mechanically exfoliated $MnBi_2Te_4$ thin flakes are typically small and can be formed into uniform micrometer-scale devices. Moreover, exfoliated flakes can be flexibly combined with other 2D materials to fabricate gated devices in which unintentional doping can be compensated. Indeed, both QAH and axion insulator states have been claimed to be realized in the absence of a magnetic field (Deng *et al.*, 2020; Liu, Wang *et al.*, 2020). Magnetic fields influence electronic structure directly, but most strongly via their impact on magnetic configurations. Both antiferromagnetic and spin-aligned Chern insulator states have been realized under high magnetic fields in exfoliated $MnBi_2Te_4$ flakes [Figs. 12(b), 12(c), and 13] (Deng *et al.*, 2020; Ge *et al.*, 2020; Liu, Wang *et al.*, 2020; Gao *et al.*, 2021; C. Liu *et al.*, 2021; Ovchinnikov *et al.*, 2021; Ying *et al.*, 2022) and will be discussed in Sec. IV.C.

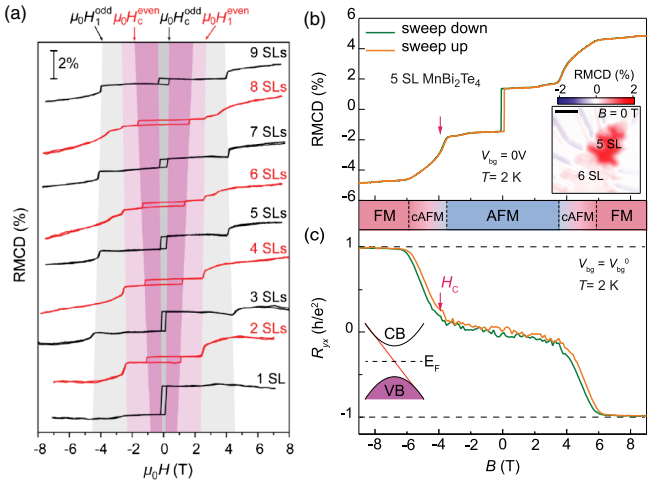

FIG. 12. Relationship between RMCD and Hall data. (a) RMCD measurements on $MnBi_2Te_4$ flakes (from one to nine SLs) at $T = 1.6$ K. The shaded areas highlight the thickness dependence of the low-field spin-flip and spin-flop phase transitions in odd- and even-number SL samples. (b),(c) Magnetic-field $\mu_0 H$ dependence of the RMCD signal and the Hall resistance R_{yx} of a five SL $MnBi_2Te_4$ device. The RMCD and transport characteristics in (b) and (c) are measured in the same sample at $V_g = 0$ and at the charge neutral point $V_g = V_g^0$, respectively. From Ovchinnikov *et al.*, 2021, and Yang *et al.*, 2021.

We now discuss the SL-number N dependence of the magnetic properties of exfoliated $MnBi_2Te_4$ flakes. Since even- and odd-SL $MnBi_2Te_4$ films, respectively, have compensated and uncompensated magnetic moments, their total magnetizations should exhibit distinct magnetic-field dependences. Recently two independent studies reported an even-odd effect in the magnetism of thin $MnBi_2Te_4$ flakes using reflection magnetic circular dichroism (RMCD) measurements [Fig. 12(a)] (Ovchinnikov *et al.*, 2021; Yang *et al.*, 2021). Specifically, (i) odd-SL flakes have pronounced hysteresis loops and significant remanent RMCD signals at weak magnetic fields that reflect uncompensated magnetic moments. On the other hand, even SL samples have vanishingly small RMCD signals and hysteresis loops, which is consistent with their zero net magnetization. (ii) The critical magnetic field for the spin-flop transition between antiferromagnetic and canted antiferromagnetic states [labeled H_1 in Fig. 12(a)], which occurs at intermediate field strengths, is ~2.6 T for even-SL and ~4.2 T for odd-SL $MnBi_2Te_4$ samples. The larger H_1 for odd-SL $MnBi_2Te_4$ samples compared to even ones can be understood in terms of the Zeeman energy of coupling to uncompensated magnetization in odd-SL samples (Ovchinnikov *et al.*, 2021; Yang *et al.*, 2021). This behavior was also observed in transport measurements on both exfoliated and MBE-grown $MnBi_2Te_4$ films (B. Chen *et al.*, 2019; Zhao *et al.*, 2021).

C. Chern insulators, axion insulators, and the QAH effect

Deng *et al.* (2020) realized the $C = 1$ QAH effect in a five SL exfoliated $MnBi_2Te_4$ device soon after it was predicted theoretically. Figure 13(a) shows the magnetic-field $\mu_0 H$ dependence of the Hall resistance R_{yx} and the longitudinal resistance R_{xx}. At $T = 1.4$ K, $R_{yx} \sim 0.97 h/e^2$ and $R_{xx} \sim 0.061 h/e^2$ at zero magnetic field. The Hall

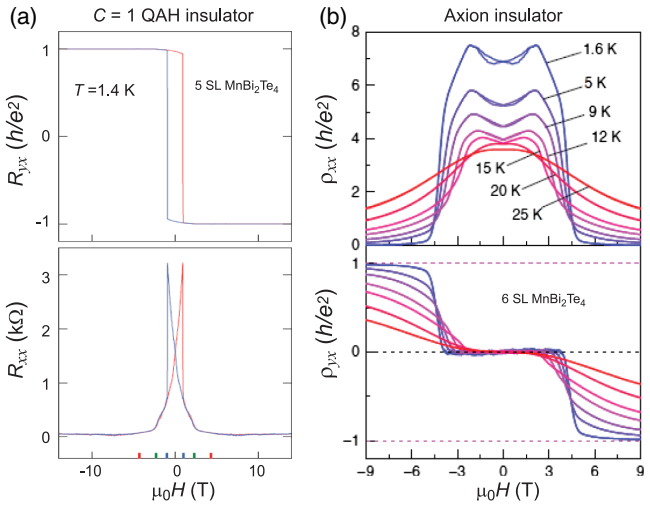

FIG. 13. Realization of the $C = 1$ QAH insulator and a zero Hall plateau in exfoliated $MnBi_2Te_4$ flakes. (a) $C = 1$ QAH insulator observed in five SL $MnBi_2Te_4$. (b) Zero Hall plateau, taken as evidence for an axion insulator state, observed in six SL $MnBi_2Te_4$. From Deng *et al.*, 2020, and Liu, Wang *et al.*, 2020.

quantization accuracy can be improved by applying an intermediate strength external magnetic field to stabilize aligned spin magnetic configurations in which $R_{yx} \sim 0.998h/e^2$ at $\mu_0 H \sim 2.5$ T. To date the $C = 1$ QAH effect at zero magnetic field in exfoliated $MnBi_2Te_4$ devices has been realized only by this group. However, the $C = 1$ Chern insulator state in spin-aligned $MnBi_2Te_4$ under magnetic fields has been realized repeatedly by several different groups in devices with both even and odd numbers of SLs (Deng *et al.*, 2020; Ge *et al.*, 2020; Liu, Wang *et al.*, 2020; Gao *et al.*, 2021; C. Liu *et al.*, 2021; Ovchinnikov *et al.*, 2021; Ying *et al.*, 2022). The $C = 1$ Chern insulator state with $R_{yx} \geq 0.904h/e^2$ in exfoliated $MnBi_2Te_4$ devices is found to survive even up to ~45 K under high magnetic fields (higher than $T_N \sim 25$ K) (Ge *et al.*, 2020).

Liu, Wang *et al.* (2020) measured axion insulator characteristics in an exfoliated $MnBi_2Te_4$ device with a nominal six SL thickness and the ground antiferromagnetic spin configuration. Figure 13(b) shows the $\mu_0 H$ dependence of ρ_{xx} and ρ_{yx} at $V_g = V_g^0$. At the base temperature $T = 1.6$ K, ρ_{yx} is found to be zero over the magnetic-field range $-3.5 < \mu_0 H < 3.5$ T, which is concomitant with a large ρ_{xx} of $\sim 7h/e^2$. Liu, Wang *et al.* (2020) considered the large ρ_{xx} combined with vanishing ρ_{yx} as the key. However, Ovchinnikov *et al.* (2021) performed combined electrical transport and RMCD measurements and found that the RMCD and AH hysteresis loops are not synchronized in their devices, whether even or odd SL. For a five SL $MnBi_2Te_4$ device, they found that both ρ_{yx} and its hysteresis loop nearly vanish over the magnetic-field range $-3.8 < \mu_0 H < 3.8$ T, in sharp contrast to RMCD characteristics that showed pronounced hysteresis [Figs. 12(b) and 12(c)]. The nearly vanishing R_{yx} and the large R_{xx}, which reaches $\sim 7h/e^2$ in this nominal five SL $MnBi_2Te_4$ device, are both similar to the behavior of the nominally six SL $MnBi_2Te_4$ device shown in Fig. 13(b) (Liu, Wang *et al.*, 2020). Since the large ρ_{xx} combined with vanishing ρ_{yx} are also signatures of a trivial 2D insulator, Ovchinnikov *et al.* (2021) speculated that the antiferromagnetic state of five SL $MnBi_2Te_4$ devices might be a trivial magnetic insulator. Indeed, the only practical distinction between axion insulators and ordinary insulators in zero-magnetic-field transport measurements is the tendency of the former to have small sidewall energy gaps that likely limit the resistivity of high-quality devices in which bulk transport is negligible.

In addition to axion insulator and $C = 1$ Chern insulator states, $C = 2$ Chern insulator states have also been observed in the magnetic-field-induced spin-aligned states of exfoliated $MnBi_2Te_4$ devices with nine and ten SL thicknesses [Figs. 14(a) and 14(b)]. Ge *et al.* (2020) attributed the observation of the $C = 2$ Chern insulator in thick $MnBi_2Te_4$ devices to an interplay between quantum confinement effects and the Weyl semimetal physics of $MnBi_2Te_4$ in spin-aligned high-magnetic-field configurations (J. Li *et al.*, 2019; Zhang, Shi *et al.*, 2019). In the limit of thick films, the ratio of the Chern number C to the septuple layer number N is expected to approach the Hall conductivity per layer of the bulk semimetal in quantum e^2/h units (Lei, Chen, and MacDonald, 2020). Cai *et al.* (2022) recently fabricated the

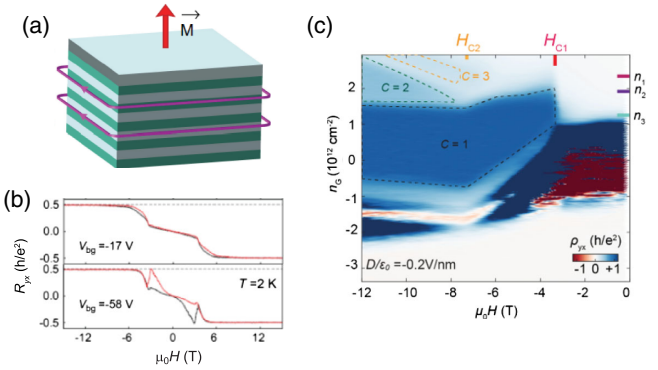

FIG. 14. $C = 2$ Chern insulator state in $MnBi_2Te_4$ devices. (a) Schematics for the $C = 2$ Chern insulator state with two chiral edge states propagating along the edges of the sample. (b) Magnetic-field $\mu_0 H$ dependence of the Hall resistance R_{yx} of a ten SL $MnBi_2Te_4$ device at fixed bottom gate voltages $V_{bg} = -17$ and -58 V. (c) ρ_{yx} as a function of the magnetic field $\mu_0 H$ and the gate injected carrier density n_G at a fixed electric field $D/\varepsilon_0 = -0.2$ V/nm in a seven SL $MnBi_2Te_4$ device. Black, green, and yellow dashed lines enclose $C = 1, 2, 3$, respectively. The marked densities are $(n_1, n_2, n_3) = (2.23, 1.87, 1.29) \times 10^{12}$ cm^{-2}. From Ge *et al.*, 2020, and Cai *et al.*, 2022.

$MnBi_2Te_4$ devices with dual gates and mapped the ρ_{yx} of a seven SL $MnBi_2Te_4$ device as a function of both $\mu_0 H$ and the injected carrier density n_G at a fixed displacement field $D/\varepsilon_0 = -0.2$ V/nm. In addition to the usual $C = 1$ plateaus in both canted antiferromagnetic and ferromagnetic regimes, $C = 2$ and 3 states, signaled by $\rho_{yx} \sim h/Ce^2$, appear in spin-aligned states at higher carrier densities n_G. Unlike the $C = 1$ phase, the $C = 2$ and 3 phases are stabilized by strong magnetic fields and are centered on densities that are proportional to the field $\mu_0 H$ [Fig. 14(c)], which suggests that they are related to the formation of Landau levels (Deng *et al.*, 2020; Ge *et al.*, 2020; H. Li, Chen *et al.*, 2021; Cai *et al.*, 2022).

More recently Gao *et al.* (2021) observed that an AH effect is induced in an even-SL-number ($N = 6$) $MnBi_2Te_4$ device by a gate electric field. This effect, in which the Hall current responses are layer dependent and can cancel each other out in two opposite layers due to the combined symmetry of inversion and TR, is referred to as the layer Hall effect. Applying a gate voltage breaks inversion and thus leads to the emergence of a large, layer-polarized AH effect. Reversing gate voltages can change the sign of AH resistance. Gao *et al.* (2021) interpreted their results in terms of electric-field-induced polarization and layer-locked Berry curvatures. We note that the interpretations of transport observations like these can be reinforced by RMCD data, as previously discussed (Ovchinnikov *et al.*, 2021; Yang *et al.*, 2021). The studied $MnBi_2Te_4$ device has a quantized AH effect in the field-induced spin-aligned state when the chemical potential is tuned to the charge neutral point. The layer Hall effect, on the other hand, is observed when the Fermi level lies outside the gap and is not quantized. A gate-induced sign reversal of the AH effect near zero magnetic field was systematically studied in exfoliated $MnBi_2Te_4$ devices by Zhang *et al.*

(2020). In odd-SL-number N $MnBi_2Te_4$ thin films, the QAH effect is expected to break down after gate electric fields exceed a breakdown field ∼10 meV/nm (Lei and MacDonald, 2021).

V. MOIRÉ MATERIALS

The large lattice constants of the moiré material systems introduced in Sec. II.A.3 are important because they allow the number of electrons per period to be varied by up to around ten purely with electrical gates, effectively moving through the periodic table of these artificial materials without doping. In many cases (Andrei *et al.*, 2021), moiré materials can be tuned into regimes in which correlations are strong and broken symmetries are common. The broken symmetry states that have been realized include superconductors (Cao, Fatemi *et al.*, 2018; Lu *et al.*, 2019; Yankowitz *et al.*, 2019; Balents *et al.*, 2020), Mott insulators (Cao *et al.*, 2018), Wigner crystals (Y. Xu *et al.*, 2020; H. Li *et al.*, 2021) and (of particular interest in this Colloquium) unusual orbital ferromagnets with Chern insulator ground states (Sharpe *et al.*, 2019; G. Chen *et al.*, 2020; Y. Chen *et al.*, 2020; Polshyn *et al.*, 2020; Serlin *et al.*, 2020; T. Li *et al.*, 2021b; Sharpe *et al.*, 2021; Tschirhart *et al.*, 2021). In the following, we explain the QAH effects seen in graphene and TMD moiré materials, which are alike in that they rely on spontaneous valley polarization, but distinct in that their nontrivial topologies are related to sublattice and layer degrees of freedom, respectively.

A. Strong correlations in twisted bilayer graphene

Because of its superlattice periodicity, TBG [Fig. 15(a)], the first moiré material, has low-energy emergent Bloch bands (Dos Santos, Peres, and Neto, 2007; G. Li *et al.*, 2010) in a BZ defined by the moiré superlattice. Bistritzer and MacDonald (2011) predicted that when the rotation angle was adjusted to a magic angle ∼1.1°, electronic velocities would slow markedly,

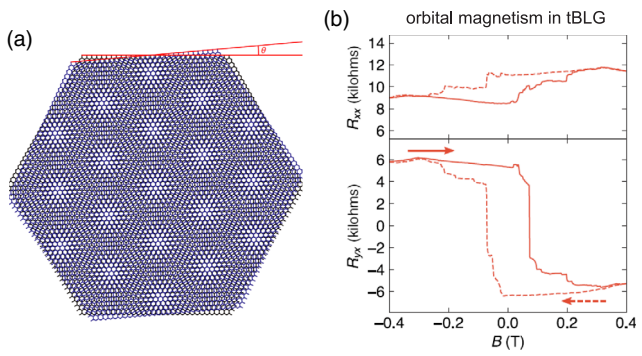

FIG. 15. Orbital magnetism in twisted bilayer graphene systems. (a) Schematic of twisted bilayer graphene. The relative orientation angle θ determines the periodicity of the moiré superllattice. (b) Magnetic-field $\mu_0 H$ dependence of the longitudinal resistance R_{xx} and the Hall resistance R_{yx} with $n/n_s = 3/4$ and $D/D_0 = -0.62$ V/nm at $T = 30$ mK demonstrating the hysteretic AH effect resulting from the emergent orbital magnetic order. From Sharpe *et al.*, 2019.

converting bilayer graphene from a 2D Fermi liquid with moderate interaction strengths to a strongly correlated electron system. Progress in accurate twist angle control (Kim, DaSilva *et al.*, 2017; Cao *et al.*, 2018; Cao, Fatemi *et al.*, 2018; Ribeiro-Palau *et al.*, 2018) eventually enabled this prediction to be tested. In 2018 Cao *et al.* (2018) and Cao, Fatemi *et al.* (2018) discovered that magic-angle TBG has a rich phase diagram as a function of twist angle and moiré band filling factor ν with correlated insulators common at integer values of ν, and superconducting domes common over intervals of noninteger ν. This discovery was confirmed and the rich properties of magic-angle TBG and related multilayer systems were more fully revealed by subsequent experiments (Lu *et al.*, 2019; Yankowitz *et al.*, 2019). Some of this ongoing work was reviewed by Andrei and MacDonald (2020) and Liu and Dai (2021a). The following discussion focuses on the unusual ferromagnetic Chern insulator states that are responsible for the QAH effect.

B. Orbital TR symmetry breaking

In TBG, spin and valley degrees of freedom combine to provide four flavors for the superlattice Bloch states. The Hamiltonian is spin independent, and the two valleys (located at opposite corners of the atomic-scale BZ) are exchanged by TR. It follows that every moiré Bloch state is fourfold degenerate. Because there are two flat bands centered on neutrality for each flavor, the flat bands are partially occupied for moiré band filling factors $\nu \in (-4, 4)$. The broken symmetry states that are common in magic-angle TBG have conventional particle-hole density matrix order parameters in the spin-valley flavor space, and in most cases do not break translational symmetry. They can therefore be viewed as generalized ferromagnets. As previously discussed, the AH effects that have been observed in moiré materials result from order that is characterized by a finite valley polarization and not, as in conventional ferromagnets and magnetic TIs, from SOC combined with spontaneous spin polarization. Magic-angle TBG is quite exceptional in that SOC does not play an essential role in its AH effect. Finite valley polarization also leads to finite values of orbital magnetization, as well as Faraday and Kerr responses. The QAH effect in magic-angle TBG is most common when the moiré band filling factor is an odd integer, but this condition is neither sufficient nor necessary, as we now explain.

C. QAH effect at odd moiré band filling factors

Sharpe *et al.* (2019) aligned a TBG moiré superlattice with a h-BN cladding layer and found evidence of emergent ferromagnetism with a giant AH effect at $\nu = 3$ [Fig. 15(b)]. Over a narrow range of carrier density n near $\nu = 3$, the magnetic-field dependence of the longitudinal resistance R_{xx} and the Hall resistance R_{yx} show hysteretic behavior suggestive of collective behavior. At zero magnetic field, a large $R_{yx} \approx \pm 6$ kΩ remains after magnetic-field cycling, with the sign depending on the direction of the magnetic-field sweep. This observation is evidence of orbital ferromagnetic order in TBG. Nonlocal transport measurements suggest that the TBG system might be a Chern insulator. Sharpe *et al.* also found

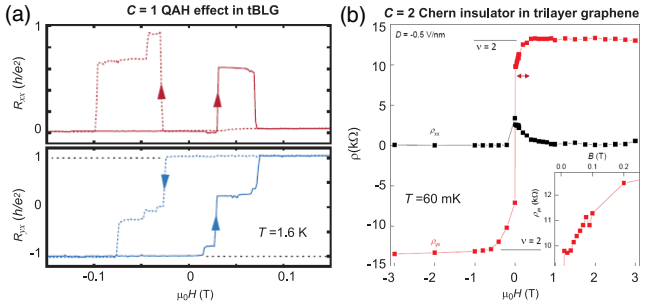

FIG. 16. $C = 1$ QAH effect in TBG and $C = 2$ Chern insulator state in trilayer graphene. (a) Magnetic-field $\mu_0 H$ dependence of the longitudinal resistance R_{xx} and the Hall resistance R_{yx} in TBG measured at $n = 2.37 \times 10^{12}$ cm^{-2}. (b) Magnetic-field $\mu_0 H$ dependence of the longitudinal resistance ρ_{xx} and the Hall resistance ρ_{yx} in a rhombohedral trilayer graphene-*h*-BN moiré superlattice. A $C = 2$ Chern insulator state is realized under a finite external magnetic field. From G. Chen *et al.*, 2020, and Serlin *et al.*, 2020.

that the Hall effect of the TBG sample could be reversed by applying a small external current. More recently AH effects were also realized in twisted monolayer-bilayer graphene (Polshyn *et al.*, 2020; S. Chen *et al.*, 2021), in *ABC* trilayer graphene on *h*-BN, and in TBG on WSe_2 (J.-X. Lin *et al.*, 2022).

Soon after the discovery of the AH effect, which signals spin-valley order that breaks TR symmetry, Serlin *et al.* (2020) optimized the device fabrication process and realized the $C = 1$ QAH effect in TBG [Fig. 16(a)]. At zero magnetic field and $T = 1.6$ K, the Hall resistance R_{yx} approaches h/e^2 in a narrow range of density near moiré band filling $\nu = 3$ and a deep minimum develops in the longitudinal resistance R_{xx}. The Curie temperature for flavor ordering is $T_C \sim 7.5$ K. Accurate R_{yx} quantization can survive up to $T \sim 3$ K. To date this experiment has not been reproduced by other groups, presumably due to the difficulties in the fabrication of high-quality TBG/*h*-BN devices. There is experimental evidence that some insulating states at odd values of ν are Chern insulators and some are not (Lu *et al.*, 2019).

Several theoretical papers (Po *et al.*, 2018; Kang and Vafek, 2019; Seo, Kotov, and Uchoa, 2019; Bultinck, Chatterjee, and Zaletel, 2020; Xie and MacDonald, 2020) raised the possibility of a QAH effect in magic-angle TBG due to spin-valley ferromagnetism, some prior to the experimental observation. These papers are compatible with the observation that although the QAH effect is sometimes observed at odd integer filling factors, it often is not observed. First, the flavor splitting produced by scattering off the order must be larger than the width of the single-particle flat bands in order to eliminate the Fermi surfaces present for $\nu \in (-4, 4)$ in the normal state. The ratio of the flavor splitting of the bands to the bandwidth depends (Xie and MacDonald, 2020) strongly on twist angle, and on the proximity of electrodes used for gating, which tend to screen electron-electron interactions (X. Liu *et al.*, 2021). Second, the Chern numbers of the occupied bands must have a nonzero sum. Bultinck, Chatterjee, and Zaletel (2020) emphasized that a nonzero Chern number in an individual valley can originate from the coupling between the graphene device and the encapsulating *h*-BN dielectric, which breaks the C_2T symmetry that protects the 2D Dirac points (Ahn and Yang, 2017). C_2T symmetry can also break spontaneously.

In general, we expect the flat band Chern numbers to be ± 1 whenever the C_2T symmetry is violated. The expectation is justified provided that there are no band closings between the large twist angle limit (MacDonald, Jung, and Zhang, 2012), where layers are weakly coupled and the smaller twist angles at which the bands become flat. In the large twist angle limit, the isolated layer half-quantized Hall conductivities add to yield Chern number 1. Level crossings do sometimes occur (Xie and MacDonald, 2020), depending on the details of the band and interaction model, and this may explain the occasional observation of odd filling-factor insulating states that appear not to have a QAH effect. QAH states with higher Chern numbers have been studied in a number of twisted multilayer systems (J. Liu *et al.*, 2019; Zhang, Mao *et al.*, 2019), whose properties are sensitive to gate-applied vertical displacement fields.

Liu, Liu, and Dai (2019) suggested a pseudo-magnetic-field picture to understand the nonzero Chern number in each valley and the resulting QAH effect in TBG. Given the similarity between the flat bands in TBG and Landau levels, fractional Chern insulator phases have also been discussed theoretically (Ledwith *et al.*, 2020; Repellin and Senthil, 2020). He, Goldhaber-Gordon, and Law (2020) proposed a giant orbital magnetoelectric effect in TBG, which can explain the extremely small current that can switch the magnetization in TBG (Sharpe *et al.*, 2019). The band basis with nonzero Chern number in each valley, sometimes called the "Chern band basis," is also valuable for understanding other topological band properties, such as fragile topology (Ahn, Park, and Yang, 2019; Po *et al.*, 2019; Song *et al.*, 2019; Song, Lian, Regnault, and Bernevig, 2021), and other correlated phases in twisted bilayer graphene (Bernevig *et al.*, 2021; Lian *et al.*, 2021; Liu and Dai, 2021b).

The QAH effect also occurs in graphene multilayer moiré superlattices when the moiré bands are flat, sometimes with systematics that differ from those of the bilayer case. G. Chen *et al.* (2020) observed hysterisis and a $C = 2$ Chern insulator state at band filling $\nu = 1$ in an *ABC* trilayer graphene/*h*-BN moiré superlattice [Fig. 16(b)]. At $T = 60$ mK, the Hall resistance ρ_{yx} is quantized to 13.0 ± 0.2 kΩ for magnetic fields larger than ~0.4 T, demonstrating the $C = 2$ Chern insulator state. The Hall resistance drops to $\rho_{yx} \sim 8$ kΩ, which is much smaller than the quantized value at $\mu_0 H \sim 0$ T, suggesting that the Chern insulator state is stabilized by a magnetic field. Furthermore, when the carrier density n and the displacement field D are varied, ρ_{xx} does not show a dip at the same point that ρ_{yx} has a peak. This observation might be related to domain walls separating states with different Chern numbers; more studies are needed to clarify its physical origin. In addition to the QAH states observed at zero magnetic field, TBG Chern insulator phases at the finite magnetic field have been found and studied by many (Nuckolls *et al.*, 2020; Saito *et al.*, 2021; Wu *et al.*, 2021). We notice that the Streda formula (Streda, 1982), which relates the Chern number to the

derivative of 2D electron density at which the charge gap occurs with respect to the applied magnetic field, provides a useful approach to demonstrate the appearance of Chern insulator phases. See Nuckolls *et al.* (2020) and Choi *et al.* (2021), who used scanning tunneling microscopy to identify the gap densities, or Pierce *et al.* (2021) and Xie *et al.* (2021), who used local compressibility measurements. The Streda formula approach has been less useful in magnetically doped TIs because, we believe, disorder closes or substantially reduces the thermodynamic gaps. In many cases, Chern insulators appear at unexpectedly weak magnetic fields, suggesting the presence competing many-body ground states with different Chern numbers (Zhang and Zhang, 2012).

We emphasize that TBG does not possess any local magnetic moments. The magnetization of TBG is therefore always dominated by its orbital contribution, which varies with chemical potential across the bulk band gap because of the role of topologically protected chiral edge states (Zhu, Su, and MacDonald, 2020). The relationship of Eq. (9), which applies inside the gaps and is equivalent to Hall conductivity quantization (MacDonald, 1994), implies that a jump of orbital magnetization $\Delta M_{\rm orb} = CeE_g/h$ occurs when the Fermi energy is tuned across the energy gap E_g of the QAH state. In magnetically doped TIs, this jump is almost negligible compared to the spin magnetization of the local moments, which does not vary when the chemical potential is in the gap. The jump of orbital magnetization induced by tuning the Fermi energy can allow for magnetic order to be reversed electrically in a weak magnetic field, as demonstrated experimentally by Polshyn *et al.* (2020).

D. QAH effect in *AB*-stacked $MoTe_2/WSe_2$ heterobilayers

The QAH effect was also recently realized in *AB*-stacked $MoTe_2/WSe_2$ moiré heterobilayers. The two semiconducting TMD layers form a triangular moiré superlattice with three high-symmetry staking sites: metal on metal (*MM*), metal on chalcogen (*MX*), and chalcogen on chalcogen (*XX*) (M = Mo, W; X = Te, Se), as shown in Fig. 17(a). Since the lattice mismatch between $MoTe_2$ and WSe_2 is ∼7%, the period of the moiré lattice is relatively short ∼5 nm and the moiré density is $\sim 5 \times 10^{12}$ cm^{-2} (T. Li *et al.*, 2021a). Application of an out-of-plane electric field can control the bandwidth and change the band topology by intertwining moiré bands associated with different layers or with different orbital character within a layer [Fig. 17(a)]. At moiré band filling $\nu = 1$, a state with Hall resistance R_{yx} quantized at $\sim h/e^2$ and vanishing longitudinal resistance R_{xx} has been observed [Fig. 17(b)]. The Hall resistance ρ_{yx} of the QAH effect in magnetically doped TI films [Figs. 4–6] and exfoliated $MnBi_2Te_4$ flakes [Fig. 13] is always less than h/e^2 when the longitudinal resistance ρ_{xx} is finite. However, for the QAH effect observed in TBG [Fig. 16(a)] and in *AB*-stacked TMD bilayers [Fig. 17(b)], ρ_{yx} is greater than h/e^2 when ρ_{xx} is greater than zero. This difference might be related to the different types of disorder in the two classes of QAH systems.

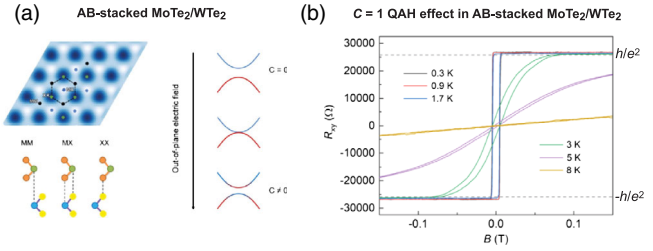

FIG. 17. $C = 1$ QAH effect in an *AB*-stacked $MoTe_2/WSe_2$ heterobilayer. (a) Left image: triangular moiré superlattice with the high-symmetry stacking sites *MM*, *MX*, and *XX* (M = Mo, W; X = Se, Te). Right image: schematic of out-of-plane electric-field-induced band inversion in an *AB*-stacked $MoTe_2/WSe_2$ heterobilayer. (b) Magnetic-field $\mu_0 H$ dependence of the Hall resistance R_{yx} in an *AB*-stacked $MoTe_2/WSe_2$ heterobilayer with the filling factor $\nu = 1$ at different temperatures. A $C = 1$ QAH insulator state is realized. From T. Li *et al.*, 2021b.

TMD bilayer moiré superlattices have valley degrees of freedom in each layer that are locked to spin by strong SOC. One theoretical scenario (Zhang, Devakul, and Fu, 2021; Pan *et al.*, 2022) for a QAH effect echoes that thought to apply to TBG, namely, a combination of valley-projected Chern bands with opposite Chern numbers in the two valleys combined with TR symmetry breaking by spontaneous valley polarization. Berry curvatures of opposite sign in opposite valleys respect TR invariance and are present in the electronic bands of 2D TMD crystals (Xiao *et al.*, 2012), even without moiré modulation. If this is the operable mechanism, there is still a need to understand how precisely the valley-projected bands develop finite Chern numbers, and the answer to this question is not as obvious as in previous cases, because of the absence of simple isolated Dirac cones that can readily be gapped. It is clear experimentally that the QAH effect occurs when the perpendicular electric field applied between layers is strong enough to bring the valence band tops in the WSe_2 and $MoTe_2$ layers close to alignment so that they can have avoided crossings that yield large Berry curvatures. In the case of *AB*-stacked bilayers, however, the relationship between spin and valley is opposite in the two layers. For this reason, single-particle hybridization between layers is expected to be weak, making it less obvious how valley-projected Chern bands could develop. Zhang, Devakul, and Fu (2021), Pan *et al.* (2022), Xie, Zhang, and Law (2022), and Xie *et al.* (2022) separately provided plausible scenarios that rely on specific details of the bilayer moiré band electronic structure for how Chern bands could emerge. Recent studies of the magneto-optical properties of these states suggest that they have intervalley order (Tao *et al.*, 2022), apparently invalidating valley polarization mechanisms and favoring those that invoke time-reversal broken intervalley coherent states (Devakul and Fu, 2022; Xie, Zhang, and Law, 2022). The general lesson from all these studies is that topologically nontrivial bands are even more common in moiré materials than in atomic-scale crystals, where bands have a strong tendency to organize according to the atomic shells of constituent atoms.

VI. QAH EFFECT RESEARCH CHALLENGES

A. Theoretical proposals and challenges

In this Colloquium, we have focused our attention on quasi-2D electron systems in which the QAH effect has already been observed. We now examine some theoretical ideas that have been proposed over the years, but not yet realized in experiment. The following list of possibilities is far from exhaustive, especially since new QAH mechanisms that are currently completely unanticipated are likely to emerge in the coming years.

1. QAH materials

As discussed in Sec. II, the QAH effect requires both band inversion and spontaneous TR symmetry breaking. A natural design strategy for the QAH effect is therefore to catalyze magnetism in materials that are already topological. The magnetism promotion strategies that are considered most often are (i) magnetic doping and (ii) the fabrication of ferromagnetic (or antiferromagnetic) insulator/topological material heterostructures. A typical example of the magnetic doping approach is to design the AH effect in magnetically doped II-VI or III-V semiconductor compound heterostructures. Ideally the host semiconductor should already have a topologically nontrivial band structure, as in the case of HgTe quantum wells (Liu, Qi *et al.*, 2008; Budewitz *et al.*, 2017). More flexibility can be achieved by integrating two different material compounds to form type-II quantum wells in which the conduction band bottom in one material has lower energy than the valence band top in the other material. Following this approach, a QAH state has been predicted to occur in magnetically doped InAs/GaSb quantum wells (Liu, Hughes *et al.*, 2008; Wang *et al.*, 2014) and in other similar *p-n* heterojunctions between II-VI, III-V, and group IV semiconductors (Zhang *et al.*, 2014). Because magnetic doping does not always lead to magnetic order, however, this approach has not yet been successful.

One possibility to overcome this obstacle is to combine two 2D ferromagnetic materials to form a type-II junction (Garrity and Vanderbilt, 2014; Pan *et al.*, 2020). An alternative theoretical possibility follows from the observation that when the hybridization between layers in *p-n* heterojunctions is weak compared to interaction strengths, rich phase diagrams can emerge (Budich, Trauzettel, and Michetti, 2014; Pikulin and Hyart, 2014; Xue and MacDonald, 2018; Zhu *et al.*, 2019; Zeng, Xue, and MacDonald, 2022) in which TR symmetry breaking and QAH states appear spontaneously without the complication of magnetic doping.

Motivated by the Haldane model (Haldane, 1988) and the Kane-Mele model (Kane and Mele, 2005), a body of theoretical work focused on compounds with honeycomb-type lattice structures and strong SOC. Graphene possesses a typical honeycomb lattice, but weak SOC and no local magnetic moments. It was therefore proposed that QAH states could be induced by adding heavy transition elements to graphene as adatoms (Qiao *et al.*, 2010, 2012; Tse *et al.*, 2011; Zhang *et al.*, 2012; Li, West *et al.*, 2015; Deng *et al.*, 2017; de Lima, Ferreira, and Miwa, 2018; Zhang, Li *et al.*, 2019) or by forming ferromagnetic insulator-graphene heterostructures (Zhang *et al.*, 2015; Zhang, Ning *et al.*, 2019; Högl *et al.*, 2020; Vila, Garcia, and Roche, 2021). These strategies have not succeeded to date, presumably because the spatial distribution of adatoms is inevitably disordered and the hybridization between graphene and adjacent materials tends to be weak. Heavier elements that can also form honeycomb or buckled honeycomb lattice structure, such as silicene (Ezawa, 2012, 2013; Zhang, Liu, and Liu, 2013; Zhang, Zhao, and Yang, 2013; Kaloni, Singh, and Schwingenschlögl, 2014; Pan *et al.*, 2014; Qian *et al.*, 2019), germanene (Wu, Shan, and Yan, 2014; Hsu *et al.*, 2017; Zhang, Qin *et al.*, 2019; Pham and Ganesh, 2020; Zou *et al.*, 2020), stanene (Xu *et al.*, 2013; Wu, Shan, and Yan, 2014; Zhang, Zhang *et al.*, 2016; Zhang, Zhou *et al.*, 2016; Li, 2019), and bismuth systems (Jin and Jhi, 2015; Liu, Zhou, and Yao, 2015; Niu *et al.*, 2015; Ji *et al.*, 2016), have also been considered as possible QAH effect hosts. In addition to these 2D materials containing a single element, honeycomb lattices are common in more complex materials, including organic triphenyl-transition-metal compounds (Wang, Liu, and Liu, 2013), half-fluorinated GaBi (Chen *et al.*, 2016), codecorated in-triangle adlayers on a $\mathrm{Si}(111)$ surface (Zhou, Sun, and Jena, 2017), heavy atom layers on magnetic insulator substrates (Garrity and Vanderbilt, 2013), monolayer jacutingaite (Luo *et al.*, 2021), monolayer $PtCl_3$ (You *et al.*, 2019), monolayer EuO_2 (Meng *et al.*, 2021), and (111) perovskite-type transition-metal oxides (Xiao *et al.*, 2011).

The approach of inducing magnetism externally has the disadvantage that magnetic doping introduces disorder and thus degrades sample quality, while the ferromagnetic (or antiferromagnetic) insulator/topological material heterostructure approach has the disadvantage that it relies on magnetic proximity effects that are often weak. Thus, it is desirable to find topological materials with intrinsic magnetism, but they are rare (Huang *et al.*, 2017; Wu, 2017). One approach is to search for magnetic Weyl semimetals since the 3D magnetic Weyl semimetal phase is closely related to the 2D QAH state. In thin films, Weyl nodes are gapped by finite-size effects allowing the QAH effect to occur. In the limit of thick films, finite-thickness gaps become smaller and the total Chern number per layer of the film approaches (Lei, Chen, and MacDonald, 2020) the nonquantized Hall conductivity per layer of the bulk material. Thus, one may expect the QAH effect in 2D films of magnetic Weyl semimetals with broken TR symmetry. Following this idea, a number of intrinsic magnetic materials have been proposed, including $HgCr_2Se_4$ (Xu *et al.*, 2011), $Co_3Sn_2S_2$ (D. Liu *et al.*, 2019; Morali *et al.*, 2019), Mn_2Sn (Kuroda *et al.*, 2017), and Co_2MnGa (Belopolski *et al.*, 2019). The QAH state is expected to emerge in all these systems in the quasi-2D thin film limit (Xu *et al.*, 2011; Muechler *et al.*, 2020).

An additional path for achieving the QAH effect is to create systems in which interaction effects are likely to spontaneously break TR and induce nonzero Chern number bands (Martin and Batista, 2008; Min *et al.*, 2008; Raghu *et al.*, 2008; Nandkishore and Levitov, 2010; Zhang *et al.*, 2011). The QAH states seen in 2D moiré superlattices provide one successful example of this route to QAH states (Wu *et al.*, 2018; Wu and Sarma, 2020; Kwan *et al.*, 2021; Liu and Dai, 2021b; Shi, Zhu, and MacDonald, 2021). Other 2D quantum spin Hall systems with small Dirac velocities have also been

proposed as possible QAH hosts that do not require magnetic dopants (Min *et al.*, 2008; Cao *et al.*, 2016; Xue and MacDonald, 2018).

2. Fractional QAH effect

In 2D electron gases with partial Landau level filling under strong magnetic fields, strong correlations can result in gapped many-body states that have quasiparticles with fractional charge and fractional statistics. This phenomenon is known as the fractional QH effect (Stormer, Tsui, and Gossard, 1999). It is natural to ask whether or not a fractional version of the QAH effect, the fractional QAH effect, can occur in strongly interacting systems (Neupert *et al.*, 2011; Sun *et al.*, 2011; Tang, Mei, and Wen, 2011; Klinovaja, Tserkovnyak, and Loss, 2015). The search for materials in which the fractional QAH effect occurs is challenged by the lack of simple predictive theoretical tools that account for strong correlations in realistic materials. Even for the weakly correlated materials in which DFT calculations are helpful, theory is not always able to account for all important complications. At present, the flat bands induced by moiré superlattices provide the most promising direction toward the realization of fractional QAH states (Ledwith *et al.*, 2020; Repellin and Senthil, 2020).

3. Higher temperature QAH effect

The successful theoretical prediction and subsequent experimental realization of the QAH effect has been recognized as a great triumph of our understanding of topological states of matter, and as a demonstration of our ability to engineer complex topological materials. To utilize these states in technology, however, the low critical temperature at which the QAH effect is observed is a substantial obstacle. The QAH effects in magnetically doped TIs (Chang *et al.*, 2013a; Chang, Zhao, Kim, Zhang *et al.*, 2015; Mogi *et al.*, 2015), in the intrinsic magnetic TI $MnBi_2Te_4$ (Deng *et al.*, 2020), and in moiré materials (Serlin *et al.*, 2020; T. Li *et al.*, 2021b) have comparable and low onset temperatures.

An important goal of QAH research is to greatly enhance the temperature at which the QAH effect is observed. One of the following two approaches might ultimately prove successful: (i) form high-quality heterostructures between TIs and high Curie temperature ferromagnetic (or high Néel temperature antiferromagnetic) insulators (Tang *et al.*, 2017; Wang *et al.*, 2019) or (ii) discover new moiré bilayers that are ordered with shorter moiré periods (Andrei and MacDonald, 2020). The former requires that TI and oxide film growth be successfully combined. The latter approach requires a joint effort involving both theoretical predictions and material synthesis. The quest to realize higher temperature QAH states not only promotes new fundamental inquiries but also could carry far-reaching implications for topological quantum computation and low-energy-cost spintronic devices.

B. Potential applications

1. Chiral Majorana edge modes

In recent decades, the search for Majorana modes has been a key activity in condensed matter physics (Das *et al.*, 2012; Deng *et al.*, 2012; Mourik *et al.*, 2012; Rokhinson, Liu, and Furdyna, 2012; Nadj-Perge *et al.*, 2014; Jeon *et al.*, 2017; D. Wang *et al.*, 2018; Kayyalha *et al.*, 2020). Majorana modes exhibit nonlocal quantum exchange statistics and are promising as a platform for topological quantum computation (Nayak *et al.*, 2008; Alicea, 2012; Beenakker, 2013). Majorana modes can appear at the boundary or inside the vortex cores of topological superconductors (TSCs).

Qi, Hughes, and Zhang (2010) predicted that chiral TSCs can be realized in QAH-superconductor hybrid structure like that illustrated in Fig. 18(a). A chiral TSC has a full pairing gap in the bulk and an odd number $\mathcal{N}$ of chiral Majorana edge modes (MEMs). Proximity-induced superconductivity in a QAH insulator can give rise to chiral MEMs appearing at the topological phase transition between trivial and nontrivial phases. In general, a QAH insulator with C chiral edge modes coupled to an s-wave superconductor is a chiral TSC with $\mathcal{N} = 2C$ chiral MEMs. Here C is the Chern number of the isolated QAH insulator and $\mathcal{N}$ labels the superconductor Chern number. When proximitized, the transition from a topologically nontrivial phase of a $C = 1$ QAH phase to a $C = 0$ topologically trivial (i.e., normal insulator) phase has to go through a chiral TSC phase with $\mathcal{N} = 1$. Based on the quasiparticle properties of this state, Wang, Zhou *et al.* (2015) predicted that a half-quantized two-terminal conductance σ_{12} plateau would appear near the coercive field H_c of a QAH-superconductor hybrid structure and be a fingerprint of a

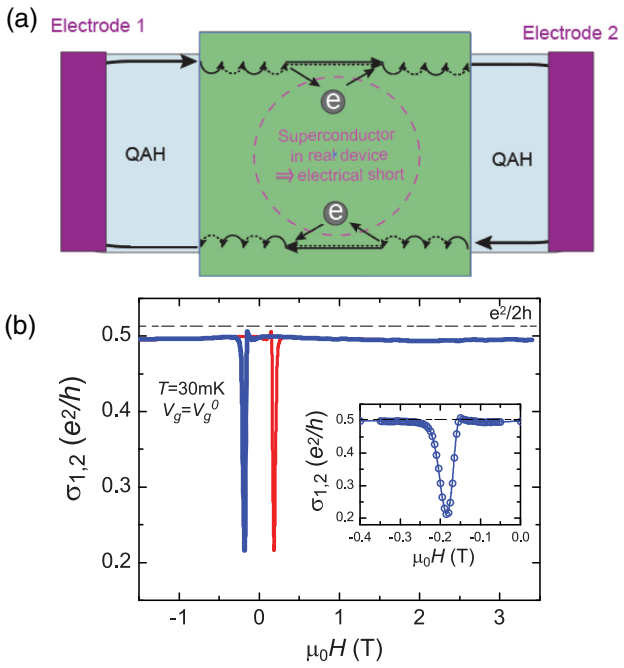

FIG. 18. Absence of the chiral Majorana edge modes in millimeter-size QAH-superconductor devices. (a) A millimeter-size superconductor strip covering a QAH device induces an electrical short that circumvents a chiral MEM signal. (b) Magnetic-field $\mu_0 H$ dependence of the two-terminal conductance $\sigma_{1,2}$ of a QAH-superconductor device. $\sigma_{1,2} \sim 0.5e^2/h$ for the entire $\mu_0 H$ range when the magnetization is accurately aligned. No change in $\sigma_{1,2}$ is observed when the Nb strip transitions from the superconducting state to the normal state. From Kayyalha *et al.*, 2020.

$\mathcal{N} = 1$ chiral TSC. As we explain, however, several theoretical papers later raised concerns about this conclusion (Chen *et al.*, 2017, 2018; Huang, Setiawan, and Sau, 2018; Ji and Wen, 2018; Lian *et al.*, 2018). Separately it was theoretically proposed that 1D nanowires formed from QAH insulators in proximity to superconductivity can host Majorana zero modes at the ends of the wire (Chen *et al.*, 2018; Zeng *et al.*, 2018; Xie *et al.*, 2020).

Experimental studies of QAH-superconductor heterostructure have been controversial. The predicted half-quantized σ_{12} plateau was reported in a millimeter-size QAH-Nb hybrid structure in 2017 (He *et al.*, 2017). However, Kayyalha *et al.* (2020) recently carried out a systematic Andreev reflection spectroscopy study of the contact transparency between the QAH insulator and superconducting Nb layers on more than 30 QAH-Nb devices. They found that σ_{12} is half quantized in QAH-Nb devices even when the magnetization is well aligned and the coercive field is exceeded [Fig. 18(b)]. The theoretical calculations given by Wang, Zhou *et al.* (2015) accounted only for quasiparticle transport processes in the hybrid system and did not account for collective currents carried by the superconducting condensate. When these are allowed, the superconductor can act as an electrical short for the QAH device [Fig. 18(a)], making transport an ineffective probe of quasiparticle properties. For this reason, the observation of the half-quantized plateau cannot be considered as conclusive evidence for the existence of chiral MEMs in the millimeter-size QAH-superconductor hybrid structures (Kayyalha *et al.*, 2020).

2. Resistance standards

As explained in Sec. I, the QAH effect can be used to create a resistance standard that is free from the need for superconducting magnets. To make this goal a reality, it is necessary to improve the accuracy of the Hall resistance quantization in the QAH effect and understand sources of deviation from perfect quantization. To date all high-precision measurements on the QAH effect have been performed on magnetically doped TI films and heterostructures. In both Cr- and V-doped QAH samples, the quantization of the Hall resistance has already been demonstrated at the level of parts-per-million (ppm) uncertainty. Fox *et al.* (2018) used a cryogenic current comparator system to perform the electrical transport on a six QL uniformly Cr-doped $(Bi, Sb)_2Te_3$ film and measured quantization of the Hall resistance to within 1 ppm at zero magnetic field. Götz *et al.* (2018) measured a nine QL V-doped $(Bi, Sb)_2Te_3$ film and determined a value of 0.17 ± 0.25 ppm. Okazaki *et al.* (2020) performed high-precision transport measurements on a nine QL modulation-doped QAH sandwich sample and demonstrated 2 ppm accuracy. More recently Okazaki *et al.* (2022) measured the same QAH sandwich device with a permanent magnet and claimed precision of 10 parts per billion (ppb). Note that the uncertainties of the order of 0.1 ppm–10 ppb still do not reach the requirements for a quantum resistance standard, which requires quantization with uncertainty on the order of 1 ppb (Jeckelmann and Jeanneret, 2001; Poirier and Schopfer, 2009). Therefore, further optimization of QAH samples, whether magnetically doped TI (Sec. III), $MnBi_2Te_4$ (Sec. IV), or moiré superlattice (Sec. V) systems, will be needed if the QAH effect is to achieve a breakthrough in resistance metrology.

3. Dissipation-free interconnects

The dissipationless chiral edge current of the QAH state can potentially be integrated into contemporary electronic or spintronic technology to develop chiral electronic or chiral spintronic devices. Since chiral edge transport eliminates local electrical resistivity, leaving only terminal or contact resistances, it was theoretically proposed that QAH devices can be used to construct chiral interconnects in computing devices in which the total resistance is independent of the circuit length (Zhang and Zhang, 2012). The spin polarization (Zhang, Hsu, and Liu, 2016; Cheraghchi and Sabze, 2020) and real-space spin textures (Wu, Liu, and Liu, 2014) carried by magnetically doped TI chiral edge states might also enable electrical control of magnetic domain-wall motion (Upadhyaya and Tserkovnyak, 2016; Kim, Kurebayashi, and Nomura, 2019). The interplay between chiral edge states and magnetic domain walls has been experimentally demonstrated (Rosen *et al.*, 2017; Yasuda *et al.*, 2017). Electrical switching of magnetic order has been demonstrated in TBG moiré superlattice devices (Sharpe *et al.*, 2019; Polshyn *et al.*, 2020; Serlin *et al.*, 2020; Zhu, Su, and MacDonald, 2020; S. Chen *et al.*, 2021; Tschirhart *et al.*, 2022). In magnetic TI systems with the well-quantized QAH effect, electrical switching of the edge state chirality was recently realized through spin-orbit torque (Yuan *et al.*, 2022). The realization of all-electrical switching of the QAH edge current chirality can be important for the development of chiral electronic devices. Chiral edge state–based electronic devices could potentially usher in a new era of dissipation-free memory and logic devices and could have a transformative impact on the grand challenges facing semiconductor electronics.

ACKNOWLEDGMENTS

C.-Z. C., C.-X. L., and A. H. M. thank R. Bistritzer, C. Canali, M. H. W. Chan, Y.-T. Cui, X. Dai, Z. Fang, K. He, T. Hughes, J. Jain, M. Kayyalha, C. Lei, B. Lian, X. Lin, L. Lu, P. Mahon, L. Molenkamp, J. Moodera, N. Morales-Duran, Q. Niu, A. Pertsova, P. Potasz, N. Pournaghavi, X.-L. Qi, N. Samarth, C. G. Smith, Y.-Y. Wang, F. Wu, W.-D. Wu, D. Xiao, X. D. Xu, Q.-K. Xue, B.-H. Yan, J. Q. Yan, Q.-M. Yan, F. Zhang, H.-J. Zhang, and S.-C. Zhang for long-term collaborations and interactions related to the subject of this Colloquium. C.-Z. C. acknowledges support from U.S. Department of Energy (DOE) Grants No. DE-SC0019064 and No. DE-SC0023113, Army Research Office (ARO) Grants No. W911NF1810198 and No. W911NF2210159, NSF CAREER Award No. DMR-1847811, Penn State NSF-MRSEC Grant No. DMR-2011839, AFOSR Grant No. FA9550-21-1-0177, Gordon and Betty Moore Foundation's EPiQS Initiative (Grant No. GBMF9063), and the Alfred P. Sloan Foundation. C.-X. L. acknowledges support from ONR Grant No. N00014-18-1-2793, DOE Grant No. DE-SC0019064, Penn State NSF-MRSEC Grant No. DMR-2011839, Princeton NSF-MRSEC Grant

No. DMR-2011750, and Kaufman Grant No. KA2018-98553. A. H. M. acknowledges support from the U.S. Department of Energy, Office of Science, Basic Energy Sciences, under Awards No. DE-SC0022106 and No. DE-SC0019481, from the Simons Foundation, and from the Army Research Office under Grant No. W911NF-16-1-0472.

REFERENCES

Ahn, J., S. Park, and B.-J. Yang, 2019, Phys. Rev. X **9**, 021013.
Ahn, J., and B.-J. Yang, 2017, Phys. Rev. Lett. **118**, 156401.
Alexander-Webber, J., A. Baker, P. D. Buckle, T. Ashley, and R. Nicholas, 2012, Phys. Rev. B **86**, 045404.
Alicea, J., 2012, Rep. Prog. Phys. **75**, 076501.
Allen, M., Y. Cui, E. Y. Ma, M. Mogi, M. Kawamura, I. C. Fulga, D. Goldhaber-Gordon, Y. Tokura, and Z.-X. Shen, 2019, Proc. Natl. Acad. Sci. U.S.A. **116**, 14511.
Anderson, P. W., 1950, Phys. Rev. **79**, 350.
Andrei, E. Y., D. K. Efetov, P. Jarillo-Herrero, A. H. MacDonald, K. F. Mak, T. Senthil, E. Tutuc, A. Yazdani, and A. F. Young, 2021, Nat. Rev. Mater. **6**, 201.
Andrei, E. Y., and A. H. MacDonald, 2020, Nat. Mater. **19**, 1265.
Aryasetiawan, F., and K. Karlsson, 2019, J. Phys. Chem. Solids **128**, 87.
Auerbach, A., 2012, *Interacting Electrons and Quantum Magnetism* (Springer Science+Business Media, New York).
Bac, S.-K., *et al.*, 2022, npj Quantum Mater. **7**, 46.
Balents, L., C. R. Dean, D. K. Efetov, and A. F. Young, 2020, Nat. Phys. **16**, 725.
Beenakker, C., 2013, Annu. Rev. Condens. Matter Phys. **4**, 113.
Belopolski, I., *et al.*, 2019, Science **365**, 1278.
Bernevig, B. A., T. L. Hughes, S. Raghu, and D. P. Arovas, 2007, Phys. Rev. Lett. **99**, 146804.
Bernevig, B. A., T. L. Hughes, and S.-C. Zhang, 2006, Science **314**, 1757.
Bernevig, B. A., B. Lian, A. Cowsik, F. Xie, N. Regnault, and Z.-D. Song, 2021, Phys. Rev. B **103**, 205415.
Bernevig, B. A., and S.-C. Zhang, 2006, Phys. Rev. Lett. **96**, 106802.
Bestwick, A., E. Fox, X. Kou, L. Pan, K. L. Wang, and D. Goldhaber-Gordon, 2015, Phys. Rev. Lett. **114**, 187201.
Bianco, R., and R. Resta, 2013, Phys. Rev. Lett. **110**, 087202.
Bistritzer, R., and A. H. MacDonald, 2011, Proc. Natl. Acad. Sci. U.S.A. **108**, 12233.
Bloembergen, N., and T. Rowland, 1955, Phys. Rev. **97**, 1679.
Budewitz, A., K. Bendias, P. Leubner, T. Khouri, S. Shamim, S. Wiedmann, H. Buhmann, and L. Molenkamp, 2017, arXiv:1706.05789.
Budich, J. C., B. Trauzettel, and P. Michetti, 2014, Phys. Rev. Lett. **112**, 146405.
Bultinck, N., S. Chatterjee, and M. P. Zaletel, 2020, Phys. Rev. Lett. **124**, 166601.
Burkov, A., and L. Balents, 2011, Phys. Rev. Lett. **107**, 127205.
Bychkov, Y. A., and E. I. Rashba, 1984, JETP Lett. **39**, 78, http://jetpletters.ru/ps/1264/article_19121.pdf.
Cai, J., *et al.*, 2022, Nat. Commun. **13**, 1668.
Cao, W., R.-X. Zhang, P. Tang, G. Yang, J. Sofo, W. Duan, and C.-X. Liu, 2016, 2D Mater. **3**, 034006.
Cao, Y., V. Fatemi, S. Fang, K. Watanabe, T. Taniguchi, E. Kaxiras, and P. Jarillo-Herrero, 2018, Nature (London) **556**7699, 43.
Cao, Y., *et al.*, 2018, Nature (London) **556**7699, 80.
Castro Neto, A. H., F. Guinea, N. M. R. Peres, K. S. Novoselov, and A. K. Geim, 2009, Rev. Mod. Phys. **81**, 109.
Ceresoli, D., T. Thonhauser, D. Vanderbilt, and R. Resta, 2006, Phys. Rev. B **74**, 024408.
Chang, C., M. Liu, Z. Zhang, Y. Wang, K. He, and Q. Xue, 2016, Sci. China Phys. Mech. Astron. **59**, 637501.
Chang, C.-Z., 2020, Nat. Mater. **19**, 484.
Chang, C.-Z., K. He, L.-L. Wang, X.-C. Ma, M.-H. Liu, Z.-C. Zhang, X. Chen, Y.-Y. Wang, and Q.-K. Xue, 2011, in *Spin*, Vol. 1 (World Scientific, Singapore), pp. 21–25.
Chang, C.-Z., and M. Li, 2016, J. Phys. Condens. Matter **28**, 123002.
Chang, C.-Z., W. Zhao, D. Y. Kim, P. Wei, J. K. Jain, C. Liu, M. H. Chan, and J. S. Moodera, 2015, Phys. Rev. Lett. **115**, 057206.
Chang, C.-Z., W. Zhao, D. Y. Kim, H. Zhang, B. A. Assaf, D. Heiman, S.-C. Zhang, C. Liu, M. H. Chan, and J. S. Moodera, 2015, Nat. Mater. **14**, 473.
Chang, C.-Z., W. Zhao, J. Li, J. Jain, C. Liu, J. S. Moodera, and M. H. Chan, 2016, Phys. Rev. Lett. **117**, 126802.
Chang, C.-Z., *et al.*, 2013a, Science **340**6129, 167.
Chang, C.-Z., *et al.*, 2013b, Adv. Mater. **25**, 1065.
Chang, C.-Z., *et al.*, 2014, Phys. Rev. Lett. **112**, 056801.
Checkelsky, J., R. Yoshimi, A. Tsukazaki, K. Takahashi, Y. Kozuka, J. Falson, M. Kawasaki, and Y. Tokura, 2014, Nat. Phys. **10**, 731.
Chen, B., *et al.*, 2019, Nat. Commun. **10**, 1.
Chen, C.-Z., J. J. He, D.-H. Xu, and K. T. Law, 2017, Phys. Rev. B **96**, 041118.
Chen, C.-Z., H. Liu, and X. Xie, 2019, Phys. Rev. Lett. **122**, 026601.
Chen, C.-Z., Y.-M. Xie, J. Liu, P. A. Lee, and K. T. Law, 2018, Phys. Rev. B **97**, 104504.
Chen, G., *et al.*, 2020, Nature (London) **579**, 56.
Chen, R., S. Li, H.-P. Sun, Q. Liu, Y. Zhao, H.-Z. Lu, and X. Xie, 2021, Phys. Rev. B **103**, L241409.
Chen, S., *et al.*, 2021, Nat. Phys. **17**, 374.
Chen, S.-P., Z.-Q. Huang, C. P. Crisostomo, C.-H. Hsu, F.-C. Chuang, H. Lin, and A. Bansil, 2016, Sci. Rep. **6**, 1.
Chen, Y., *et al.*, 2009, Science **325**5937, 178.
Chen, Y., *et al.*, 2010, Science **329**5992, 659.
Chen, Y., *et al.*, 2019, Phys. Rev. X **9**, 041040.
Chen, Y., *et al.*, 2020, Phys. Rev. Mater. **4**, 064411.
Cheraghchi, H., and T. Sabze, 2020, J. Magn. Magn. Mater. **513**, 166923.
Chien, Y.-J., Z. Zhou, and C. Uher, 2005, J. Cryst. Growth **283**, 309.
Choi, Y., *et al.*, 2021, Nature (London) **589**, 536.
Chu, R.-L., J. Shi, and S.-Q. Shen, 2011, Phys. Rev. B **84**, 085312.
Connolly, M., R. Puddy, D. Logoteta, P. Marconcini, M. Roy, J. Griffiths, G. Jones, P. Maksym, M. Macucci, and C. Smith, 2012, Nano Lett. **12**, 5448.
Cui, J., M. Shi, H. Wang, F. Yu, T. Wu, X. Luo, J. Ying, and X. Chen, 2019, Phys. Rev. B **99**, 155125.
Das, A., Y. Ronen, Y. Most, Y. Oreg, M. Heiblum, and H. Shtrikman, 2012, Nat. Phys. **8**, 887.
de Lima, F. C., G. J. Ferreira, and R. Miwa, 2018, Phys. Chem. Chem. Phys. **20**, 22652.
Deng, M., C. Yu, G. Huang, M. Larsson, P. Caroff, and H. Xu, 2012, Nano Lett. **12**, 6414.
Deng, X., S. Qi, Y. Han, K. Zhang, X. Xu, and Z. Qiao, 2017, Phys. Rev. B **95**, 121410.
Deng, Y., Y. Yu, M. Z. Shi, Z. Guo, Z. Xu, J. Wang, X. H. Chen, and Y. Zhang, 2020, Science **367**, 895.
Devakul, T., and L. Fu, 2022, Phys. Rev. X **12**, 021031.
Dietl, T., and H. Ohno, 2014, Rev. Mod. Phys. **86**, 187.
Ding, L., C. Hu, F. Ye, E. Feng, N. Ni, and H. Cao, 2020, Phys. Rev. B **101**, 020412.

Dos Santos, J. L., N. Peres, and A. C. Neto, 2007, Phys. Rev. Lett. **99**, 256802.
Dziom, V., *et al.*, 2017, Nat. Commun. **8**, 15197.
Essin, A. M., J. E. Moore, and D. Vanderbilt, 2009, Phys. Rev. Lett. **102**, 146805.
Ezawa, M., 2012, Phys. Rev. Lett. **109**, 055502.
Ezawa, M., 2013, Phys. Rev. B **87**, 155415.
Fang, C., and L. Fu, 2019, Sci. Adv. **5**, eaat2374.
Fang, C., M. J. Gilbert, and B. A. Bernevig, 2014, Phys. Rev. Lett. **112**, 046801.
Feng, X., *et al.*, 2016, Adv. Mater. **28**, 6386.
Feng, Y., *et al.*, 2015, Phys. Rev. Lett. **115**, 126801.
Fijalkowski, K., *et al.*, 2021, Phys. Rev. B **103**, 235111.
Fox, E. J., I. T. Rosen, Y. Yang, G. R. Jones, R. E. Elmquist, X. Kou, L. Pan, K. L. Wang, and D. Goldhaber-Gordon, 2018, Phys. Rev. B **98**, 075145.
Fradkin, E., E. Dagotto, and D. Boyanovsky, 1986, Phys. Rev. Lett. **57**, 2967.
Fu, L., and C. L. Kane, 2007, Phys. Rev. B **76**, 045302.
Fu, L., C. L. Kane, and E. J. Mele, 2007, Phys. Rev. Lett. **98**, 106803.
Gao, A., *et al.*, 2021, Nature (London) **595**, 521.
Garrity, K. F., and D. Vanderbilt, 2013, Phys. Rev. Lett. **110**, 116802.
Garrity, K. F., and D. Vanderbilt, 2014, Phys. Rev. B **90**, 121103.
Ge, J., Y. Liu, J. Li, H. Li, T. Luo, Y. Wu, Y. Xu, and J. Wang, 2020, Natl. Sci. Rev. **7**, 1280.
Ge, W., P. M. Sass, J. Yan, S. H. Lee, Z. Mao, and W. Wu, 2021, Phys. Rev. B **103**, 134403.
Giovannetti, G., P. A. Khomyakov, G. Brocks, P. J. Kelly, and J. Van Den Brink, 2007, Phys. Rev. B **76**, 073103.
Girvin, S., and R. Prange, 1990, *The Quantum Hall Effect*, Graduate Texts in Contemporary Physics (Springer-Verlag, New York), https://link.springer.com/content/pdf/10.1007/978-1-4612-3350-3.pdf?pdf=button.
Gong, Y., *et al.*, 2019, Chin. Phys. Lett. **36**, 076801.
Goodenough, J. B., 1955, Phys. Rev. **100**, 564.
Gordon, K. N., *et al.*, 2019, arXiv:1910.13943.
Götz, M., *et al.*, 2018, Appl. Phys. Lett. **112**, 072102.
Grauer, S., K. Fijalkowski, S. Schreyeck, M. Winnerlein, K. Brunner, R. Thomale, C. Gould, and L. Molenkamp, 2017, Phys. Rev. Lett. **118**, 246801.
Grauer, S., S. Schreyeck, M. Winnerlein, K. Brunner, C. Gould, and L. Molenkamp, 2015, Phys. Rev. B **92**, 201304.
Haim, A., R. Ilan, and J. Alicea, 2019, Phys. Rev. Lett. **123**, 046801.
Haldane, F. D. M., 1988, Phys. Rev. Lett. **61**, 2015.
Hall, E. H., 1880, Am. J. Sci. **s3-20**, 161.
Halperin, B. I., 1987, Jpn. J. Appl. Phys. **26**, 1913.
Hao, Y.-J., *et al.*, 2019, Phys. Rev. X **9**, 041038.
Hasan, M. Z., and C. L. Kane, 2010, Rev. Mod. Phys. **82**, 3045.
He, K., Y. Wang, and Q.-K. Xue, 2018, Annu. Rev. Condens. Matter Phys. **9**, 329.
He, Q. L., *et al.*, 2017, Science **357**6348, 294.
He, W.-Y., D. Goldhaber-Gordon, and K. T. Law, 2020, Nat. Commun. **11**, 1.
Hofstadter, D. R., 1976, Phys. Rev. B **14**, 2239.
Högl, P., T. Frank, K. Zollner, D. Kochan, M. Gmitra, and J. Fabian, 2020, Phys. Rev. Lett. **124**, 136403.
Hor, Y. S., *et al.*, 2010, Phys. Rev. B **81**, 195203.
Hsu, C.-H., *et al.*, 2017, Phys. Rev. B **96**, 165426.
Hu, C., *et al.*, 2020a, Sci. Adv. **6**, eaba4275.
Hu, C., *et al.*, 2020b, Nat. Commun. **11**, 1.
Hu, Y., *et al.*, 2020, Phys. Rev. B **101**, 161113.
Huan, S., *et al.*, 2021, Phys. Rev. Lett. **126**, 246601.
Huang, C., J. Zhou, H. Wu, K. Deng, P. Jena, and E. Kan, 2017, Phys. Rev. B **95**, 045113.
Huang, Y., F. Setiawan, and J. D. Sau, 2018, Phys. Rev. B **97**, 100501.
Huang, Z., M.-H. Du, J. Yan, and W. Wu, 2020, Phys. Rev. Mater. **4**, 121202.
Huckestein, B., 1995, Rev. Mod. Phys. **67**, 357.
Jeckelmann, B., and B. Jeanneret, 2001, Rep. Prog. Phys. **64**, 1603.
Jeon, S., Y. Xie, J. Li, Z. Wang, B. A. Bernevig, and A. Yazdani, 2017, Science **358**6364, 772.
Ji, W., and X.-G. Wen, 2018, Phys. Rev. Lett. **120**, 107002.
Ji, W.-x., *et al.*, 2016, New J. Phys. **18**, 083002.
Jiang, G., *et al.*, 2018, Chin. Phys. Lett. **35**, 076802.
Jiang, H., Z. Qiao, H. Liu, and Q. Niu, 2012, Phys. Rev. B **85**, 045445.
Jiang, J., *et al.*, 2020, Nat. Mater. **19**, 732.
Jiang, Q., *et al.*, 2021, Phys. Rev. B **103**, 205111.
Jiang, Y., C. Song, Z. Li, M. Chen, R. L. Greene, K. He, L. Wang, X. Chen, X. Ma, and Q.-K. Xue, 2015, Phys. Rev. B **92**, 195418.
Jiang, Y., Y. Wang, M. Chen, Z. Li, C. Song, K. He, L. Wang, X. Chen, X. Ma, and Q.-K. Xue, 2012, Phys. Rev. Lett. **108**, 016401.
Jin, K.-H., and S.-H. Jhi, 2015, Sci. Rep. **5**, 8426.
Jo, N. H., L.-L. Wang, R.-J. Slager, J. Yan, Y. Wu, K. Lee, B. Schrunk, A. Vishwanath, and A. Kaminski, 2020, Phys. Rev. B **102**, 045130.
Jungwirth, T., J. Sinova, J. Mašek, J. Kučera, and A. MacDonald, 2006, Rev. Mod. Phys. **78**, 809.
Kagerer, P., *et al.*, 2020, J. Appl. Phys. **128**, 135303.
Kaloni, T. P., N. Singh, and U. Schwingenschlögl, 2014, Phys. Rev. B **89**, 035409.
Kanamori, J., 1959, J. Phys. Chem. Solids **10**, 87.
Kandala, A., A. Richardella, S. Kempinger, C.-X. Liu, and N. Samarth, 2015, Nat. Commun. **6**, 7434.
Kane, C. L., and E. J. Mele, 2005, Phys. Rev. Lett. **95**, 226801.
Kang, J., and O. Vafek, 2019, Phys. Rev. Lett. **122**, 246401.
Kasuya, T., 1956, Prog. Theor. Phys. **16**, 45.
Kawaji, S., 1996, Semicond. Sci. Technol. **11**, 1546.
Kawamura, M., M. Mogi, R. Yoshimi, A. Tsukazaki, Y. Kozuka, K. S. Takahashi, M. Kawasaki, and Y. Tokura, 2018, Phys. Rev. B **98**, 140404.
Kawamura, M., M. Mogi, R. Yoshimi, A. Tsukazaki, Y. Kozuka, K. S. Takahashi, M. Kawasaki, and Y. Tokura, 2020, Phys. Rev. B **102**, 041301.
Kawamura, M., R. Yoshimi, A. Tsukazaki, K. S. Takahashi, M. Kawasaki, and Y. Tokura, 2017, Phys. Rev. Lett. **119**, 016803.
Kayyalha, M., *et al.*, 2020, Science **367**6473, 64.
Kim, J., S.-H. Jhi, A. MacDonald, and R. Wu, 2017, Phys. Rev. B **96**, 140410.
Kim, K., A. DaSilva, S. Huang, B. Fallahazad, S. Larentis, T. Taniguchi, K. Watanabe, B. J. LeRoy, A. H. MacDonald, and E. Tutuc, 2017, Proc. Natl. Acad. Sci. U.S.A. **114**, 3364.
Kim, S., D. Kurebayashi, and K. Nomura, 2019, J. Phys. Soc. Jpn. **88**, 083704.
Klimovskikh, I. I., *et al.*, 2020, npj Quantum Mater. **5**, 54.
Klinovaja, J., Y. Tserkovnyak, and D. Loss, 2015, Phys. Rev. B **91**, 085426.
Klitzing, K. v., G. Dorda, and M. Pepper, 1980, Phys. Rev. Lett. **45**, 494.
König, M., S. Wiedmann, C. Brüne, A. Roth, H. Buhmann, L. W. Molenkamp, X.-L. Qi, and S.-C. Zhang, 2007, Science **318**, 766.
Koroteev, Y. M., G. Bihlmayer, J. Gayone, E. V. Chulkov, S. Blügel, P. M. Echenique, and P. Hofmann, 2004, Phys. Rev. Lett. **93**, 046403.

Kou, X., *et al.*, 2014, Phys. Rev. Lett. **113**, 137201.
Kou, X., *et al.*, 2015, Nat. Commun. **6**, 8474.
Krupin, O., G. Bihlmayer, K. Starke, S. Gorovikov, J. Prieto, K. Döbrich, S. Blügel, and G. Kaindl, 2005, Phys. Rev. B **71**, 201403.
Kuroda, K., *et al.*, 2017, Nat. Mater. **16**, 1090.
Kwan, Y. H., Y. Hu, S. H. Simon, and S. Parameswaran, 2021, Phys. Rev. Lett. **126**, 137601.
Lachman, E. O., *et al.*, 2015, Sci. Adv. **1**, e1500740.
Lachman, E. O., *et al.*, 2017, npj Quantum Mater. **2**, 70.
Landau, L., 1930, Z. Phys. **64**, 629.
Landau, L. D., and E. M. Lifshitz, 2013, *Quantum Mechanics: Non-relativistic Theory*, Course of Theoretical Physics Vol. 3 (Elsevier, New York).
Lapano, J., *et al.*, 2020, Phys. Rev. Mater. **4**, 111201.
Ledwith, P. J., G. Tarnopolsky, E. Khalaf, and A. Vishwanath, 2020, Phys. Rev. Res. **2**, 023237.
Lee, D. K., and J. Chalker, 1994, Phys. Rev. Lett. **72**, 1510.
Lee, I., *et al.*, 2015, Proc. Natl. Acad. Sci. U.S.A. **112**, 1316.
Lee, S. H., *et al.*, 2019, Phys. Rev. Res. **1**, 012011.
Lee, S. H., *et al.*, 2021, Phys. Rev. X **11**, 031032.
Lei, C., S. Chen, and A. H. MacDonald, 2020, Proc. Natl. Acad. Sci. U.S.A. **117**, 27224.
Lei, C., and A. H. MacDonald, 2021, Phys. Rev. Mater. **5**, L051201.
Li, G., A. Luican, J. L. Dos Santos, A. C. Neto, A. Reina, J. Kong, and E. Andrei, 2010, Nat. Phys. **6**, 109.
Li, H., C.-Z. Chen, H. Jiang, and X. Xie, 2021, Phys. Rev. Lett. **127**, 236402.
Li, H., H. Jiang, C.-Z. Chen, and X. Xie, 2021, Phys. Rev. Lett. **126**, 156601.
Li, H., S. Liu, C. Liu, J. Zhang, Y. Xu, R. Yu, Y. Wu, Y. Zhang, and S. Fan, 2020, Phys. Chem. Chem. Phys. **22**, 556.
Li, H., *et al.*, 2019, Phys. Rev. X **9**, 041039.
Li, H., *et al.*, 2021, arXiv:2106.10599.
Li, J., Y. Li, S. Du, Z. Wang, B.-L. Gu, S.-C. Zhang, K. He, W. Duan, and Y. Xu, 2019, Sci. Adv. **5**, eaaw5685.
Li, J., K. Wang, K. J. McFaul, Z. Zern, Y. Ren, K. Watanabe, T. Taniguchi, Z. Qiao, and J. Zhu, 2016, Nat. Nanotechnol. **11**, 1060.
Li, J., R.-X. Zhang, Z. Yin, J. Zhang, K. Watanabe, T. Taniguchi, C. Liu, and J. Zhu, 2018, Science **362**, 1149.
Li, M., C.-Z. Chang, L. Wu, J. Tao, W. Zhao, M. H. Chan, J. S. Moodera, J. Li, and Y. Zhu, 2015, Phys. Rev. Lett. **114**, 146802.
Li, P., 2019, Phys. Chem. Chem. Phys. **21**, 11150.
Li, T., *et al.*, 2021a, Nature (London) **597**, 350.
Li, T., *et al.*, 2021b, Nature (London) **600**, 641.
Li, W., *et al.*, 2016, Sci. Rep. **6**, 32732.
Li, Y., D. West, H. Huang, J. Li, S. Zhang, and W. Duan, 2015, Phys. Rev. B **92**, 201403.
Li, Y.-H., and R. Cheng, 2021, Phys. Rev. Lett. **126**, 026601.
Li, Y.-Y., *et al.*, 2010, Adv. Mater. **22**, 4002.
Lian, B., Z.-D. Song, N. Regnault, D. K. Efetov, A. Yazdani, and B. A. Bernevig, 2021, Phys. Rev. B **103**, 205414.
Lian, B., J. Wang, X.-Q. Sun, A. Vaezi, and S.-C. Zhang, 2018, Phys. Rev. B **97**, 125408.
Liang, Z., *et al.*, 2020, Phys. Rev. B **102**, 161115.
Lin, J.-X., Y.-H. Zhang, E. Morissette, Z. Wang, S. Liu, D. Rhodes, K. Watanabe, T. Taniguchi, J. Hone, and J. Li, 2022, Science **375**, 437.
Lin, W., *et al.*, 2022, Phys. Rev. B **105**, 165411.
Lippertz, G., A. Bliesener, A. Uday, L. M. Pereira, A. Taskin, and Y. Ando, 2022, Phys. Rev. B **106**, 045419.
Liu, C., T. L. Hughes, X.-L. Qi, K. Wang, and S.-C. Zhang, 2008, Phys. Rev. Lett. **100**, 236601.
Liu, C., Y. Wang, H. Li, Y. Wu, Y. Li, J. Li, K. He, Y. Xu, J. Zhang, and Y. Wang, 2020, Nat. Mater. **19**, 522.
Liu, C., *et al.*, 2020, Phys. Rev. X **10**, 041063.
Liu, C., *et al.*, 2021, Nat. Commun. **12**, 4647.
Liu, C.-C., J.-J. Zhou, and Y. Yao, 2015, Phys. Rev. B **91**, 165430.
Liu, C.-X., X.-L. Qi, X. Dai, Z. Fang, and S.-C. Zhang, 2008, Phys. Rev. Lett. **101**, 146802.
Liu, C.-X., S.-C. Zhang, and X.-L. Qi, 2016, Annu. Rev. Condens. Matter Phys. **7**, 301.
Liu, D., *et al.*, 2019, Science **365**, 1282.
Liu, J., and X. Dai, 2021a, Nat. Rev. Phys. **3**, 367.
Liu, J., and X. Dai, 2021b, Phys. Rev. B **103**, 035427.
Liu, J., J. Liu, and X. Dai, 2019, Phys. Rev. B **99**, 155415.
Liu, J., Z. Ma, J. Gao, and X. Dai, 2019, Phys. Rev. X **9**, 031021.
Liu, M., W. Wang, A. R. Richardella, A. Kandala, J. Li, A. Yazdani, N. Samarth, and N. P. Ong, 2016, Sci. Adv. **2**, e1600167.
Liu, Q., C.-X. Liu, C. Xu, X.-L. Qi, and S.-C. Zhang, 2009, Phys. Rev. Lett. **102**, 156603.
Liu, X., Z. Wang, K. Watanabe, T. Taniguchi, O. Vafek, and J. Li, 2021, Science **3716**535, 1261.
Liu, Y., *et al.*, 2021, Phys. Rev. X **11**, 021033.
Lu, H.-Z., 2019, Natl. Sci. Rev. **6**, 208.
Lu, X., *et al.*, 2019, Nature (London) **574**, 653.
Luo, F., X. Hao, Y. Jia, J. Yao, Q. Meng, S. Zhai, J. Wu, W. Dou, and M. Zhou, 2021, Nanoscale **13**, 2527.
Ma, X.-M., *et al.*, 2020, Phys. Rev. B **102**, 245136.
MacDonald, A., 1983, Phys. Rev. B **28**, 6713.
MacDonald, A., 1994, in *Mesoscopic Quantum Physics*, Proceedings of the Les Houches Summer School, Session LXI, edited by E. Akkermans, G. Montambaux, J. L. Pichard, and J. Zinn-Justin (Springer-Verlag, Berlin).
MacDonald, A. H., J. Jung, and F. Zhang, **2012**, Phys. Scr. 014012.
Martin, I., and C. Batista, 2008, Phys. Rev. Lett. **101**, 156402.
Martin, I., Y. M. Blanter, and A. Morpurgo, 2008, Phys. Rev. Lett. **100**, 036804.
Meng, W., X. Zhang, W. Yu, Y. Liu, L. Tian, X. Dai, and G. Liu, 2021, Appl. Surf. Sci. **551**, 149390.
Mensz, P., and D. Tsui, 1989, Phys. Rev. B **40**, 3919.
Min, H., G. Borghi, M. Polini, and A. H. MacDonald, 2008, Phys. Rev. B **77**, 041407.
Mogi, M., M. Kawamura, A. Tsukazaki, R. Yoshimi, K. S. Takahashi, M. Kawasaki, and Y. Tokura, 2017, Sci. Adv. **3**, eaao1669.
Mogi, M., M. Kawamura, R. Yoshimi, A. Tsukazaki, Y. Kozuka, N. Shirakawa, K. Takahashi, M. Kawasaki, and Y. Tokura, 2017, Nat. Mater. **16**, 516.
Mogi, M., R. Yoshimi, A. Tsukazaki, K. Yasuda, Y. Kozuka, K. Takahashi, M. Kawasaki, and Y. Tokura, 2015, Appl. Phys. Lett. **107**, 182401.
Mogi, M., *et al.*, 2019, Phys. Rev. Lett. **123**, 016804.
Moore, J. E., and L. Balents, 2007, Phys. Rev. B **75**, 121306.
Morali, N., R. Batabyal, P. K. Nag, E. Liu, Q. Xu, Y. Sun, B. Yan, C. Felser, N. Avraham, and H. Beidenkopf, 2019, Science **365**, 1286.
Morimoto, T., A. Furusaki, and N. Nagaosa, 2015, Phys. Rev. B **92**, 085113.
Mourik, V., K. Zuo, S. M. Frolov, S. Plissard, E. P. Bakkers, and L. P. Kouwenhoven, 2012, Science **336**, 1003.
Muechler, L., E. Liu, J. Gayles, Q. Xu, C. Felser, and Y. Sun, 2020, Phys. Rev. B **101**, 115106.
Murakami, T., Y. Nambu, T. Koretsune, G. Xiangyu, T. Yamamoto, C. M. Brown, and H. Kageyama, 2019, Phys. Rev. B **100**, 195103.

Nadj-Perge, S., I. K. Drozdov, J. Li, H. Chen, S. Jeon, J. Seo, A. H. MacDonald, B. A. Bernevig, and A. Yazdani, 2014, Science **346**, 602.
Nagaosa, N., J. Sinova, S. Onoda, A. H. MacDonald, and N. P. Ong, 2010, Rev. Mod. Phys. **82**, 1539.
Nandkishore, R., and L. Levitov, 2010, Phys. Rev. B **82**, 115124.
Nayak, C., S. H. Simon, A. Stern, M. Freedman, and S. D. Sarma, 2008, Rev. Mod. Phys. **80**, 1083.
Neupert, T., L. Santos, C. Chamon, and C. Mudry, 2011, Phys. Rev. Lett. **106**, 236804.
Nevola, D., H. X. Li, J.-Q. Yan, R. Moore, H.-N. Lee, H. Miao, and P. D. Johnson, 2020, Phys. Rev. Lett. **125**, 117205.
Nielsen, H. B., and M. Ninomiya, 1981a, Nucl. Phys. **B185**, 20.
Nielsen, H. B., and M. Ninomiya, 1981b, Nucl. Phys. B **193**, 173.
Ning, W., and Z. Mao, 2020, APL Mater. **8**, 090701.
Niu, C., G. Bihlmayer, H. Zhang, D. Wortmann, S. Blügel, and Y. Mokrousov, 2015, Phys. Rev. B **91**, 041303.
Nomura, K., and N. Nagaosa, 2011, Phys. Rev. Lett. **106**, 166802.
Nuckolls, K. P., M. Oh, D. Wong, B. Lian, K. Watanabe, T. Taniguchi, B. A. Bernevig, and A. Yazdani, 2020, Nature (London) **588**, 610.
Ohno, H., 1999, J. Magn. Magn. Mater. **200**, 110.
Ohno, H., D. Chiba, F. Matsukura, T. Omiya, E. Abe, T. Dietl, Y. Ohno, and K. Ohtani, 2000, Nature (London) **408**, 944.
Okada, K. N., Y. Takahashi, M. Mogi, R. Yoshimi, A. Tsukazaki, K. S. Takahashi, N. Ogawa, M. Kawasaki, and Y. Tokura, 2016, Nat. Commun. **7**, 12245.
Okazaki, Y., *et al.*, 2020, Appl. Phys. Lett. **116**, 143101.
Okazaki, Y., *et al.*, 2022, Nat. Phys. **18**, 25.
Onoda, M., and N. Nagaosa, 2003, Phys. Rev. Lett. **90**, 206601.
Otrokov, M. M., I. P. Rusinov, M. Blanco-Rey, M. Hoffmann, A. Y. Vyazovskaya, S. V. Eremeev, A. Ernst, P. M. Echenique, A. Arnau, and E. V. Chulkov, 2019, Phys. Rev. Lett. **122**, 107202.
Otrokov, M. M., *et al.*, 2017, 2D Mater. **4**, 025082.
Otrokov, M. M., *et al.*, 2019, Nature (London) **576**, 416.
Ou, Y., *et al.*, 2018, Adv. Mater. **30**, 1703062.
Ovchinnikov, D., *et al.*, 2021, Nano Lett. **21**, 2544.
Pan, H., Z. Li, C.-C. Liu, G. Zhu, Z. Qiao, and Y. Yao, 2014, Phys. Rev. Lett. **112**, 106802.
Pan, H., M. Xie, F. Wu, and S. D. Sarma, 2022, Phys. Rev. Lett. **129**, 056804.
Pan, J., J. Yu, Y.-F. Zhang, S. Du, A. Janotti, C.-X. Liu, and Q. Yan, 2020, npj Comput. Mater. **6**, 1.
Peccei, R. D., and H. R. Quinn, 1977, Phys. Rev. Lett. **38**, 1440.
Peixoto, T. R., *et al.*, 2016, Phys. Rev. B **94**, 195140.
Pham, A., and P. Ganesh, 2020, arXiv:2003.05840.
Pierce, A. T., *et al.*, 2021, Nat. Phys. **17**, 1210.
Pikulin, D., and T. Hyart, 2014, Phys. Rev. Lett. **112**, 176403.
Po, H. C., L. Zou, T. Senthil, and A. Vishwanath, 2019, Phys. Rev. B **99**, 195455.
Po, H. C., L. Zou, A. Vishwanath, and T. Senthil, 2018, Phys. Rev. X **8**, 031089.
Poirier, W., and F. Schopfer, 2009, Eur. Phys. J. Special Topics **172**, 207.
Polshyn, H., *et al.*, 2020, Nature (London) **588**, 66.
Pournaghavi, N., A. Pertsova, A. MacDonald, and C. M. Canali, 2021, Phys. Rev. B **104**, L201102.
Qi, X.-L., T. L. Hughes, and S.-C. Zhang, 2008, Phys. Rev. B **78**, 195424.
Qi, X.-L., T. L. Hughes, and S.-C. Zhang, 2010, Phys. Rev. B **82**, 184516.
Qi, X.-L., Y.-S. Wu, and S.-C. Zhang, 2006, Phys. Rev. B **74**, 085308.
Qi, X.-L., and S.-C. Zhang, 2011, Rev. Mod. Phys. **83**, 1057.
Qian, J., J. Zhang, Q. Wu, and Z. Lin, 2019, Appl. Phys. Lett. **114**, 053105.
Qiao, Z., Y. Han, L. Zhang, K. Wang, X. Deng, H. Jiang, S. A. Yang, J. Wang, and Q. Niu, 2016, Phys. Rev. Lett. **117**, 056802.
Qiao, Z., H. Jiang, X. Li, Y. Yao, and Q. Niu, 2012, Phys. Rev. B **85**, 115439.
Qiao, Z., S. A. Yang, W. Feng, W.-K. Tse, J. Ding, Y. Yao, J. Wang, and Q. Niu, 2010, Phys. Rev. B **82**, 161414.
Quhe, R., *et al.*, 2012, NPG Asia Mater. **4**, e6.
Raghu, S., X.-L. Qi, C. Honerkamp, and S.-C. Zhang, 2008, Phys. Rev. Lett. **100**, 156401.
Repellin, C., and T. Senthil, 2020, Phys. Rev. Res. **2**, 023238.
Ribeiro-Palau, R., C. Zhang, K. Watanabe, T. Taniguchi, J. Hone, and C. R. Dean, 2018, Science **361**, 690.
Rienks, E. D., *et al.*, 2019, Nature (London) **576**, 423.
Rokhinson, L. P., X. Liu, and J. K. Furdyna, 2012, Nat. Phys. **8**, 795.
Rosen, I. T., E. J. Fox, X. Kou, L. Pan, K. L. Wang, and D. Goldhaber-Gordon, 2017, npj Quantum Mater. **2**, 69.
Roy, R., 2009, Phys. Rev. B **79**, 195322.
Ruderman, M. A., and C. Kittel, 1954, Phys. Rev. **96**, 99.
Saito, Y., J. Ge, L. Rademaker, K. Watanabe, T. Taniguchi, D. A. Abanin, and A. F. Young, 2021, Nat. Phys. **17**, 478.
San-Jose, P., A. Gutiérrez-Rubio, M. Sturla, and F. Guinea, 2014, Phys. Rev. B **90**, 075428.
Sass, P. M., W. Ge, J. Yan, D. Obeysekera, J. Yang, and W. Wu, 2020, Nano Lett. **20**, 2609.
Sass, P. M., J. Kim, D. Vanderbilt, J. Yan, and W. Wu, 2020, Phys. Rev. Lett. **125**, 037201.
Sato, K., *et al.*, 2010, Rev. Mod. Phys. **82**, 1633.
Schopfer, F., and W. Poirier, 2007, J. Appl. Phys. **102**, 054903.
Sekine, A., and K. Nomura, 2021, J. Appl. Phys. **129**, 141101.
Semenoff, G. W., 1984, Phys. Rev. Lett. **53**, 2449.
Seo, K., V. N. Kotov, and B. Uchoa, 2019, Phys. Rev. Lett. **122**, 246402.
Serlin, M., C. Tschirhart, H. Polshyn, Y. Zhang, J. Zhu, K. Watanabe, T. Taniguchi, L. Balents, and A. Young, 2020, Science **367** 6480, 900.
Sharpe, A. L., E. J. Fox, A. W. Barnard, J. Finney, K. Watanabe, T. Taniguchi, M. Kastner, and D. Goldhaber-Gordon, 2019, Science **365**, 605.
Sharpe, A. L., E. J. Fox, A. W. Barnard, J. Finney, K. Watanabe, T. Taniguchi, M. A. Kastner, and D. Goldhaber-Gordon, 2021, Nano Lett. **21**, 4299.
Shi, J., G. Vignale, D. Xiao, and Q. Niu, 2007, Phys. Rev. Lett. **99**, 197202.
Shi, J., J. Zhu, and A. MacDonald, 2021, Phys. Rev. B **103**, 075122.
Shi, M., B. Lei, C. Zhu, D. Ma, J. Cui, Z. Sun, J. Ying, and X. Chen, 2019, Phys. Rev. B **100**, 155144.
Singh, V., and M. M. Deshmukh, 2009, Phys. Rev. B **80**, 081404.
Śliwa, C., C. Autieri, J. A. Majewski, and T. Dietl, 2021, Phys. Rev. B **104**, L220404.
Song, Z., Z. Wang, W. Shi, G. Li, C. Fang, and B. A. Bernevig, 2019, Phys. Rev. Lett. **123**, 036401.
Song, Z.-D., B. Lian, R. Queiroz, R. Ilan, B. A. Bernevig, and A. Stern, 2021, Phys. Rev. Lett. **127**, 016602.
Song, Z.-D., B. Lian, N. Regnault, and B. A. Bernevig, 2021, Phys. Rev. B **103**, 205412.
Stormer, H. L., D. C. Tsui, and A. C. Gossard, 1999, Rev. Mod. Phys. **71**, S298.
Streda, P., 1982, J. Phys. C **15**, L717.

Sun, K., Z. Gu, H. Katsura, and S. D. Sarma, 2011, Phys. Rev. Lett. **106**, 236803.

Swatek, P., Y. Wu, L.-L. Wang, K. Lee, B. Schrunk, J. Yan, and A. Kaminski, 2020, Phys. Rev. B **101**, 161109.

Tai, L., *et al.*, 2021, arXiv:2103.09878.

Tang, C., *et al.*, 2017, Sci. Adv. **3**, e1700307.

Tang, E., J.-W. Mei, and X.-G. Wen, 2011, Phys. Rev. Lett. **106**, 236802.

Tao, Z., *et al.*, 2022, arXiv:2208.07452.

Tcakaev, A., *et al.*, 2020, Phys. Rev. B **101**, 045127.

Thonhauser, T., 2011, Int. J. Mod. Phys. B **25**, 1429.

Thonhauser, T., D. Ceresoli, D. Vanderbilt, and R. Resta, 2005, Phys. Rev. Lett. **95**, 137205.

Thouless, D. J., M. Kohmoto, M. P. Nightingale, and M. den Nijs, 1982, Phys. Rev. Lett. **49**, 405.

Tian, S., *et al.*, 2020, Phys. Rev. B **102**, 035144.

Tokura, Y., K. Yasuda, and A. Tsukazaki, 2019, Nat. Rev. Phys. **1**, 126.

Trang, C. X., *et al.*, 2021, ACS Nano **15**, 13444.

Tschirhart, C., *et al.*, 2021, Science **372**, 1323.

Tschirhart, C., *et al.*, 2022, arXiv:2205.02823.

Tse, W.-K., Z. Qiao, Y. Yao, A. MacDonald, and Q. Niu, 2011, Phys. Rev. B **83**, 155447.

Turner, A. M., Y. Zhang, R. S. Mong, and A. Vishwanath, 2012, Phys. Rev. B **85**, 165120.

Upadhyaya, P., and Y. Tserkovnyak, 2016, Phys. Rev. B **94**, 020411.

Van Vleck, J. H., 1932, *The Theory of Electric and Magnetic Susceptibilities* (Clarendon Press, Oxford).

Van Vleck, J. H., 1953, Rev. Mod. Phys. **25**, 220.

Varnava, N., and D. Vanderbilt, 2018, Phys. Rev. B **98**, 245117.

Varnava, N., J. H. Wilson, J. Pixley, and D. Vanderbilt, 2021, Nat. Commun. **12**, 3998.

Vidal, R., *et al.*, 2019a, Phys. Rev. B **100**, 121104.

Vidal, R. C., *et al.*, 2019b, Phys. Rev. X **9**, 041065.

Vila, M., J. H. Garcia, and S. Roche, 2021, Phys. Rev. B **104**, L161113.

Wang, C., H.-P. Sun, H.-Z. Lu, and X. Xie, 2017, Phys. Rev. Lett. **119**, 136806.

Wang, D., *et al.*, 2018, Science **362**, 333.

Wang, F., *et al.*, 2018, Phys. Rev. B **97**, 115414.

Wang, F., *et al.*, 2019, Nano Lett. **19**, 2945.

Wang, G., *et al.*, 2010, Nano Res. **3**, 874.

Wang, J., B. Lian, X.-L. Qi, and S.-C. Zhang, 2015, Phys. Rev. B **92**, 081107.

Wang, J., B. Lian, H. Zhang, and S.-C. Zhang, 2013, Phys. Rev. Lett. **111**, 086803.

Wang, J., B. Lian, and S.-C. Zhang, 2014, Phys. Rev. B **89**, 085106.

Wang, J., Q. Zhou, B. Lian, and S.-C. Zhang, 2015, Phys. Rev. B **92**, 064520.

Wang, P., J. Ge, J. Li, Y. Liu, Y. Xu, and J. Wang, 2021, Innovation **2**, 100098.

Wang, Q.-Z., X. Liu, H.-J. Zhang, N. Samarth, S.-C. Zhang, and C.-X. Liu, 2014, Phys. Rev. Lett. **113**, 147201.

Wang, S.-W., D. Xiao, Z. Dou, M. Cao, Y.-F. Zhao, N. Samarth, C.-Z. Chang, M. R. Connolly, and C. G. Smith, 2020, Phys. Rev. Lett. **125**, 126801.

Wang, W., Y. Ou, C. Liu, Y. Wang, K. He, Q.-K. Xue, and W. Wu, 2018, Nat. Phys. **14**, 791.

Wang, Z., Z. Liu, and F. Liu, 2013, Phys. Rev. Lett. **110**, 196801.

Watanabe, R., R. Yoshimi, M. Kawamura, M. Mogi, A. Tsukazaki, X. Yu, K. Nakajima, K. S. Takahashi, M. Kawasaki, and Y. Tokura, 2019, Appl. Phys. Lett. **115**, 102403.

Wei, H., D. Tsui, M. Paalanen, and A. Pruisken, 1988, Phys. Rev. Lett. **61**, 1294.

Wei, H., D. Tsui, and A. Pruisken, 1986, Phys. Rev. B **33**, 1488.

Weng, H., R. Yu, X. Hu, X. Dai, and Z. Fang, 2015, Adv. Phys. **64**, 227.

Wieder, B. J., and B. A. Bernevig, 2018, arXiv:1810.02373.

Wilczek, F., 1987, Phys. Rev. Lett. **58**, 1799.

Wimmer, S., *et al.*, 2021, Adv. Mater. **33**, 2102935.

Wu, F., T. Lovorn, E. Tutuc, and A. H. MacDonald, 2018, Phys. Rev. Lett. **121**, 026402.

Wu, F., T. Lovorn, E. Tutuc, I. Martin, and A. MacDonald, 2019, Phys. Rev. Lett. **122**, 086402.

Wu, F., and S. D. Sarma, 2020, Phys. Rev. Lett. **124**, 046403.

Wu, J., J. Liu, and X.-J. Liu, 2014, Phys. Rev. Lett. **113**, 136403.

Wu, J., *et al.*, 2019, Sci. Adv. **5**, eaax9989.

Wu, L., M. Salehi, N. Koirala, J. Moon, S. Oh, and N. Armitage, 2016, Science **354**, 1124.

Wu, M., 2017, 2D Mater. **4**, 021014.

Wu, S., Z. Zhang, K. Watanabe, T. Taniguchi, and E. Y. Andrei, 2021, Nat. Mater. **20**, 488.

Wu, S.-C., G. Shan, and B. Yan, 2014, Phys. Rev. Lett. **113**, 256401.

Wu, X., D. Xiao, C.-Z. Chen, J. Sun, L. Zhang, M. H. Chan, N. Samarth, X. Xie, X. Lin, and C.-Z. Chang, 2020, Nat. Commun. **11**, 1.

Wu, X., *et al.*, 2020, Phys. Rev. X **10**, 031013.

Xia, Y., *et al.*, 2009, Nat. Phys. **5**, 398.

Xiao, D., M.-C. Chang, and Q. Niu, 2010, Rev. Mod. Phys. **82**, 1959.

Xiao, D., G.-B. Liu, W. Feng, X. Xu, and W. Yao, 2012, Phys. Rev. Lett. **108**, 196802.

Xiao, D., J. Shi, and Q. Niu, 2005, Phys. Rev. Lett. **95**, 137204.

Xiao, D., W. Yao, and Q. Niu, 2007, Phys. Rev. Lett. **99**, 236809.

Xiao, D., W. Zhu, Y. Ran, N. Nagaosa, and S. Okamoto, 2011, Nat. Commun. **2**, 596.

Xiao, D., *et al.*, 2018, Phys. Rev. Lett. **120**, 056801.

Xie, M., and A. H. MacDonald, 2020, Phys. Rev. Lett. **124**, 097601.

Xie, Y., *et al.*, 2021, Nature (London) **600**, 439.

Xie, Y.-M., X.-J. Gao, T.-K. Ng, and K. Law, 2020, arXiv:2012.15523.

Xie, Y.-M., C.-P. Zhang, J.-X. Hu, K. F. Mak, and K. Law, 2022, Phys. Rev. Lett. **128**, 026402.

Xie, Y.-M., C.-P. Zhang, and K. Law, 2022, arXiv:2206.11666.

Xiong, G., S.-D. Wang, Q. Niu, D.-C. Tian, and X. Wang, 2001, Phys. Rev. Lett. **87**, 216802.

Xu, G., H. Weng, Z. Wang, X. Dai, and Z. Fang, 2011, Phys. Rev. Lett. **107**, 186806.

Xu, L., *et al.*, 2020, Sci. Bull. **65**, 2086.

Xu, Y., S. Liu, D. A. Rhodes, K. Watanabe, T. Taniguchi, J. Hone, V. Elser, K. F. Mak, and J. Shan, 2020, Nature (London) **587** 7833, 214.

Xu, Y., Z. Song, Z. Wang, H. Weng, and X. Dai, 2019, Phys. Rev. Lett. **122**, 256402.

Xu, Y., B. Yan, H.-J. Zhang, J. Wang, G. Xu, P. Tang, W. Duan, and S.-C. Zhang, 2013, Phys. Rev. Lett. **111**, 136804.

Xue, F., and A. H. MacDonald, 2018, Phys. Rev. Lett. **120**, 186802.

Yan, C., S. Fernandez-Mulligan, R. Mei, S. H. Lee, N. Protic, R. Fukumori, B. Yan, C. Liu, Z. Mao, and S. Yang, 2021, Phys. Rev. B **104**, L041102.

Yan, C., Y. Zhu, S. Fernandez-Mulligan, E. Green, R. Mei, B. Yan, C. Liu, Z. Mao, and S. Yang, 2021, arXiv:2107.08137.

Yan, D., M. Yang, P. Song, Y. Song, C. Wang, C. Yi, and Y. Shi, 2021, Phys. Rev. B **103**, 224412.

Yan, J.-Q., Y. Liu, D. S. Parker, Y. Wu, A. Aczel, M. Matsuda, M. A. McGuire, and B. C. Sales, 2020, Phys. Rev. Mater. **4**, 054202.

Yan, J.-Q., S. Okamoto, M. A. McGuire, A. F. May, R. J. McQueeney, and B. C. Sales, 2019, Phys. Rev. B **100**, 104409.
Yan, J.-Q., Q. Zhang, T. Heitmann, Z. Huang, K. Chen, J.-G. Cheng, W. Wu, D. Vaknin, B. C. Sales, and R. J. McQueeney, 2019, Phys. Rev. Mater. **3**, 064202.
Yang, S., *et al.*, 2021, Phys. Rev. X **11**, 011003.
Yankowitz, M., S. Chen, H. Polshyn, Y. Zhang, K. Watanabe, T. Taniguchi, D. Graf, A. F. Young, and C. R. Dean, 2019, Science **363**, 1059.
Yankowitz, M., J. Xue, D. Cormode, J. D. Sanchez-Yamagishi, K. Watanabe, T. Taniguchi, P. Jarillo-Herrero, P. Jacquod, and B. J. LeRoy, 2012, Nat. Phys. **8**, 382.
Yasuda, K., M. Mogi, R. Yoshimi, A. Tsukazaki, K. Takahashi, M. Kawasaki, F. Kagawa, and Y. Tokura, 2017, Science **358**, 1311.
Ying, Z., S. Zhang, B. Chen, B. Jia, F. Fei, M. Zhang, H. Zhang, X. Wang, and F. Song, 2022, Phys. Rev. B **105**, 085412.
Yosida, K., 1957, Phys. Rev. **106**, 893.
You, J.-Y., C. Chen, Z. Zhang, X.-L. Sheng, S. A. Yang, and G. Su, 2019, Phys. Rev. B **100**, 064408.
Yu, R., W. Zhang, H.-J. Zhang, S.-C. Zhang, X. Dai, and Z. Fang, 2010, Science **329**, 61.
Yuan, W., *et al.*, 2022, arXiv:2205.01581.
Yuan, Y., *et al.*, 2020, Nano Lett. **20**, 3271.
Yue, C., Y. Xu, Z. Song, H. Weng, Y.-M. Lu, C. Fang, and X. Dai, 2019, Nat. Phys. **15**, 577.
Zener, C., 1951, Phys. Rev. **82**, 403.
Zener, C., and R. Heikes, 1953, Rev. Mod. Phys. **25**, 191.
Zeng, Y., C. Lei, G. Chaudhary, and A. H. MacDonald, 2018, Phys. Rev. B **97**, 081102.
Zeng, Y., F. Xue, and A. H. MacDonald, 2022, Phys. Rev. B **105**, 125102.
Zhang, D., M. Shi, T. Zhu, D. Xing, H. Zhang, and J. Wang, 2019, Phys. Rev. Lett. **122**, 206401.
Zhang, F., J. Jung, G. A. Fiete, Q. Niu, and A. H. MacDonald, 2011, Phys. Rev. Lett. **106**, 156801.
Zhang, H., C. Lazo, S. Blügel, S. Heinze, and Y. Mokrousov, 2012, Phys. Rev. Lett. **108**, 056802.
Zhang, H., C.-X. Liu, X.-L. Qi, X. Dai, Z. Fang, and S.-C. Zhang, 2009, Nat. Phys. **5**, 438.
Zhang, H., Y. Ning, W. Yang, J. Zhang, R. Zhang, and X. Xu, 2019, Phys. Chem. Chem. Phys. **21**, 17087.
Zhang, H., W. Qin, M. Chen, P. Cui, Z. Zhang, and X. Xu, 2019, Phys. Rev. B **99**, 165410.
Zhang, H., Y. Xu, J. Wang, K. Chang, and S.-C. Zhang, 2014, Phys. Rev. Lett. **112**, 216803.
Zhang, H., J. Zhang, B. Zhao, T. Zhou, and Z. Yang, 2016, Appl. Phys. Lett. **108**, 082104.
Zhang, H., T. Zhou, J. Zhang, B. Zhao, Y. Yao, and Z. Yang, 2016, Phys. Rev. B **94**, 235409.
Zhang, J., B. Zhao, and Z. Yang, 2013, Phys. Rev. B **88**, 165422.
Zhang, J., B. Zhao, Y. Yao, and Z. Yang, 2015, Phys. Rev. B **92**, 165418.
Zhang, J., *et al.*, 2013, Science **339**, 1582.
Zhang, K.-C., Y.-F. Li, Y. Liu, and Y. Zhu, 2019, J. Phys. Condens. Matter **31**, 045802.
Zhang, R.-X., H.-C. Hsu, and C.-X. Liu, 2016, Phys. Rev. B **93**, 235315.
Zhang, R.-X., F. Wu, and S. D. Sarma, 2020, Phys. Rev. Lett. **124**, 136407.
Zhang, S., *et al.*, 2020, Nano Lett. **20**, 709.
Zhang, W., D. West, S. H. Lee, Y. Qiu, C.-Z. Chang, J. S. Moodera, Y. San Hor, S. Zhang, and W. Wu, 2018, Phys. Rev. B **98**, 115165.
Zhang, X., and S.-C. Zhang, 2012, in *Micro- and Nanotechnology Sensors, Systems, and Applications IV*, Vol. 8373, edited by T. George and M. S. Islam (International Society for Optics and Photonics, Bellingham, WA), p. 837309.
Zhang, X.-L., L.-F. Liu, and W.-M. Liu, 2013, Sci. Rep. **3**, 2908.
Zhang, Y., T. Devakul, and L. Fu, 2021, Proc. Natl. Acad. Sci. U.S.A. **118**, e2112673118.
Zhang, Y., *et al.*, 2010, Nat. Phys. **6**, 584.
Zhang, Y.-H., D. Mao, Y. Cao, P. Jarillo-Herrero, and T. Senthil, 2019, Phys. Rev. B **99**, 075127.
Zhao, Y., and Q. Liu, 2021, Appl. Phys. Lett. **119**, 060502.
Zhao, Y.-F., R. Zhang, L.-J. Zhou, R. Mei, Z.-J. Yan, M. H. Chan, C.-X. Liu, and C.-Z. Chang, 2022, Phys. Rev. Lett. **128**, 216801.
Zhao, Y.-F., *et al.*, 2020, Nature (London) **588**, 419.
Zhao, Y.-F., *et al.*, 2021, Nano Lett. **21**, 7691.
Zhou, J., Q. Sun, and P. Jena, 2017, Phys. Rev. Lett. **119**, 046403.
Zhou, Z., Y.-J. Chien, and C. Uher, 2005, Appl. Phys. Lett. **87**, 112503.
Zhou, Z., Y.-J. Chien, and C. Uher, 2006, Phys. Rev. B **74**, 224418.
Zhu, J., J.-J. Su, and A. H. MacDonald, 2020, Phys. Rev. Lett. **125**, 227702.
Zhu, K., *et al.*, 2020, J. Phys. Condens. Matter **32**, 475002.
Zhu, Q., M. W.-Y. Tu, Q. Tong, and W. Yao, 2019, Sci. Adv. **5**, eaau6120.
Zhu, T., *et al.*, 2021, Nano Lett. **21**, 5083.
Zou, R., F. Zhan, B. Zheng, X. Wu, J. Fan, and R. Wang, 2020, Phys. Rev. B **101**, 161108.